4. SITE 1040[1]

Shipboard Scientific Party[2]

HOLE 1040A

Position: 9°39.707′N, 86°10.746′W

Start hole: 0345 hr, 5 November 1996

End hole: 1545 hr, 5 November 1996

Time on hole: 12.0 hr (0.5 days)

Seafloor (drill-pipe measurement from rig floor, mbrf): 4188.0

Water depth (drill-pipe measurement from sea level, m): 4177.0

Distance between rig floor and sea level (m): 11.0

Total depth (drill-pipe measurement from rig floor, mbrf): 4197.5

Penetration (mbsf): 9.5

Coring totals:

Type: APC; No: 1; Cored: 9.5 m; Recovered: 9.58 m (100.8%)

Formation:

Subunit P1A (0–9.58 mbsf): Olive green silty clay to clayey silt with debris flows and silty sands (Pliocene–?Pleistocene)

HOLE 1040B

Position: 9°39.707′N, 86°10.746′W

Start hole: 1545 hr, 5 November 1996

End hole: 1400 hr, 8 November 1996

Time on hole: 70.25 hr (2.93 days)

Seafloor (drill-pipe measurement from rig floor, mbrf): 4189.0

Water depth (drill-pipe measurement from sea level, m): 4178.0

Distance between rig floor and sea level (m): 11.0

Total depth (drill-pipe measurement from rig floor, mbrf): 4379.2

Penetration (mbsf): 190.2

Coring totals:

Type: APC; No: 2; Cored: 14.0 m; Recovered: 14.06 m (100.4%)
Type: XCB; No: 20; Cored: 176.2 m; Recovered: 113.90 m (64.6%)
Total: No: 22; Cored: 190.2 m; Recovered: 127.92 m (67.3%)

Formation:

Subunit P1A (0–74.80 mbsf): Olive green silty clay with debris flows and silty sands (Pliocene–?Pleistocene)
Subunit P1B (74.80–190.2 mbsf): Olive green silty clay to clayey silt with intervals of silt to very fine sand (Pliocene–?Pleistocene)

HOLE 1040C

Position: 9°39.697′N, 86°10.735′W

Start hole: 0115 hr, 11 November 1996

End hole: 1200 hr, 18 November 1996

Time on hole: 178.75 hr (7.45 days)

Seafloor (drill-pipe measurement from rig floor, mbrf): 4189.0

Water depth (drill-pipe measurement from sea level, m): 4177.9

Distance between rig floor and sea level (m): 11.1

Total depth (drill-pipe measurement from rig floor, mbrf): 4854.0

Penetration (mbsf): 665.0

Drilled: 0–159.3 mbsf

Coring totals:

Type: RCB; No: 53; Cored: 505.7 m; Recovered: 377.28 m (74.6%)

Formation:

Subunit P1B (159.3–371.2 mbsf): Olive green silty claystone with intervals of siltstone to very fine sandstone (Pliocene–?Pleistocene)
Subunit U1A (371.2–384.4 mbsf): Dark olive green clayey diatomite with silty sand interbeds (<0.20 Ma)
Subunit U1B (384.4–422.6 mbsf): Clayey diatomite with ash layers (middle–late Pleistocene)
Subunit U2A (422.6–472.47 mbsf): Dark olive green silty claystone with ash layers (early Pliocene–middle Pleistocene)
Subunit U2B (472.47–479.7 mbsf): Dark to light olive green silty claystone with calcareous claystone and ash layers (late Miocene–early Pliocene)
Subunit U3A (479.7–497.8 mbsf): Ivory gray siliceous nannofossil chalk and claystone (late Miocene)
Subunit U3B (497.8–573.35 mbsf): Ivory to light green siliceous nannofossil chalk with minor ash layers (middle–late Miocene)
Subunit U3C (573.35–653.53 mbsf): Nannofossil chalk, diatomite, and breccia interbeds (middle Miocene)
Unit U4 (653.53–661.47 mbsf): Glassy pyroxene gabbro intrusion with plagioclase glomerocrysts (post-15.6 Ma)

HOLE 1040D

Position: 9°39.719′N, 86°10.758′W

Start hole: 0915 hr, 20 November 1996

End hole: 0315 hr, 23 November 1996

Time on hole: 66.0 hr (2.75 days)

Seafloor (drill-pipe measurement from rig floor, mbrf): 4189.0

Water depth (drill-pipe measurement from sea level, m): 4177.9

Distance between rig floor and sea level (m): 11.1

Total depth (drill-pipe measurement from rig floor, mbrf): 4526.5

Penetration (mbsf): 337.5

Logging while drilling

[1]Kimura, G., Silver, E.A., Blum, P., et al., 1997. *Proc. ODP, Init. Repts.*, 170: College Station, TX (Ocean Drilling Program).
[2]Shipboard Scientific Party is given in the list preceding the Table of Contents.

Previous Chapter Table of Contents Next Chapter

HOLE 1040E

Position: 9°39.731′N, 86°10.755′W

Start hole: 0315 hr, 23 November 1996

End hole: 2015 hr, 24 November 1996

Time on hole: 41.0 hr (1.71 days)

Seafloor (drill-pipe measurement from rig floor, mbrf): 4189.0

Water depth (drill-pipe measurement from sea level, m): 4177.9

Distance between rig floor and sea level (m): 11.1

Total depth (drill-pipe measurement from rig floor, mbrf): 4507.4

Penetration (mbsf): 318.4

Logging while drilling

Principal results: The lithostratigraphic and biostratigraphic objectives included determining the nature and age of the sedimentary wedge, the relationship of underthrust units to those of the reference section at Site 1039, and the implications for the balance of mass and fluids between the trench sequence and the underthrust and wedge sequences. Another important objective was to determine the structural fabric of both the sedimentary wedge and the underthrust section. We were mostly successful in achieving these objectives, drilling through the décollement and the entire underthrust sedimentary sequence and into gabbro intrusions very similar to those in Site 1039. Because logging-while-drilling (LWD) operations were only partially successful at this site, we did not obtain a full in situ physical properties data set for correlations with Site 1039.

The sedimentary wedge overlies the same three sedimentary units and one igneous unit as were drilled at Site 1039 (Fig. 1). The wedge unit (P1) consists of a subunit (P1A; 0–74.8 mbsf) of olive green silty clay (stone) with debris flows and silty sands (stones) overlying a lower subunit (P1B; 74.8–371.2 mbsf) of olive green silty claystone with intervals of siltstone to very fine sandstone. The age of the wedge unit is Pliocene–?Pleistocene. Below Unit P1, Subunit U1A (<0.20 Ma; 371.2–384.4 mbsf) is a clayey diatomite with silty sand interbeds, and Subunit U1B (middle–late Pleistocene; 384.4–422.6 mbsf) is clayey diatomite with ash layers. Subunit U2A (late Pliocene–middle Pleistocene; 422.6–472.47 mbsf) is silty claystone with ash layers, and Subunit U2B (late Miocene–early Pliocene; 472.47–479.7) is silty claystone with calcareous claystone and ash layers. Subunit U3A (late Miocene; 479.7–497.8 mbsf) is a siliceous nannofossil chalk and claystone, whereas Subunit U3B (middle–late Miocene; 497.8–573.35) is siliceous nannofossil chalk. Subunit U3C (middle Miocene; 573.35–653.53) is nannofossil, chalk, diatomite, and breccia interbeds. Finally, Unit U4 (post-15.6 Ma; 653.53–661.47 mbsf) is a pyroxene gabbro intrusion.

Deformational structures were observed in the first core at Site 1040. Fissility to incipient scaly fabric was observed from the top of the prism discontinuously throughout Unit P1 (0–371 mbsf). Deformation bands and distributed fractures are common in the upper 20 mbsf and discontinuous throughout Unit P1. Many of these may be drilling induced, particularly stratal disruptions. Both brittle and plastic deformation structures are common from the surface to 370 mbsf. Plastic deformation is associated with soft, sticky clay and severe spiral drilling disturbance. Therefore, original plastic deformation cannot be identified, although it may have existed within these clay-rich intervals. From 340 to 350 mbsf, we find that fracture networks, stratal disruption, veins, and incipient scaly clay structures are common. Locally, a very intense fracture fabric is formed. From 350 to 360 mbsf, brittle deformation gives way to plastic deformation in sticky clays. Throughout Unit P1, cores are highly disrupted by drilling, with evidence of both flow-in and intensive torque transfer to the cores. Paleomagnetic studies indicate that the more plastic intervals have corkscrewed tens of times.

Below 371 mbsf, the intense fissility, fracture networks, and stratal disruption disappear, and evidence for torque transfer to the cores decreases markedly. Primary sedimentary structures are common, such as *Zoophycos* and other burrows. Mud-filled veins are present. Steep bedding dips are measured in the interval 420–484 mbsf. At 460 mbsf, microfaulting is more abundant in the cores, and fluid escape breccias are noted. Minor faults occur through the cores to the base of the section. Microfaults are mostly reverse in the interval 430–500 mbsf and show mostly normal displacement in the interval 610–650 mbsf. Incipient stylolitization is present in the lowest 10 m of the sediment section, developed largely subhorizontally, and rare boudinage is present. The lower 150 m of the section shows consistent bedding dips of up to 20°. This attitude can be explained by the measured hole deviation of up to 18° (see “Operations” section, this chapter).

The distribution of age vs. depth in Site 1040 for Units U1, U2, and U3 is similar to that of Site 1039. The major difference between the two sites is the difference in thickness of the corresponding units. Units U1 and U2 in Site 1040 are ~67% of the thickness of those in Site 1039, whereas Unit U3 in Site 1040 is about 80% of that in Site 1039. These differences correspond well with measured differences in porosity and bulk density between the two sites. Although some of the same fossil zones are found in both sites, a number are different, probably due in part to the 10-m spacing of core-catcher samples for shipboard analysis. Post-cruise work should shed more light on these differences. Within the sedimentary wedge (0–330 mbsf), numerous normal and reversed polarity intervals have been determined. Lack of good biostratigraphic control and the high probability of thrust faults within this interval have prevented a unique assignment of our reversal stratigraphy to any specific portion of the magnetic polarity time scale. The reversed-polarity results at 5 mbsf in Hole 1040B do suggest, however, that these near-surface sediments are at least 0.78 Ma in age. Beneath the décollement (371–655 mbsf), a good magnetostratigraphic record has been obtained from the underthrust sediments. In particular, the Jamaica Event (0.2 Ma) has been located at 383.7 mbsf, and a complete set of reversals ranging in age from 2.14 Ma (Chron C2r.1n) to 6.935 Ma (Chron C3Bn) occurs between 458 and 482 mbsf in Hole 1040C. Preliminary age vs. depth estimates for the underthrust section at Site 1040 from biostratigraphy and magnetostratigraphy are, respectively, 41 and 72 m/m.y. for the Pleistocene, and 6 and 5.8 m/m.y. for the Pliocene to upper Miocene. The age vs. depth for the middle Miocene from biostratigraphy is 32 m/m.y. The oldest sediment dated at Site 1040 was 15.6 Ma, younger than the 16.4-Ma age found at Hole 1039C.

Some primary objectives of Site 1040 were to determine the chemistry of pore waters within the sedimentary wedge, décollement, and underthrust section; to compare Site 1040 chemistry with that of Site 1039; and to gain a fuller understanding of the nature of fluid and heat flow near the toe of the Costa Rican Margin. We were successful in meeting these fluid-chemistry objectives, obtaining accurate chemical depth profiles even from intervals with severe drilling disturbance.

Pore-water geochemistry shows significant decreases in salinity in the upper 371 m at Site 1040. Chloride concentrations decrease rapidly in the upper 40 mbsf from 550 to ~512 mM, and salinity decreases from 34.5 to ~30 in the upper 40 m. Chloride and salinity both decreased further to ~500 mM and 28, respectively, by 80–100 mbsf. In addition, both properties show large minima at 200 mbsf and a moderate one at 300 mbsf, implying both flow through fractures and presence of gas hydrates at 200 mbsf. Both properties also show minimum concentrations in the décollement zone, at 360 mbsf, and both return to normal seawater values at 371 mbsf, just beneath the décollement, and maintain these values to 653 mbsf. Calcium and magnesium also show similar effects. Magnesium decreases from 50 mM at the surface to ~20 mM at 100 mbsf, shows minima at 200 and 300 mbsf and in the décollement zone, and then increases to 41 mM at 390 mbsf. It also shows a small maximum concentration of 47 mM at 382 mbsf, just below the décollement. Calcium shows a curve that is the reverse of magnesium, with maxima at 200 and 360 mbsf, and a small maximum at 280 mbsf. The distributions of ammonium, phosphate, silica, potassium, sulfate, and alkalinity all show sharp boundaries and major changes across the décollement.

The distribution of methane gas also changes significantly at the décollement. Methane increases from a few parts per million by volume (ppmv) in the upper few meters to 8996 ppmv at 28.5 mbsf. In the interval

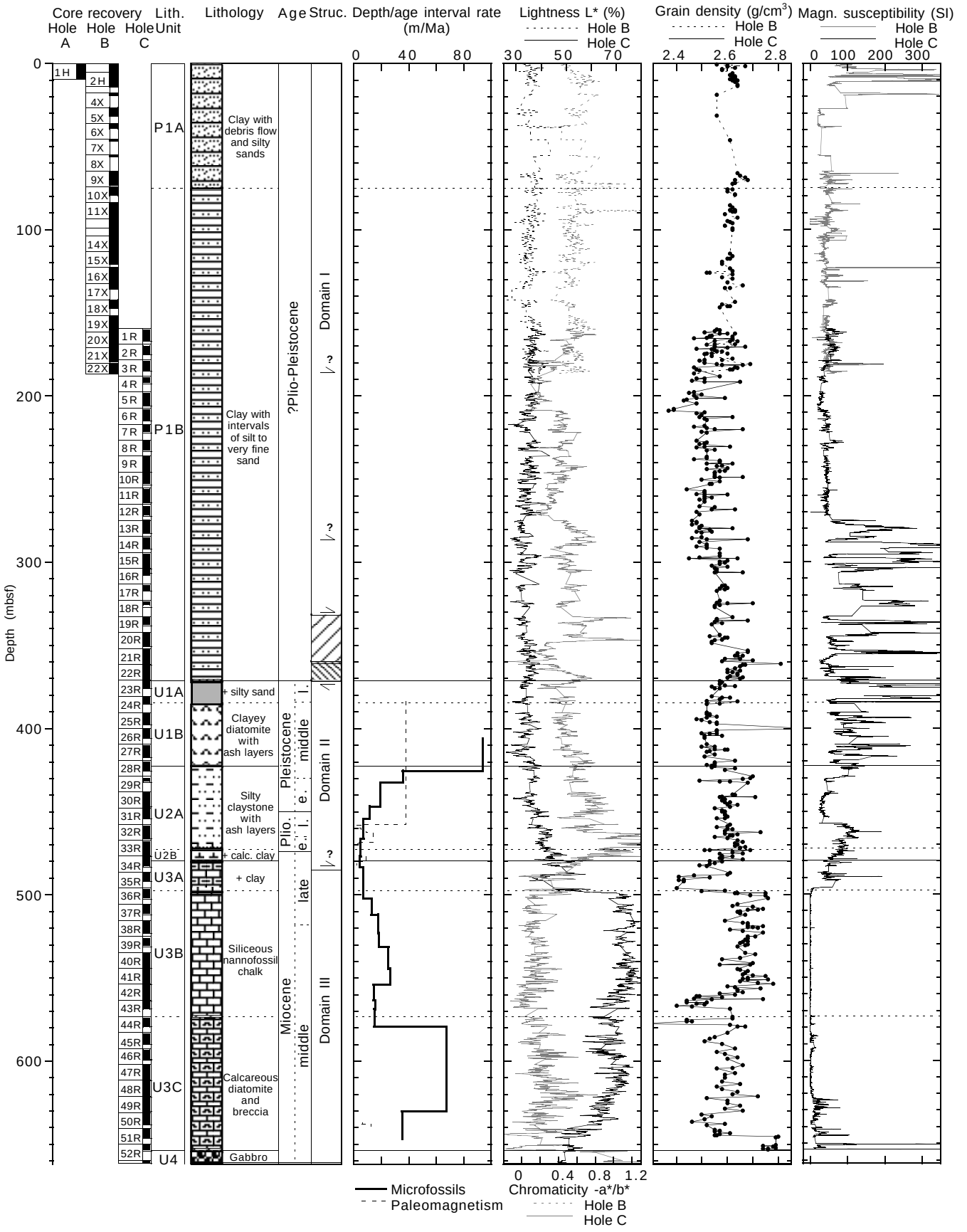

Figure 1. Graphical representation and summary plots of shipboard core and downhole measurements. Explanation of data types and their acquistion are found in the "Explanatory Notes" chapter (this volume). Shipboard descriptions of data are found in relevant sections in this chapter. LWD = logging while drilling, and SGR = spectral gamma ray (total counts).

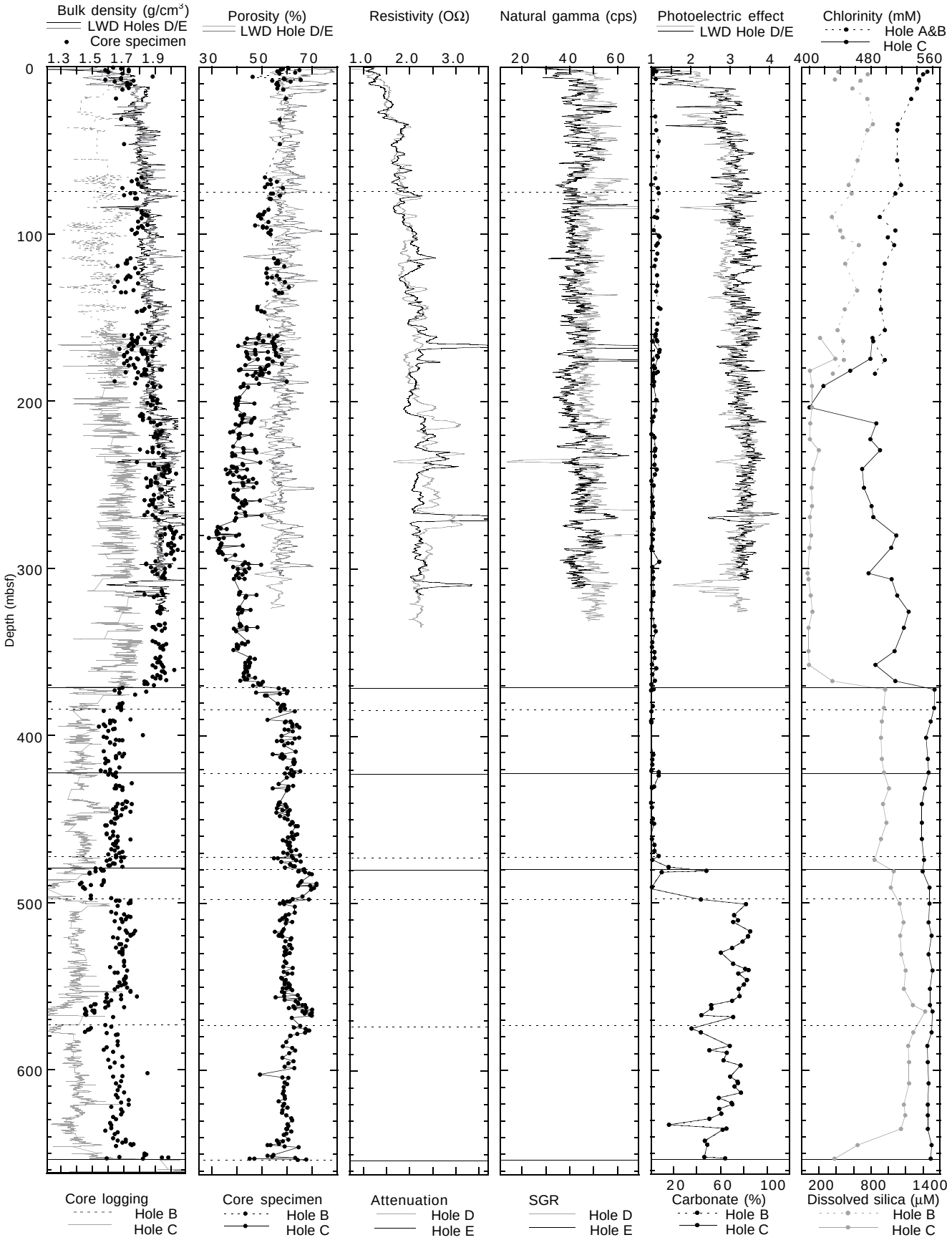

Figure 1 (continued).

from 28.5 to 374 mbsf, concentrations increase to values between 4818 and 116,561 ppmv. Below the base of the décollement, methane values decrease sharply, and from 460 to 653 mbsf the values are again a few parts per million by volume. Propane is very low at Site 1040, but shows a peak of 24 ppmv between 191 and 203.6 mbsf and a peak of 19 ppmv between 348.2 and 357.8 mbsf. These two intervals coincide with anomalies in fluid composition of the pore waters, suggesting a significant input in allochthonous thermogenic gas. Below 374 mbsf, only small amounts of propane were detected throughout the underthrust section. The distribution of calcium carbonate in the underthrust section shows the same distinct patterns as reported for Site 1039.

The XRF sediment geochemistry may be used for several purposes. A sharp increase in Ba, Cu, and Ni depth profiles is observed between samples taken at 367 and 372 mbsf and identifies the underthrust section. The sediments of the deformed wedge are homogeneous in composition with the exception of a single ash layer at 180 mbsf, which serves as a fluid conduct. The chemical composition of all the wedge sediments indicates significant contributions from the volcanic arc. The subducted Ba flux beneath Costa Rica is comparable to, or slightly larger than, that at Guatemala.

Primary objectives of studying the physical properties of the wedge and underthrust section included determination of the changes from reference state to either accreted or underthrust material, using density, porosity, magnetic susceptibility, temperature and thermal conductivity, and seismic velocity. We successfully determined the differences in these parameters compared to those of the reference site. Physical properties at Site 1040 show significant changes compared to equivalent units at Site 1039. Seismic velocity measurements at Site 1040 average ~1700 m/s from 371 to 496 mbsf. From 496 to ~560 mbsf, seismic velocity averages 1660 m/s and increases steadily from 1660 m/s at 560 mbsf to 1760 m/s at 653 mbsf. Porosity varies from 50% at 150 mbsf to 40% at 371 mbsf. At this depth (the décollement), porosity increases rapidly to ~60% and stays at this value to a depth of 650 mbsf. Bulk density at Site 1040 increases from ~1660 kg/m^3 at 150 mbsf to 1720 kg/m^3 at 371 mbsf. Density drops to 1430 kg/m^3 between the décollement at 372 mbsf and a depth of 430 mbsf. Thermal conductivity shows considerable scatter, but measurements indicate an average value of 0.9 W/(m·K) from 0 to 490 mbsf. Magnetic susceptibility is a primary property for cross-hole correlation, because its natural variations are not significantly affected by core disturbance. It shows some peaks in the upper 20 m, then stays very low to 270 mbsf. From 270 to 496 mbsf, magnetic susceptibility is relatively high and varied, and from 496 to 650 mbsf it is essentially zero, increasing only slightly in the lower 30 m and showing a single peak at 653 mbsf because of the presence of the gabbro intrusion.

Temperature measurements downhole show an extremely low gradient of 8.3°C/km from the surface to 200 mbsf, followed by 5.3°C/km from 200 to 350 mbsf, and then returning to 8.4°C/km from 350 to 475 mbsf. The corresponding heat flows calculated for these intervals are 7.5, 4.8, and 8.9 mW/m^2.

In situ density, porosity, resistivity, and gamma-ray measurements were collected with the compensated density neutron (CDN) and compensated dual resistivity (CDR) tools as part of the LWD downhole measurement program. Two logging runs were made using different drill bits in an unsuccessful attempt to penetrate through the décollement. The total logged intervals at Holes 1040D and 1040E are from the seafloor to 325 and 307 mbsf, respectively.

Downhole density and porosity measurements correlate roughly with the core specimen measurements, and resistivity generally follows the pattern of density. Although the profiles from Holes 1040D and 1040E show similar trends in density and porosity, they show different log responses in several intervals. Bulk-density profiles gradually increase with depth, but show a number of segments with rapid downward decreases between more gradual downward increases. Most of the density values range between 1.7 and 2.0 g/cm^3. Significant decreases in density occur at 84 mbsf (1.55 g/cm^3), 237 mbsf (1.68 g/cm^3), and 310 mbsf (1.60 g/cm^3) in Hole 1040D, and 168 mbsf (1.70 g/cm^3) and 269 mbsf (1.72 g/cm^3) in Hole 1040E. Porosities calculated directly from the neutron log fluctuate widely throughout the logged interval. The filtered neutron porosity profile indicates porosities from 65% to 50%, decreasing gradually with depth. The porosity profiles show a reverse trend to that of the density profile, but several low-density intervals indicate low neutron porosities.

In the interval 0–200 mbsf, the resistivity values gradually increase from 1 to 2.5 Ωm in Hole 1040D, whereas in Hole 1040E the values show greater fluctuation. In Hole 1040D, the interval 200–277 mbsf is characterized by relatively high resistivity values up to 3.2 Ωm. In Hole 1040E, high resistivity is identified between 210 and 242 mbsf. A resistivity maximum at 114 mbsf corresponds to a density maximum. However, resistivity maxima at 168, 238, and 270 mbsf are correlated to minima in density.

In summary, we were highly successful in meeting our primary objectives in lithostratigraphy, biostratigraphy, geochemistry, and physical properties. We had only partial success at this site in carrying out LWD because of the inability of the tool to penetrate beneath a presumably overpressured zone.

BACKGROUND AND SCIENTIFIC OBJECTIVES

Site 1040 was located 1.6 km upslope from the toe of the slope off the Nicoya Peninsula, Costa Rica (Fig. 2, "Site 1039" chapter, this volume). The objective of this site was to pass through the sedimentary wedge near the toe, the décollement, and the underthrust sedimentary section beneath the décollement. Specific objectives included the nature and age of the wedge material; the physical properties of the wedge and underthrust section; the chemistry of pore waters within the wedge, décollement, and underthrust sections; and the implications for the balance of mass and fluids between the trench sequence and the underthrust and wedge sequence. The specific location of Site 1040 was chosen because the wedge appeared to be entirely sedimentary in the seismic records, the underthrust section was traceable from the reference section, although significantly thinner, and the basement was accessible to the drill. In addition, the décollement reflection is clearly phase-reversed relative to the seafloor reflection, indicating an inversion of seismic impedance and possibly elevated pore-fluid pressure. Furthermore, very low heat flow was measured from surface studies in this area, and we hoped to learn the cause of this anomaly as well as obtaining additional downhole thermal data.

The seismic stratigraphy indicates the same seismic-stratigraphic units in the underthrust section as visible beneath Site 1039, an upper weakly reflecting unit and a lower more strongly reflecting unit with greater reflector continuity (Fig. 2). Above the décollement, there is very little internal coherence of reflectors, and those reflectors that can be resolved have low continuity. The top of Site 1040 appears to be cut by a zone of discontinuous reflectors dipping upslope. The latter may represent a fault zone that intersects the site between 50 and 75 mbsf. Site 1040 is located on a narrow terrace, which could indicate the upper surface of a slide or a low gradient part of the slope above a structural uplift. Several other probable faults can be discerned faintly in this upper material, but no throughgoing reflection can be resolved.

The décollement is very sharply defined in this region by a negatively polarized reflection (Shipley and Moore, 1986), which was interpreted by Shipley et al. (1990) to indicate that the velocity in the wedge is significantly higher than that of the underthrust sediment. The décollement reflector can be traced without a break from beneath Site 1040 to the surface at the toe of the wedge (Fig. 2).

In the underthrust section, the major reflections in the lower unit can be traced reasonably well between Sites 1039 and 1040. Because of compaction thinning, some stratigraphic layering that is seismically apparent at Site 1039 falls below the level of seismic resolution by Site 1040 (Fig. 2). About 1 km west of Site 1040, a normal fault displaces the lower unit about 30 m, down to the northeast. The fault also displaces the basement reflector, and a possible sill northeast of the fault is terminated at the fault.

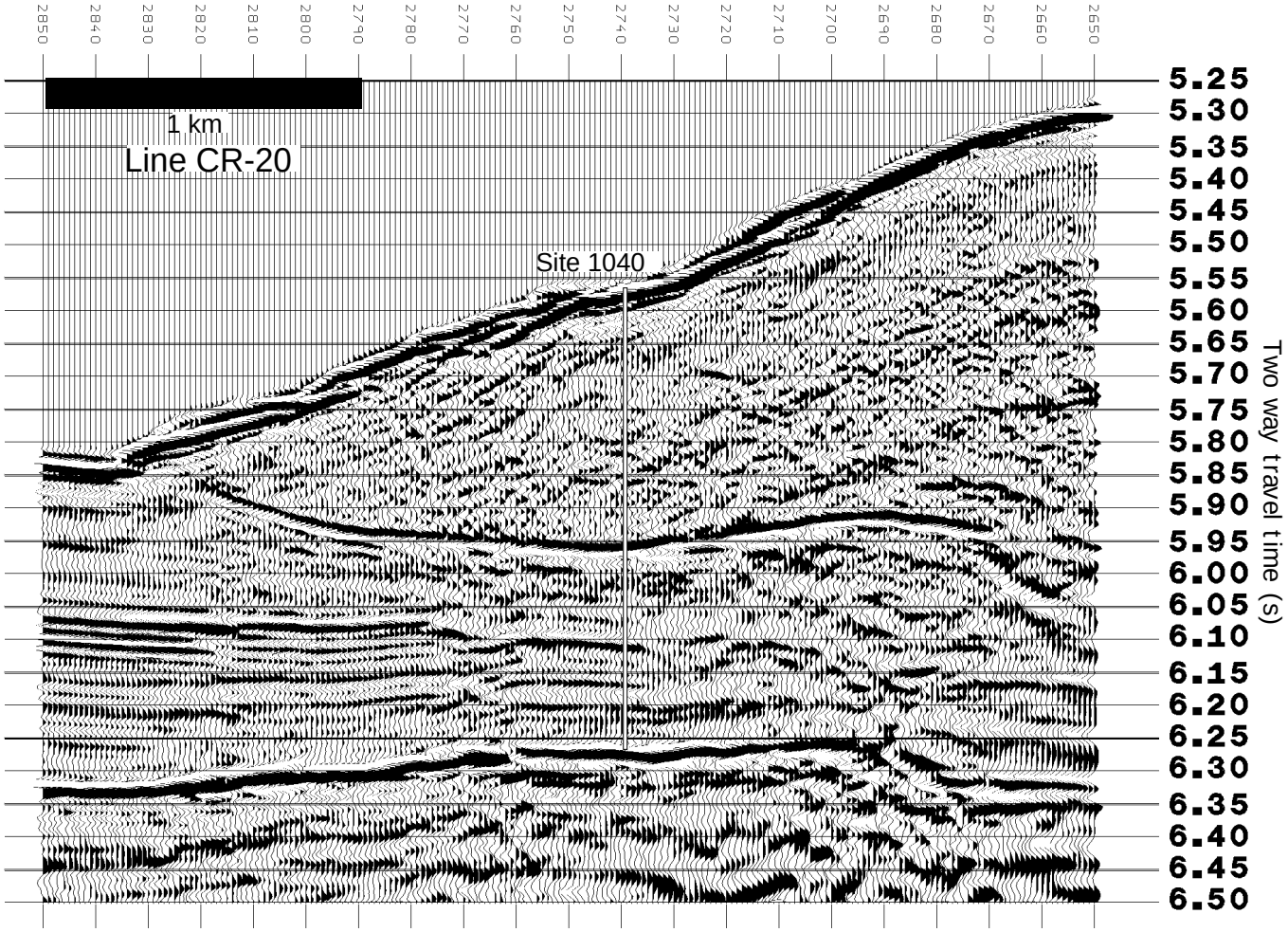

Figure 2. Detail of time-migrated seismic-reflection Line CR-20 across the toe of the subduction complex, showing the location of Site 1040.

The décollement phase inversion terminates about 1 km northeast of Site 1040, and that termination appears to coincide with the location of a thrust fault that cuts upsection, crossing Site 1040 at about 100 ms below the seafloor. The décollement is convex upward between the site location and the thrust fault. Reflectors are disturbed below this convexity, and the total thickness of the section is measurably greater than that to the southwest, suggesting convergent deformation resulting in tectonic thickening of the section. Shipley et al. (1992) identified this incipient deformation as the early stage of a sediment underplating process.

In a previous heat-flow survey (Langseth and Silver, 1996), attempted heat-flow measurements at the location of Site 1040 failed because the probe would not penetrate the near-surface sediments. Attempts to obtain piston cores were unsuccessful for the same reason. Heat-flow measurements taken very close to the trench axis averaged 23 mW/m^2. Upslope from Site 1040, heat-flow values averaged 28–30 mW/m^2.

LWD was as high a priority for Site 1040 as it was for Site 1039. Comparison of LWD at Sites 1040 and 1039 could provide us with unprecedented detail in the record of density and porosity between a reference site and an underthrust sedimentary section.

OPERATIONS

Hole 1040A

After completion of Holes 1039A and 1039B, the ship was moved to Site 1040 in dynamic positioning (DP) mode. The precision depth recorder (PDR) reading of 4136.4 m water depth (corrected to the rig floor) was in error because of several diffracted side echoes. After three water cores, the drill string was lowered until a firm seafloor was identified ("felt") at a depth of 4191 m. The bit was positioned at a depth of 4188 m for Core 1H, which did not vent, indicating that the barrel did not fully stroke. In addition, 30 kilo-pounds (kips) was required to extract the barrel from the seabed. When recovered, the barrel contained 9.58 m of material (Tables 1, 2). Because a reliable mudline depth was not identified, it was decided that a new hole should be started.

Hole 1040B

The bit was raised to a depth of 4185 m for spudding Hole 1040B. This time the barrel did fully stroke and only required 15 kips to extract. It recovered 5.51 m of core material, establishing the mudline. Core 2H did not fully stroke, but 8.5 m was recovered, and it was decided to attempt a third advanced hydraulic piston (APC) core. However, while attempting to drill out the rathole from Core 2H, it became apparent that the hole could not be advanced without a core barrel in place. The APC barrel was recovered, and an extended core barrel (XCB) core barrel was dropped at that point.

Coring with the XCB continued at a slow pace, because the drill collars making up the bottom-hole assembly (BHA) were well above the seabed. Low bit weight and top drive rpm were used initially, and each was increased as penetration advanced into the firm seabed. Even with the drill collars buried below the seabed, the rate of penetration (ROP) was slow. Bit balling was suspected as the primary rea-

Table 1. Coring summary for Site 1040.

Core	Date (Nov. 1996)	Time (UTC)	Depth (mbsf)	Length cored (m)	Length recovered (m)	Recovery (%)
170-1040A-						
1H	05	2130	0.0-9.5	9.5	9.58	101.0
Coring totals:				9.5	9.58	101.0
170-1040B-						
1H	05	2240	0.0-5.5	5.5	5.51	100.0
2H	05	2355	5.5-14.0	8.5	8.55	100.0
3X	06	0250	14.0-18.0	4.0	0.28	7.0
4X	06	0510	18.0-27.0	9.0	1.47	16.3
5X	06	0845	27.0-36.4	9.4	4.92	52.3
6X	06	1030	36.4-45.8	9.4	2.64	28.1
7X	06	1420	45.8-55.2	9.4	0.72	7.7
8X	06	1705	55.2-64.8	9.6	1.22	12.7
9X	06	1955	64.8-74.4	9.6	8.26	86.0
10X	06	2355	74.4-84.0	9.6	5.26	54.8
11X	07	0300	84.0-93.6	9.6	9.88	103.0
12X	07	0620	93.6-99.1	5.5	4.91	89.3
13X	07	0835	99.1-103.8	4.7	7.83	166.0
14X	07	1055	103.8-113.4	9.6	8.56	89.1
15X	07	1430	113.4-122.9	9.5	7.48	78.7
16X	07	1705	122.9-132.5	9.6	9.65	100.0
17X	07	1935	132.5-142.2	9.7	2.94	30.3
18X	07	2230	142.2-151.8	9.6	4.99	52.0
19X	08	0045	151.8-161.4	9.6	8.94	93.1
20X	08	0420	161.4-171.0	9.6	9.74	101.0
21X	08	0715	171.0-180.6	9.6	8.29	86.3
22X	08	1015	180.6-190.3	9.7	5.98	61.6
Coring totals:				190.3	128.02	67.3
170-1040C-						
1R	12	0150	159.3-168.8	9.5	7.67	80.7
2R	12	0340	168.8-178.4	9.6	6.47	67.4
3R	12	0535	178.4-188.0	9.6	6.62	68.9
4R	12	0755	188.0-197.6	9.6	4.88	50.8
5R	12	1025	197.6-207.3	9.7	8.57	88.3
6R	12	1300	207.3-216.9	9.6	7.86	81.9
7R	12	1540	216.9-226.5	9.6	5.48	57.1
8R	12	1900	226.5-236.1	9.6	6.73	70.1
9R	12	2105	236.1-245.8	9.7	9.97	103.0
10R	12	2245	245.8-255.4	9.6	7.53	78.4
11R	13	0040	255.4-265.1	9.7	8.99	92.7
12R	13	0300	265.1-274.7	9.6	7.07	73.6
13R	13	0550	274.7-284.4	9.7	8.03	82.8
14R	13	0815	284.4-294.1	9.7	7.58	78.1
15R	13	1040	294.1-303.7	9.6	9.85	102.0
16R	13	1310	303.7-313.3	9.6	3.16	32.9
17R	13	1530	313.3-323.0	9.7	4.30	44.3
18R	13	1925	323.0-332.6	9.6	4.13	43.0
19R	13	2150	332.6-342.2	9.6	5.75	59.9
20R	14	0020	342.2-351.8	9.6	8.61	89.7
21R	14	0315	351.8-361.4	9.6	9.87	103.0
22R	14	0525	361.4-371.0	9.6	9.85	102.0
23R	14	0825	371.0-380.6	9.6	5.24	54.6
24R	14	1020	380.6-390.2	9.6	5.04	52.5
25R	14	1210	390.2-399.8	9.6	7.70	80.2
26R	14	1405	399.8-409.4	9.6	5.96	62.1
27R	14	1545	409.4-419.1	9.7	7.99	82.4
28R	14	1940	419.1-428.6	9.5	6.22	65.5
29R	14	2130	428.6-438.2	9.6	4.00	41.6
30R	14	2320	438.2-447.8	9.6	8.55	89.0
31R	15	1000	447.8-457.4	9.6	6.40	66.6
32R	15	1155	457.4-467.0	9.6	8.89	92.6
33R	15	1520	467.0-476.7	9.7	9.91	102.0
34R	15	1705	476.7-486.4	9.7	6.78	69.9
35R	15	1850	486.4-496.0	9.6	5.42	56.4
36R	15	2025	496.0-505.6	9.6	6.36	66.2
37R	15	2155	505.6-515.3	9.7	6.18	63.7
38R	15	2325	515.3-524.9	9.6	7.87	82.0
39R	16	0100	524.9-534.5	9.6	6.44	67.1
40R	16	0235	534.5-544.1	9.6	9.84	102.0
41R	16	0400	544.1-553.7	9.6	9.87	103.0
42R	16	0545	553.7-563.4	9.7	9.79	101.0
43R	16	0825	563.4-573.1	9.7	5.20	53.6
44R	16	1015	573.1-582.7	9.6	6.24	65.0
45R	16	1210	582.7-592.3	9.6	7.34	76.4
46R	16	1400	592.3-601.9	9.6	6.58	68.5
47R	16	1550	601.9-611.6	9.7	9.90	102.0
48R	16	1745	611.6-621.2	9.6	9.87	103.0
49R	16	1925	621.2-630.8	9.6	8.82	91.9
50R	16	2105	630.8-640.4	9.6	7.70	80.2
51R	16	2255	640.4-650.0	9.6	6.17	64.3
52R	17	0125	650.0-659.6	9.6	4.29	44.7
53R	17	0755	659.6-665.0	5.4	1.75	32.4
Coring totals:				505.7	377.28	74.6

Note: UTC = Universal Time Coordinated.

son, because the material being cored was not hard enough to dictate such a slow ROP. Coring continued to Core 22X at 4379.2 mbrf, when an XCB space sub failed, leaving the XCB hard formation cutting shoe in the hole. The failure terminated the coring in Hole 1040B at a total depth of 190.2 mbsf.

Headspace methane levels varied from 53,995 to 44,529 ppmv, whereas ethane levels were 7 to 209 ppmv. Propane varied from 0 to 6 ppmv. Vacutainer data indicated more than 100% methane in several cores. Core 16X was under high pressure when recovered, and core started being ejected out of the barrel at the rig floor immediately upon recovery. Standard precautions were taken on the rig floor and core receiving platform regarding safety.

A total of four Davis-Villinger Temperature Probe (DVTP) measurements were taken beginning after Core 6X and continued on ~50-m intervals during XCB coring. The first DVTP measurement was bad.

Several mud sweeps were pumped in the lower 100 mbsf after fill (1.5–12.0 m) was identified between connections. Once coring had ceased, the hole was filled with 10.5-lb/gal mud, and the drill string was tripped out of the hole. While pulling pipe, an overpull of 30 kips was taken between 177.7 and 120.1 mbsf. The drill string cleared the seafloor at 0630 hr, 8 November 1996.

Operation at Site 1039

During the pipe trip, the vessel was offset 1.2 nmi back to Site 1039 to drill the rotary core barrel (RCB) Hole 1039C (see "Operations" section, "Site 1039" chapter, this volume). After completing Hole 1039C at 0115 hr, 11 November 1996, the pipe was secured, placing the bit at 3988.1 m, for the DP transit back to Site 1040 to spud the RCB Hole 1040C.

Hole 1040C

After spacing out the drill pipe to 4148.0 mbrf, the water-sampling temperature probe (WSTP) was deployed, and a bottom-water sample was collected. The previously collected sample at this site was not good. A center bit-assembly was then pumped downhole, and the drill string was lowered to 4189.0 m. Hole 1040C was spudded and drilling continued to a depth of 4348.3 m (159.3 mbsf), where RCB coring began. An overlap of ~30 m was desired with the previously drilled XCB hole at this site. Coring with the RCB began with Core 1R and continued until a hard layer near the décollement was contacted at the bottom of Core 19R at a depth of 342.2 mbsf. The subsequent Cores 20R and part of 21R were considerably fractured and assumed to be in the décollement zone. Coring continued from that point with the penetration rate continually increasing until it stabilized around 60–70 m/hr (8–9 min rotating time). The rapid ROP was attributed to coring through the underconsolidated sediments beneath the décollement. A gabbro intrusion was contacted in Core 52R at a depth of 657.0 mbsf, and the last core recovered was Core 53R at a total depth of 665.0 mbsf.

Some drill-string drag was identified while drilling Hole 1040C. The Tensor electronic multishot tool was deployed and drift measurements were taken while retrieving Core 43R. Measurements were taken on bottom at 4750 m (573.1 mbsf) and 100 m above bottom at 4650 m (473.1 mbsf). The hole angle was 18.5° and 17.5°, respectively. It is assumed that the hard seafloor, coupled with a noncentralized coring assembly, contributed to the buildup of angle. A complete drift survey was conducted while recovering Core 53R. The data indicated a dog leg at ~440 mbsf. Hole deviation continued to build from 8.25° at 40 mbsf to 18.5° at 440 mbsf and then declined to 14° at 640 mbsf.

A total of 350 bbl of sepiolite drilling mud was circulated during the coring operation, including spotting mud around the drill collars during DVTP measurements. A bottom-water temperature was taken with the APC temperature tool during the WSTP deployment, and then a total of six DVTP measurements were taken. These began after Core 7R and continued in ~50-m intervals during RCB coring. The

Table 2. Coring section summary for Site 1040.

Leg	Site	Hole	Core	Type	Top (mbsf)	Bottom (mbsf)	Advancement	Section number	Liner length (m)	Curated length (m)	Map interval top (mbsf)	Map interval bottom (mbsf)	Map type
170	1040	A	1	H	0	9.5	9.5	1	1.50	1.50	0.00	1.50	STD
170	1040	A	1	H	0	9.5	9.5	2	1.50	1.50	1.50	3.00	STD
170	1040	A	1	H	0	9.5	9.5	3	1.50	1.50	3.00	4.50	STD
170	1040	A	1	H	0	9.5	9.5	4	1.50	1.50	4.50	6.00	STD
170	1040	A	1	H	0	9.5	9.5	5	1.50	1.50	6.00	7.50	STD
170	1040	A	1	H	0	9.5	9.5	6	1.50	1.50	7.50	9.00	STD
170	1040	A	1	H	0	9.5	9.5	7	0.26	0.26	9.00	9.26	STD
170	1040	A	1	H	0	9.5	9.5	8	0.32	0.32	9.26	9.58	STD
170	1040	B	1	H	0	5.5	5.5	1	1.5	1.5	0	1.5	STD
170	1040	B	1	H	0	5.5	5.5	2	1.5	1.5	1.5	3	STD

Note: STD = standard. This is a sample of the table that appears on the volume CD-ROM.

last DVTP measurement was taken after Core 32R, because it was deemed unwise to risk the drill string and hole while sitting on bottom without circulation.

Above the décollement (Cores 1R through 19R), headspace methane levels varied from 4818 to 116,556 ppmv, whereas ethane levels were 5 to 65 ppmv. Propane varied from 3 to 24 ppmv. Vacutainer data indicated 50%–100% methane, whereas C_2 ranged from 226 ppmv to 1561 ppmv, and C_3 was 0–169 ppmv. Heavier hydrocarbons like *i*-C_4 ranged from 0 to 26 ppmv, and *i*-C_5 was 0–9 ppmv. There was geochemical evidence of hydrates in situ above the décollement; however, no hydrates were recovered in the cores. The hydrate stability zone for this site extended all the way to basement.

Below the décollement (Cores 20R through 51R), headspace methane levels dropped from 12,724 to 4 ppmv, and ethane levels went from 15 to 0 ppmv. Propane varied from 19 to 0 ppmv, with nothing over 1 ppmv after Core 21R. The only vacutainer data recovered below the décollement were for Core 21R. Methane indicated 98%, whereas C_2 was 781 ppmv, and C_3 was 76 ppmv. Heavier hydrocarbons like *i*-C_4 registered 29 ppmv, and *i*-C_5 was 1 ppmv. After that there was not enough gas to warrant vacutainer analysis. There was no geochemical evidence of hydrates in situ below the décollement.

Because there was interest in getting wireline sonic and Formation MicroScanner (FMS) logs (not available through LWD), it was decided that another wiper trip be made followed by two logging runs if the hole remained open. A wiper trip was completed to 4278.0 m (89.0 mbsf), noting a maximum overpull and drag of 40 and 30 kips, respectively. The bit was released, and the mechanical bit release (MBR) sleeve was reverse shifted to close off the dog ports. The hole was displaced with 220 bbl of sepiolite mud, and the open-ended pipe was positioned at 4292.8 m (103.8 mbsf) for logging.

The first suite of logs (sonic) was only able to advance to 129.2 m below the bit before being halted by a bridge or ledge in the hole. This interval was logged, and the tools were recovered, ending the wireline logging attempt. The open-ended pipe was run to a depth of 4480.1 m (291.1 mbsf), where the drag reached 35 kips. The trip was halted at that point and the hole was displaced with 80 bbl of 10.5 lb/gal mud. The drill pipe was pulled out of the hole, and the ship offset back to Site 1039, while the pipe trip continued to the surface.

Operations at Site 1039

The ship returned to Site 1039 to drill the LWD Hole 1039D (see "Operations" section, "Site 1039" chapter, this volume).

Hole 1040D

The LWD tools from the previous hole were removed from the rig floor, and new ones with fresh batteries were made up while the ship was moved in DP mode to Site 1040. Once the nuclear sources were loaded, the CDN and CDR tools were run to bottom. A Smith tricone F4 bit was run with 12/32-in and 14/32-in jets installed to allow coring of a limited amount of igneous rock. LWD Hole 1040D was spudded at 1830 hr, 20 November. Because of the very hard seafloor, very controlled drilling parameters were used. Weight-on-bit was limited to 2–4 kips, and the rotary speed was 30–45 rpm. Penetration rate for the first 40 m was 7.9 m/hr. Drilling proceeded relatively well, although the penetration rate (average = 14.6 m/hr) was hampered by continual bit balling and suspected balling around the LWD stabilizer. At a depth of 279.8, pump pressure and torque increased, and generous sepiolite mud sweeps did little to correct the condition. Drilling continued to a depth of 308.7 mbsf, and hole conditions continued to deteriorate. A wiper trip was made to 103.6 mbsf with overpulls of 20 kips and 300–500 psi back pressure prevalent to 214.0 mbsf. On the way back to bottom, there was 10–15 kips of pipe drag in the hole. In all, a total of 10½ hr was spent on remedial work attempting to stabilize the hole. Drilling resumed, and the hole was deepened to a depth of 4526.5 m (337.5 mbsf), taking care to double-ream the hole between each connection. Continued hole trouble resulting in eventual stuck pipe forced a halt to drilling operations at a total depth (TD) of 337.5 mbsf. An overpull of 50 kips was required to free the drill string.

Suspected hole deviation and possible formation overpressure was suspected as the primary cause for failure to achieve the depth objective. After pulling pipe to a "safe" depth of 4475.0 m (286.0 mbsf), the Tensor electronic multishot was deployed for a drift survey of the hole. Because of poor hole conditions and the nuclear sources installed in the LWD tools, the lowest data point recorded was at 271.0 mbsf, which was 66.5 m above hole TD. Drift data indicated that the hole was started at an angle of 7.6° from vertical and proceeded to straighten with depth. The angle was 2.9° at a depth of 271.0 mbsf. After completing the survey, the pipe was again found to be stuck. This time 25-kips overpull was required to free the string. The hole was displaced with 10.5 lb/gal mud, and the drill string tripped back to the surface. Once the nuclear sources were removed from the LWD tools, the bit was pulled to the rig floor. The log data were transferred from the tools to a workstation computer for plotting and analysis. Subsequent analysis of the LWD log data by the logging engineer confirmed a probable overpressurized zone in the hole extending from a depth of 281.0 mbsf to TD.

Hole 1040E

Hole 1040E was located 30 m north of Hole 1040D. This was to be another attempt at getting LWD logs down to and across the décollement. The CDN and CDR tools were changed out for those with fresh batteries, and the same tricone drag bit that was run successfully in Hole 1039D was used. It was hoped that a faster penetration rate and a straighter hole would allow this hole to reach a deeper TD. Drilling in this hole proceeded at a much faster ROP with the more

efficient drag type bit. The first 221.9 m was drilled at an average ROP of 30.6 m/hr. Drilling continued without incident until a depth of around 280 mbsf. At that point, the same type of hole problems that were encountered in Hole 1049D occurred. Pump pressure (400- to 500-psi back pressure) and drilling torque were higher, and a tight hole (20–30 kips) was the rule rather than the exception. The hole was advanced to a depth of 4507.4 m (318.4 mbsf), with the drill string sticking every time a connection was made, and it became apparent that the hole would not be drilled much further. To avoid a potential loss of the expensive LWD tools, the hole was terminated. The drill string was raised to 247.9 mbsf, and the hole was displaced with 10.5 lb/gal mud. The pipe was pulled clear of the seafloor at 1130 hr. The vessel immediately got underway in DP mode for Site 1041, while the LWD tools were removed from the rig floor and the APC/XCB BHA was made up for the next site.

LITHOSTRATIGRAPHY AND STRUCTURES

Site 1040 was drilled to investigate the lithostratigraphy and structural geology of the sedimentary wedge, décollement zone, and underthrust section imaged in multichannel seismic-reflection data (see "Introduction" section, this chapter). A primary goal was correlation of the wedge and underthrust section to the reference incoming section drilled at Site 1039. Coring in three holes from the seafloor to a gabbroic intrusion at 653 mbsf recovered deformed sediments and sedimentary rocks from both wedge and underthrust domains.

Description of Lithostratigraphic Units

The cores recovered at Site 1040 include four sedimentary lithologic units and one igneous unit (Fig. 1; Table 3). Because the units of the underthrust section below the décollement correspond to those of the reference section at Site 1039, we chose to subdivide the lithologic unit names into two groups. Those units designated "P" belong to the prism-shaped sedimentary wedge (0–371 mbsf), and those designated "U" make up the underthrust section (371–653 mbsf). We chose this format to preserve the same unit designations for the underthrust section as at Site 1039. Intervals cored at Site 1040 include 0–9.5 mbsf in Hole 1040A (Core 170-1040A-1H), 0–190.3 mbsf in Hole 1040B (Cores 170-1040B-1H through 170-1040B-22X), and 159.3–665.0 mbsf in Hole 1040C (Cores 170-1040C-1R through 170-1040C-53R). Core recovery was generally good to excellent (44%–108%), except in the uppermost 65 mbsf in Hole 1040B (7%–100%).

Unit P1: Silty Clay(stone)

Intervals: 170-1040A-1H-1, 0 cm, to 1H-CC, 32 cm; 170-1040B-1H-1, 0 cm, to 22X-4, 148 cm; 170-1040C-1R through 22R
Thickness: 371.2 m
Depth: 0–371.2 mbsf
Age: Pliocene–?Pleistocene

Subunit P1A: Silty Clay to Clayey Silt with Debris Flows and Silty Sands

Intervals: 170-1040A-1H-1, 0 cm, to 1H-CC, 32 cm; 170-1040B-1H-1, 0 cm, to 10X-1, 40 cm
Thickness: 74.8 m
Depth: 0–74.8 mbsf
Age: Pliocene–?Pleistocene

Subunit P1B: Silty Clay(stone)

Intervals: 170-1040B-10X-1, 40 cm, to 22X-4, 148 cm; 170-1040C-1R-1, 0 cm, through 22R
Thickness: 296.4 m
Depth: 74.8–371.2 mbsf
Age: Pliocene–?Pleistocene

This unit consists primarily of homogeneous olive green to dark olive green silty clay to claystone, divided into Subunits P1A and P1B. Subunit P1A is defined by the presence of common matrix-supported sedimentary breccias and rare silty sand beds. These beds form minor layers intercalated with a fine-grained sediment of silty clay to clayey silt, mostly massive with few distinct bedding planes, and few trace fossils. Sedimentary breccias are composed of angular to subrounded pebble-sized clasts of firm olive green silty clay in a matrix of either softer silty clay of similar lithology (Fig. 3), or a coarser grained sandy silt. Many of the breccias, notably at interval 170-1040B-7X-1, 0–20 cm, include rock fragments of andesite, sandstone, and tuff. A minor proportion of the clasts are yellow-brown to greenish brown calcareous silty clay. These breccias make up about half of the recovered material near the surface, diminishing to ~10% below 25 mbsf.

Silty clays of Subunit P1A typically are dominated by abundant clay or clay-sized grains, associated with significant amounts of quartz, plagioclase feldspar, and volcanic glass (Table 4). Plagioclase is 2–3 times more abundant than quartz. Microfossils are generally rare, with diatoms, nannofossils, radiolarians, and sponge spicules absent or present only in trace amounts. Volcanic glass is ubiquitous as a minor component of the sand- and silt-sized fraction. Thin beds of ash or, more typically, bioturbated pods and burrow-fills of ash,

Table 3. Site 1040 lithostratigraphic units.

Unit	Subunit	Intervals	Thickness (m)	Depth (mbsf)	Age
P1: silty clay (stone) (0-371.2 mbsf)	P1A: olive green silty clay to clayey silt with debris flows and silty sands	1040A-1H-1, 0 cm, to 1H-CC, 32 cm 1040B-1H-1, 0 cm, to 10X-1, 40 cm	74.8	0-74.8	Pliocene to ? Pleistocene
	P1B: olive green silty clay(stone) with intervals of silt-very fine sand	1040B-10X-1, 40 cm, to 22X-4, 148 cm 1040C-1R-1, 0 cm, to 22R	296.4	74.8-371.2	Pliocene to ? Pleistocene
U1: clayey diatomite (371.2- 422.6 mbsf)	U1A: clayey diatomite with with silty sand interbeds	1040C-23R-1, 0 cm, to 24R-3, 80 cm	13.2	371.2-384.4	<0.20 Ma
	U1B: clayey diatomite with ash layers	1040C-24R-3, 80 cm, to 28R-3, 50 cm	38.2	384.4-422.6	middle to late Pleistocene
U2: silty claystone (422.6-479.7 mbsf)	U2A: silty claystone with ash layers	1040C-28R-3, 50 cm, to 33R-4, 98 cm	49.87	422.6-472.47	early Pliocene to middle Pleistocene
	U2B: silty claystone with calcareous clay, ash layers	1040C-33R-4, 98 cm, to 34R-3, 0 cm	7.23	472.47-479.7	late Miocene to early Pliocene
U3: siliceous nannofossil chalk (479.7-653.5 mbsf)	U3A: siliceous nannofossil chalk and claystone	1040C-34R-3, 0 cm, to 36R-2, 30 cm	18.1	479.7-497.8	late Miocene
	U3B: siliceous nannofossil chalk	1040C-36R-2, 30 cm, to 44R-1, 25 cm	75.55	497.8-573.35	middle to late Miocene
	U3C: nannofossil chalk, diatomite, and breccia	1040C-44R-1, 25 cm, to 52R-3, 53 cm	80.18	573.35-653.53	middle Miocene
U4: pyroxene gabbro (653.53-661.47 mbsf)		1040C-52R-3, 53 cm, to 53R-2, 37 cm	7.94	653.53-661.47	Post-15.6 Ma

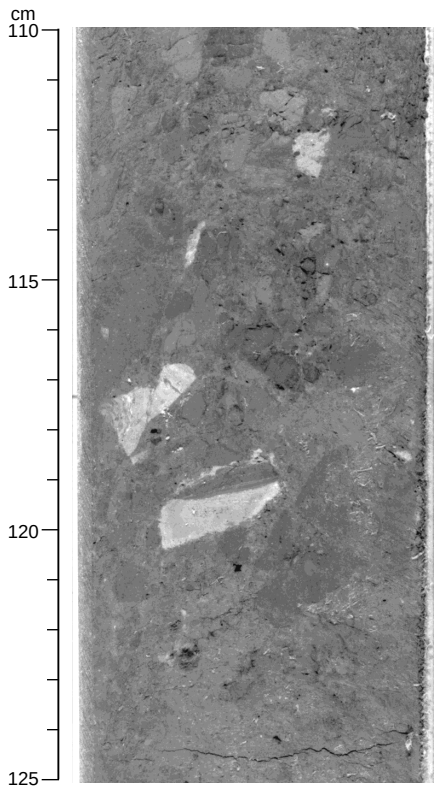

Figure 3. Example of sedimentary breccia with light and dark angular mud and calcareous mud clasts (e.g., 117–120 cm) typical of Subunit P1A (interval 170-1040B-2H-2, 110–125 cm).

are present at a frequency of 2–5 per 9.5-m core. These ashes are light gray to grayish green, crystal-lithic-vitric ashes composed predominantly of clear, unaltered to weakly altered volcanic glass, pumice, quartz, feldspar, and clay, in some cases with amphiboles. Virtually all ashy layers are mixed with clay and traces of microfossils, suggesting partial reworking by bioturbation and/or submarine transport.

The uppermost 30 m of Subunit P1A, as well as the interval from 64.8 to 69 mbsf (Sections 170-1040B-9X-1 through 9X-3) include sandy silt and silty sand lithologies in thicknesses from several tens of centimeters to several meters. These poorly sorted, sand- and silt-rich intervals typically have no clear grading or basal scour (although such features may have been obliterated by extensive bioturbation). They consist mainly of quartz, feldspar, volcanic glass, and lithic fragments (tephra, limestone, and feldspathic-lithic sandstone lithologies). Glauconite, phosphate, carbonate grains, fish debris, and microfossils occur as minor components.

Subunit P1B is distinguished from Subunit P1A by the absence of sedimentary breccia interbeds; the major lithology remains unchanged. In Subunit P1B, the composition of the sediments determined from smear slides remains unchanged throughout nearly the entire depth interval. All of the cores of this subunit were extensively disturbed by drilling as well as by varying amounts of tectonic deformation, which would have obliterated most macroscopic sedimentary structures present. However, intact intervals of core exhibit a few examples of *Zoophycos* and other burrow traces, and only rare bedding planes. The nearly 200-m interval of Subunit P1B is composed of homogeneous silty claystone with few ash layers. Macroscopically, we distinguish a subtle color-based alternation in the cores, varying from olive green to dark olive green silty claystone, typically over a scale of approximately 1–2 m. Smear-slide analysis does not reveal any significant difference between sediments of the two shades, but the lighter olive green claystones appear to contain slightly more carbonate, based on HCl reaction. Neither is shown to be carbonate rich by bulk carbonate analysis (see "Geochemistry" section, this chapter). All of the sedimentary wedge data indicate that the $CaCO_3$ content is below 8 wt%.

Deviations from the clay-rich lithology occur only in a few notable intervals in Subunit P1B. In Sections 170-1040B-11X-1 and 11X-4 (85 and 88.5–89.1 mbsf), we noted dark olive green fine- to medium-sized silty sand that was finely bedded (1–3 mm spacing) and dominated by volcanic glass and volcanogenic rock fragments. Similar silty sandstones are present in Sections 170-1040B-16X-4 and 16X-5. Rare sandy silt horizons also were noted between 159.3 and 197.6 mbsf, in Cores 170-1040C-1R through 4R. From that depth to 279.7 mbsf, the lithology is very homogeneous, with few ash layers interspersed in 80 m of olive green silty clay. Between 279.7 and 303 mbsf, there are interbeds of sandy silt and clayey silt, 20–50 cm thick, with minor carbonates. From 303 mbsf to its base at 371.2 mbsf, Unit P1 is all homogeneous silty clay or silty claystone (induration state varies in this interval). Discrete ash layers are nearly absent over this interval, with the notable exception of the base of the unit from 356.1 to 371.2 mbsf, where dark reddish brown, yellow-brown, and dark gray lithic-vitric ashes form a significant minor component of the sediment. These ashes occur both in discrete, folded layers and mixed with the silty clay; it is unclear whether the folding and mixing are partially natural or are entirely products of the extreme drilling disturbance in this interval.

Framboidal pyrite is the most common diagenetic mineral, forming a minor to trace component throughout Unit P1. Macroscopic pyrite cubes are rare in Unit P1 but are notably more concentrated in interval 170-1040C-22R-6, 88–111 cm (370 mbsf). Very fine veinlets, less than 1 mm thick, of dark red and black minerals are present in intervals 170-1040C-19R-4, 41–42 cm and 62–64 cm (337.5–337.7 mbsf), and 170-1040C-20R-4, 53–55 cm (347.1 mbsf). Based on macroscopic color and appearance, these veinlets are most likely manganese oxide with rhodochrosite or siderite. Common to trace amounts of fine silt-sized dolomite rhombs were observed in smear slides from Cores 170-1040C-5R and 6R (198–217 mbsf), along with a dolomitic vein or concretion in Core 170-1040C-6R. Traces of dolomite were also noted from 265 to 275 mbsf and, rarely, to 375 mbsf.

Summary and Inferred Depositional Environment

In summary, Unit P1 is a relatively massive silty clay/claystone interbedded with a few minor ashes and thin silty and sandy layers. The homogeneous nature of the sediments is confirmed by results of shipboard X-ray fluorescence (XRF) analysis (see "Geochemistry" section, this chapter), and LWD logging results in the interval 0–330 mbsf (see "Physical Properties" section, this chapter). The predominantly fine-grained terrigenous character of the components of Unit P1, lacking clear grading or bedding, is consistent with a deep-water hemipelagic origin on the lower continental slope or in the trench. The composition of the bedded sands and silts also indicates a terrigenous siliciclastic origin, attributed to submarine gravity flow in turbidity currents. The numerous sedimentary breccias and rare slump folds from 0 to 75 mbsf suggest that downslope mass transport processes (i.e., slumping and gravity flow) have mixed and reworked at least the uppermost part of Unit P1. Both downslope transport and bioturbation may have contributed to the mixing and disruption of ash and sand layers.

Unit U1: Clayey Diatomite

Interval: 170-1040C-23R-1, 0 cm, to 28R-3, 50 cm
Thickness: 51.6 m
Depth: 371.2–422.8 mbsf
Age: middle–late Pleistocene

Subunit U1A: Clayey Diatomite with Silty Sand Interbeds

Interval: 170-1040C-23R-1, 0 cm, to 24R-3, 80 cm
Thickness: 13.2 m

Table 4. Site 1040 smear-slide descriptions.

Sample number							Depth	Imp.		Size				Composition																				Fossils										Sediment or rock name	Comment
Leg	Site	Hole	Core	Type	Section	Interval (cm)	mbsf	Major lithology	Minor lithology	Med.-coarse sand	Fine sand	Silt size	Clay size	Quartz	Feldspar	Clay	Mica	Rock fragments	Volcanic glass	Amphibole	Olivine	Glauconite	Phosphate	Zeolites	Dolomite	Carbonate	Micrite	Opaque	Framboid	Iron oxide	Other	Nannofossils	Foraminifers	Diatoms	Radiolarians	Silicoflagellates	Sponge spicules	Shell debris	Fish remains	Peloids/pellets	Organic matter	Unidentified		
170	1040	A	1	H	1	5	0.05		X	C	A	C	C	C	C	C		A	C			A	T			T	T	C			T					T					Dark olive gray silty sand with tephra and glauconite	Rock fragments are pumice. Glauconite-filled foraminifers or diatoms comprise most of the sand and coarse silt.
170	1040	A	1	H	2	30	1.80		X		C	C	T	T	T	T		A	C			C	T			C	C	T	C			C	C	T	T		T		T			Calcareous sandy silt with glauconite clasts and ash	Pollen. Rock fragments are pumice. Sand is glauconite.
170	1040	A	1	H	2	55	2.05	X				C	A	T	T	A		T	C			T	C			T						T					T		T			Dark olive green silty clay	Pollen. Rock fragments are pumice.
170	1040	B	1	H	1	10	0.10		X		C	C	C	T	T	C		C	C				C			T	T	T	T			T		A		T	T		T			Reddish brown diatomaceous ooze with phosphatic sand and ash	Rock fragments are pumice. Phosphate is nodular, oblong to round, fine sand and coarse silt. Some phosphate fills diatom or foram tests.
170	1040	B	1	H	1	50	0.50	X			T	C	A	C	T	C		A	C			T	C			C		T	T			T	T	T								Olive green clay with phosphatic silt and ash.	Some tests filled with pyrite framboids or phosphate.
170	1040	B	2	H	2	30	7.30		X		T	A	A	C		A	T		A	T		T	T+			T			T				T	T			T		C-	C		Olive green clayey silt with abundant volcanic detritus and fecal pellets	
170	1040	B	2	H	2	68	7.68		X		T	C	A	T	T+	A	T	C-	C-	T		T	T					T	T					T	T		T		T			Clay with lithic-vitric ash	
170	1040	B	2	H	4	38	10.38	X			T	A	A	C	T	A			C	T			T			T						T		T	T		T		C-	C	T	Olive green silty clay with volcanic glass and fecal pellets	Trace of pollen
170	1040	B	2	H	4	110	11.10		X		T	C	A	C	T	A			C			T	T			T								T					C-	T	T	Silty clay with volcanic glass	
170	1040	B	3	X	CC	10	14.10	X				C	A	T	T	A		T	C			C	T			T		T	T			T		T	T		T		T	T		Silty clay	

Notes: Imp. = important. A = abundant, C = common, T = trace, and blank box = not observed.

This is a sample of the table that appears on the volume CD-ROM.

Depth: 371.2–384.4 mbsf
Age: <0.20 Ma

Subunit U1B: Clayey Diatomite with Ash Layers

Interval: 170-1040C-24R-3, 80 cm, to 28R-3, 50 cm
Thickness: 38.2 m
Depth: 384.4–422.6 mbsf
Age: middle–late Pleistocene

The top of Core 170-1040C-23R lies at an abrupt boundary between the barren, deformed hemipelagic sediments of the wedge and a strongly biogenic section analogous to that encountered at Site 1039, here interpreted as the underthrust reference section. The stratigraphic succession between this boundary and 653.53 mbsf is nearly identical (except in thickness and lithification state) to that at Site 1039 and is laterally continuous with it in seismic-reflection data (see Fig. 2). The reader is referred to the "Lithostratigraphy and Structures" section, "Site 1039" chapter (this volume) for detailed descriptions of the lithologies. Only significant departures from the reference section at Site 1039 are discussed here.

Subunit U1A consists of dark olive green clayey diatomite with common silty sand interbeds. Because lithification is much greater here than at Site 1039, we use the name "diatomite" rather than "diatomaceous ooze." At both sites, the major components in sediments of this unit are diatoms, but it is more clay rich than a true diatomite (Table 4). In interval 170-1040C-24R-1, 104–115 cm, a graded bed of mud clasts and coarse to fine sand, silt, and clay is interpreted as a turbidite similar to those of Subunit U1A at Site 1039 (Fig. 4). This unit exhibits better preserved bedding and burrows than Unit P1. Diatoms, radiolarians, silicoflagellates, and sponge spicules are abundant to common as are *Zoophycos* burrows, except in the sandy intervals. Subunit U1A appears to be broadly correlative with Subunit U1A at Site 1039, although the spatially variable nature of turbidite deposition and the plate motion through the trench axis suggest the unit may be diachronous from Sites 1039 to 1040. The base of Subunit U1A is marked by the lowest observed sand bed.

Subunit U1B is dark green clayey diatomite to siliceous claystone with ash layers, equivalent to Subunit U1B at Site 1039 except that it is thinner, more indurated, and exhibits more deformation (discussed below in the "Structural Geology" section). *Zoophycos* burrows and siliceous and calcareous microfossils are ubiquitous. All of Unit U1 contains common authigenic pyrite.

Unit U2: Silty Claystone

Interval: 170-1040C-28R-3, 50 cm, to 34R-3, 0 cm
Thickness: 57.10 m
Depth: 422.6–479.7 mbsf
Age: late Miocene–middle Pleistocene

Subunit U2A: Silty Claystone with Ash Layers

Interval: 170-1040C-28R-3, 50 cm, to 33R-4, 98 cm
Thickness: 49.87 m
Depth: 422.6–472.47 mbsf
Age: early Pliocene–middle Pleistocene

Subunit U2B: Silty Claystone with Calcareous Claystone and Ash Layers

Interval: 170-1040C-33R-4, 98 cm, to 34R-3, 0 cm
Thickness: 7.23 m
Depth: 472.47–479.7 mbsf
Age: late Miocene–early Pliocene

The boundary between Units U1 and U2 is gradational over a 2- to 3-m interval in Sections 170-1040C-28R-2 through 28R-3 and is placed at the uppermost point where smear-slide examination indicates the major lithology is siliciclastic rather than strongly biogenic.

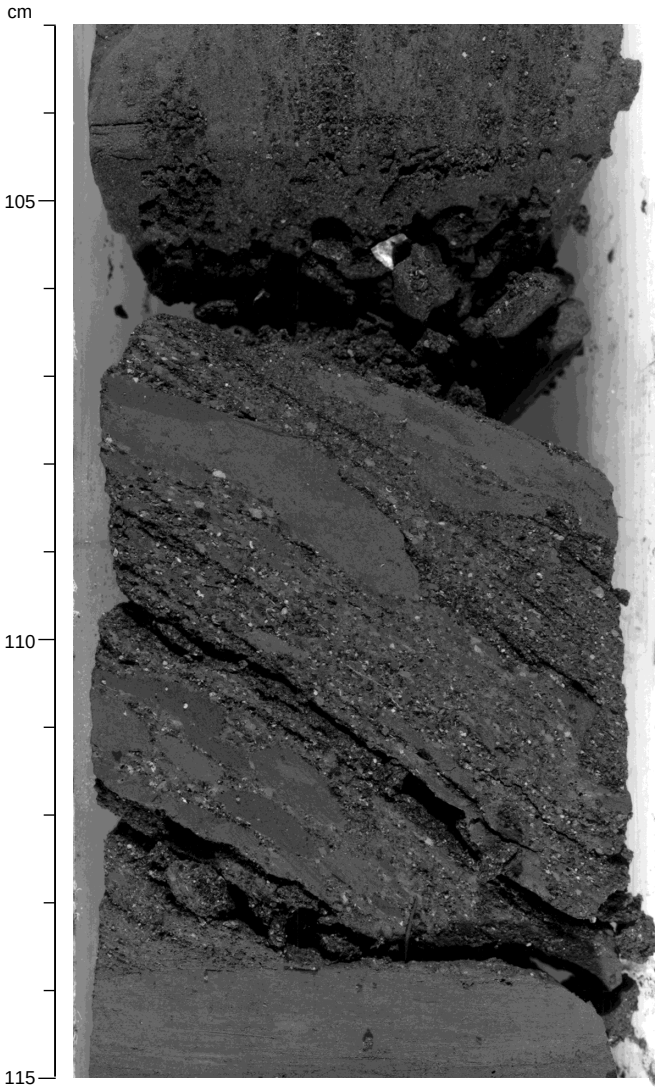

Figure 4. Poorly sorted bed of coarse sand- to granule-sized mud clasts interpreted as a turbidite, just below the décollement zone, Subunit U1A (interval 170-1040C-24R-1, 103–115 cm).

Unit U2 is predominantly silty claystone to silty claystone with calcareous clay; ash layers are common. Unit U2 is of the same composition as the equivalent unit at Site 1039 but is more indurated and exhibits a greater number of minor faults. Subunit U2A lacks interbeds of calcareous claystone, whereas Subunit U2B is transitional between the predominantly siliciclastic Subunit U2A and predominantly biogenic Subunit U3A. Subunit U2B includes interbedded light green to greenish gray calcareous claystones alternating with the darker silty clays. Nannofossils are common to abundant in this subunit. Based on smear-slide observations as well as carbonate analyses and spectrophotometer lightness component data, Subunit U2B is substantially thinner here than at Site 1039, being 7.23 m thick compared to 19.62 m at Site 1039.

Unit U3: Siliceous Nannofossil Chalk

Interval: 170-1040C-34R-3, 0 cm, to 52R-3, 53 cm
Thickness: 173.83
Depth: 479.7–653.53 mbsf
Age: middle–late Miocene

Subunit U3A: Siliceous Nannofossil Chalk and Claystone

Interval: 170-1040C-34R-3, 0 cm, to 36R-2, 30 cm
Thickness: 18.1
Depth: 479.7–497.8 mbsf
Age: late Miocene

Subunit U3B: Siliceous Nannofossil Chalk

Interval: 170-1040C-36R-2, 30 cm, to 44R-1, 25 cm
Thickness: 75.55 m
Depth: 497.8–573.35 mbsf
Age: middle–late Miocene

Subunit U3C: Nannofossil Chalk, Diatomite, and Breccia

Interval: 170-1040C-44R-1, 25 cm, to 52R-3, 53 cm
Thickness: 80.18 m
Depth: 573.35–653.53 mbsf
Age: middle Miocene

Unit U3 consists of the almost entirely biogenic siliceous nannofossil chalk, which makes up the rest of the sedimentary section down to the gabbro intrusions of Unit U4 at the base of Hole 1040C. The entire section is dominated by nannofossils and diatoms and is extensively bioturbated, primarily by *Zoophycos* burrows. The top of Subunit U3A is marked by a color change to gray and light gray and is primarily identified by a change in the dominant component of the sediment to nannofossils. As with Units U1 and U2, the lithologies are analogous to their equivalents at Site 1039 but are thinner and more indurated. The 18.1-m-thick Subunit U3A records a transition from the mixed terrigenous clayey and biogenic sediment of Unit U2 to the biogenic sediment of Subunit U3B. Terrigenous components decrease in abundance downhole through this subunit until they nearly disappear below 497.8 mbsf. Siliceous microfossils, most commonly diatoms but also radiolarians and sponge spicules, increase in abundance downsection throughout Subunit U3A.

The top of Subunit U3B is marked by the abrupt change in color to ivory white or light gray siliceous nannofossil chalk, corresponding to an increase in carbonate content to over 50 wt%. Although nannofossils are most abundant, siliceous microfossils, especially diatoms, are a major component of the chalk (Table 4). As at Site 1039, the color of the cores is variegated, including bands and patches of brownish yellow, green, lavender, and dark gray against the background of ivory. Purplish black liesegang bands and rings are ubiquitous. As at Site 1039, no clear compositional differences in the various bands could be discerned through smear-slide analysis. Distinct volcanic ashes are rare in much of this subunit but become more common in the lowermost 100 m of the unit, increasing in abundance to the base of the recovered sedimentary section. Volcanic glass is a ubiquitous trace component even in the biogenic sediment.

Subunit U3C is defined by distinctive interbeds of brown and greenish gray diatom-rich chalks and diatomites, as well as rare interbeds of mixed sediment, containing subequal amounts of mixed ash and nannofossils. Minor sedimentary breccias are found in the lowermost 15 m of the subunit. The top of the subunit is defined at the uppermost brown diatomite interbed in Core 170-1040C-44R. As at Site 1039, most of the section is nannofossil chalk (here it is more lithified than the ooze at Site 1039). Sections 170-1040C-51R-1, 51R-4, 52R-1, and 52R-3 contain accumulations of vitric and lithic-vitric ash up to 40 cm thick, and the nannofossil chalk is mixed with major proportions of volcanic glass, tephra, and glassy lithic fragments. These chalky tuffs/tuffaceous chalks are similar to but of different age from those identified in the same subunit in Holes 1039B and 1039C, based on magnetostratigraphy. Graded deposits of biogenic material mixed with ash suggest turbidity-current deposition. In Section 170-1040C-51R-4, several 10- to 15-cm-thick intervals of sedimentary breccia interpreted as debris flow deposits were identified (Fig. 5). At 653.53 mbsf (interval 170-1040C-52R-3, 53 cm), two 3- to 5-cm-thick pieces of hard rock next to the gabbroic intru-

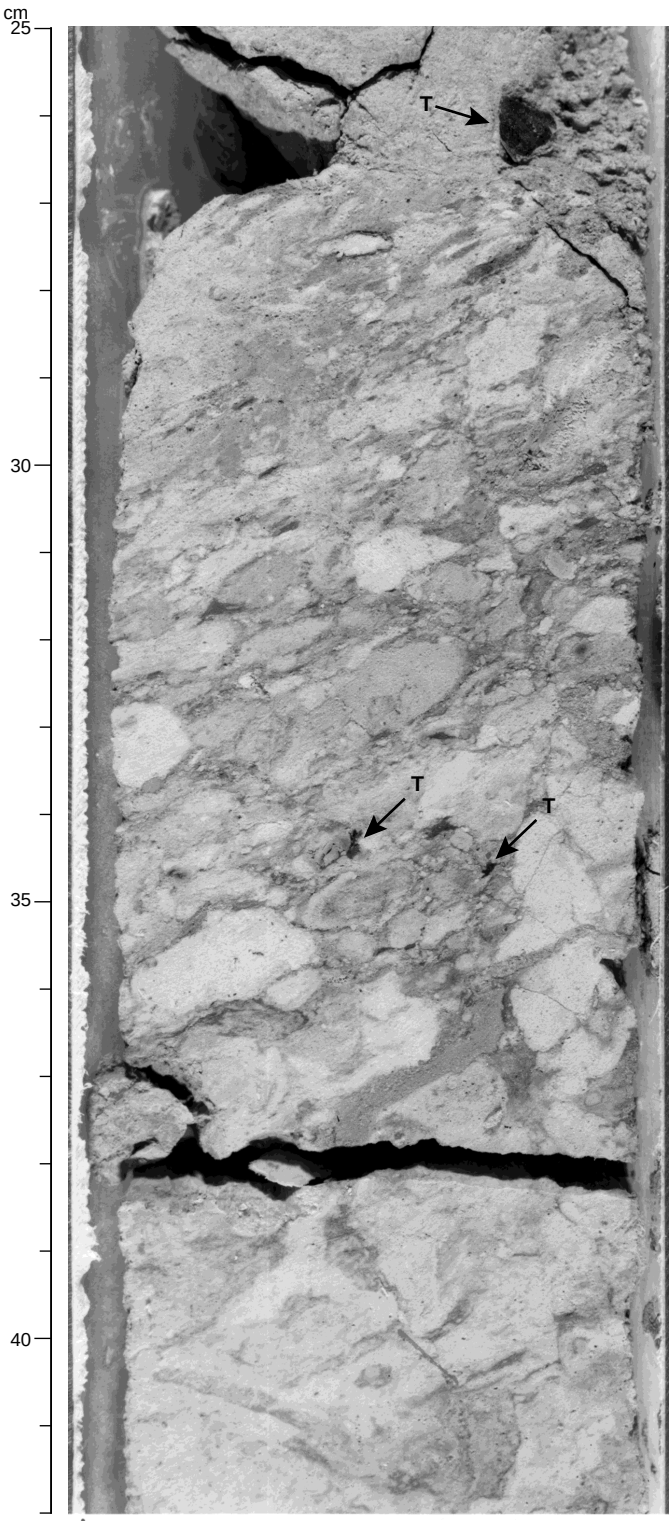

Figure 5. Layer of sedimentary breccia 9 m above gabbroic intrusion, lowermost part of Subunit U3B. Note the large black, glassy tephra clast (“T”) at 26 cm and smaller ones at 34–35 cm (interval 170-1040C-51R-4, 25–42 cm).

sion of Unit U4 contain glass and carbonate, suggesting baked sediment.

Unit U4: Pyroxene Gabbro

Interval: 170-1040C-52R-3, 53 cm, to 53R-2, 37 cm
Thickness: 7.94 m
Depth: 653.53–661.47 mbsf
Age: post-15.6 Ma

Unit U4 consists entirely of pyroxene gabbros, closely similar to those at Site 1039 (see "Lithology and Structures" section, "Site 1039" chapter, this volume). They are fine-grained pyroxene (augite) gabbros with medium plagioclase or plagioclase plus pyroxene glomerophenocrysts (Fig. 6). Grain size, mineral composition, and visually estimated mineral proportions are in the same ranges reported for Site 1039 (Table 5). The Site 1040 gabbros typically consist of 10%–20% glomerophenocrysts and pyroxene grains up to 1.2 mm in size (Table 5). Therefore, they are petrographically similar to the gabbros recovered from the base of the gabbro section at Site 1039 (below 448 mbsf). Glass pockets and veins constitute 5%–50% of the Site 1040 gabbros. The glass is pervasively palagonitized, often chloritized, and commonly contains zeolites. Gabbros at Site 1040 appear to be more extensively altered in both thin section and hand sample than those at Site 1039. Mineral textures that suggest a partial cumulate origin for the Site 1039 gabbros are also present at Site 1040. Chemically, the Site 1040 gabbros appear to be slightly less fractionated than those at Site 1039, with lower TiO_2 contents and lower abundances of oxide minerals (see "Geochemistry" section, this chapter).

One intrusive unit is recognized at Site 1040. It is topped by a 5-cm-thick layer of cryptocrystalline sugary glass. In thin section, this glass is largely microcrystalline quartz plus clear glass, with minor stringers and pods of variably resorbed carbonate, recording the intrusive contact. Compositionally, this glass is almost pure SiO_2, with minor amounts of Ca, Fe, and Al.

Structural Geology

Structural observations and measurements made at Site 1040 (Table 6; Fig. 7) indicate that the 653 m of sediment overlying the gabbro intrusion can be divided into two distinct structural domains. Domain I is the slightly to strongly deformed but lithologically homogenous sedimentary wedge, extending from the seafloor to the base of the décollement zone at 371 mbsf. Domain II extends from just below the décollement to the bottom of Hole 1040C. Domain IIA includes the interval from the décollement to the base of Unit U2 (371–480 mbsf); it is characterized by much less deformation than the wedge but exhibits significant bedding dip, steepening toward the bottom. Domain IIB is the interval from 480 to 665 mbsf, consisting of apparently flat-lying, compacted, but relatively little deformed (except right at the base) siliceous chalks.

Several operational factors presented obstacles to detailed structural analysis of the cores, especially those from Domain I, the sedimentary wedge. Core recovery in Hole 1040B was very poor over the uppermost 70 m of coring, and XCB cores below this to the total depth of 190.3 mbsf exhibit extensive drill biscuiting disruption. The remaining cores from 190 to 665 mbsf were collected in Hole 1040C, which is known to be significantly inclined with respect to vertical based on Tensor tool measurements taken inside the drill string (see "Operations" section, this chapter). Inclination is almost 8° very close to the seafloor, increases to a maximum of nearly 19° at the depth of the décollement zone, and then decreases to about 15° at 650 mbsf. The azimuth of the inclination is 270° in the wireline-logged interval, 105–230 mbsf. The nonverticality of the long axis of the cores has a devastating effect on structural interpretation, because it introduces up to ±19° uncertainty in the measured attitudes. Furthermore, even though the azimuth is known, the inclination precludes paleomagnetic reorientation of the structures into geographic coordinates except where strike of features can be assumed a priori. The third obstacle is apparently caused by the Hole 1040C RCB coring, which produced a form of extreme drilling disturbance manifested as quasi-continuous torsional plastic deformation of the cores over intervals of many meters (Fig. 8; see also "Biostratigraphy and Magnetostratigraphy" section, this chapter) referred to here as "spiral drill disturbance." This disturbance renders suspect all structural information recorded in these intervals, primarily 190–371 mbsf. The net effect of these complications is that we recorded very little reliable structural information in the sedimentary wedge domain; unfortu-

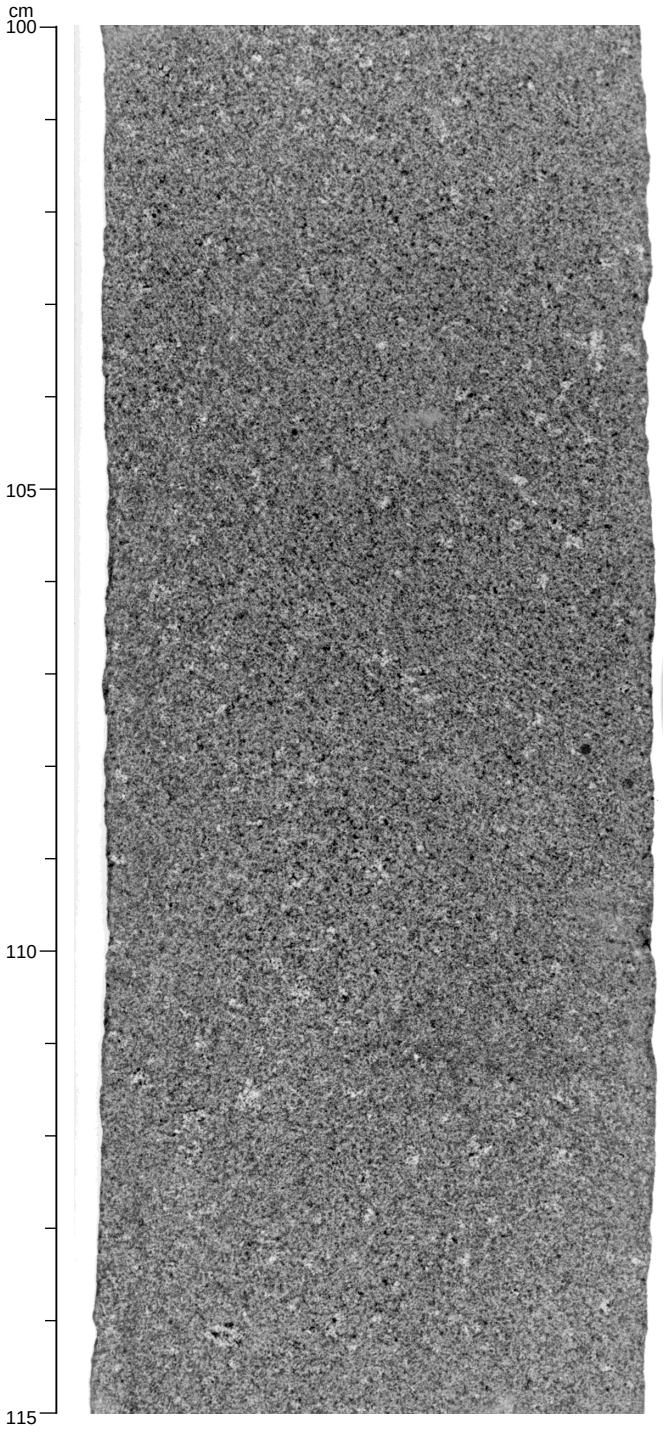

Figure 6. Pyroxene gabbro with large light-colored plagioclase-pyroxene glomerophenocrysts, typical of Unit U4 (interval 170-1040C-53R-1, 100–115 cm).

Table 5. Thin-section summary for gabbros.

Site	Hole	Core	Section	Top (cm)	Piece	Depth (mbsf)	Rock type	% Glom	Size, glom	% Plag	Size, laths	% Cpx	Size, cpx	% Glass	% Alt	Comments
1040	C	52R	3	56	8	653.6	Baked sediment							1	1	Quartz and carbonate-rich glass
1040	C	52R	4	5	2	653.6	Gabbro	15	3	15	0.25	1	1	50	48	Glass-rich layer in section
1040	C	52R	4	62	8	654.2	Gabbro	28	6	30	0.3	30	0.15	5	8	Plag, plag+ cpx and cpx glomerocrysts
1040	C	53R	1	15	1A	659.7	Gabbro	10	2	15	0.25	5	1.2	30	31	Plag, plag+ cpx and cpx glomerocrysts
1040	C	53R	1	37	1A	660	Gabbro	3	5	35	0.5	2	0.25	5	6	Plag, plag+ cpx and cpx glomerocrysts
1040	C	53R	2	28	4		Gabbro	7	4	25	0.15	3	0.4	10	15	Plag, plag+ cpx and cpx glomerocrysts

Notes: Glom = glomerocryst, plag = plagioclase, cpx = clinopyroxene, and alt = alteration. Grain sizes in millimeters.

Table 6. Site 1040 structural summary.

Site	Hole	Core	Type	Section	Top (cm)	Bottom (cm)	Depth (mbsf)	Cr az.	Cr dip	Cr line	Cr l.dip	Cr sense	Pm az.	Pm dip	Pm line	Pm l.dip	Sense
1040	B	2	H	2	26	27	7.26	27	62				140	38			
1040	B	2	H	2	86	88	7.86	210	74				60	34			
1040	B	2	H	4	39	41	10.39	34	80				108	35			
1040	B	2	H	4	65	70	10.65	46	82				101	47			
1040	B	6	X	2	28	31	38.18	145	72				300	39			
1040	B	6	X	2	29	31	38.19						303	41			
1040	B	6	X	2	57	59	38.47	250	29				28	80			
1040	B	6	X	2	59	63	38.49	253	78				77	73			
1040	B	6	X	2	59	63	38.49						80	74			
1040	B	9	X	4	60	60	69.62	122	84				277	58			

Notes: Cr az. = core reference azimuth, cr dip = core reference dip, cr line = core reference lineation, cr l.dip = core reference lineation dip, cr sense = core reference sense, pm az. = paleomagnetic azimuth, pm dip = paleomagnetic dip, pm line = paleomagnetic lineation, pm l.dip = paleomagnetic lineation dip, Sense = sense of movement in paleomagnetic reference frame, Conf. = confidence, and Half = core half (W = working half, A = archive half). MMT = tool designed by Martin Mesch, and Protr. = protractor. Bedd. = bedding, frac. = fracture, and fiss. = fissility.

Table 6 (continued).

Site	Hole	Core	Type	Section	Top (cm)	Bottom (cm)	Depth (mbsf)	Conf.	Half	Tool	Identifier
1040	B	2	H	2	26	27	7.26		W	MMT	Bedd.
1040	B	2	H	2	86	88	7.86		W	MMT	Bedd.
1040	B	2	H	4	39	41	10.39		W	MMT	Bedd.
1040	B	2	H	4	65	70	10.65		W	MMT	Bedd.
1040	B	6	X	2	28	31	38.18		W	MMT	Bedd. (same plane as below, measured with MMT)
1040	B	6	X	2	29	31	38.19		W	Protr.	Bedd. (same plane as above, measured with protractor)
1040	B	6	X	2	57	59	38.47		W	MMT	Bedd.
1040	B	6	X	2	59	63	38.49		W	MMT	Bedd. (same plane as below, measured with MMT)
1040	B	6	X	2	59	63	38.49		W	Protr.	Bedd. (same plane as above, measured with protractor)
1040	B	9	X	4	60	60	69.62		W	MMT	Bedd.

This is a sample of the table that appears on the volume CD-ROM.

nately this includes the décollement zone. Structural data from the underthrust domains are more reliable, although they too suffer from the hole deviation uncertainty.

Domain I: Sedimentary Wedge

This domain includes the interval from 0 to 371.2 mbsf, and corresponds exactly to lithostratigraphic Unit P1. The wedge domain is characterized by heterogenous bedding dips (Fig. 9), extensive intervals of apparently natural fracture networks, and zones of brittle-plastic stratal disruption that are most likely entirely caused by drilling disturbance. The extensive fracture networks and variable dips suggest pervasive brittle deformation.

No unequivocal evidence for discrete fault zones or strongly localized shearing was observed above the décollement within this domain. However, evidence for two structural discontinuities was observed. Small-scale deformation bands and stratal disruption in Cores 170-1040B-21X and 22X suggest a possible fault at ~180–190 mbsf. Because these are XCB cores, they were not subject to the spiral disturbance. Second, the sharp change in dip suggests another possible fault between 275 and 290 mbsf (Fig. 9).

In the APC- and XCB-cored Hole 1040B, the silty clays exhibit steep dips of as much as 40°–70° in XCB biscuits, even at only 38 mbsf. Zones of fissility appear in the section below the depth of about 94 mbsf (Core 170-1040B-12X) and persist to the bottom of the wedge domain without clear relation to other structures or to lithology. Bedding measurements are rare, because the sediment is typically massive, but where identified, bedding is inclined 35°–70°. No clear overall trends in dips or fracture orientations were observed in this domain, except in and just above the décollement zone.

Well-developed joints and networks of open fractures begin near the top of the section and are common throughout Domain I; most of the cored material is broken into angular fragments of claystone of varying sizes but typically of rhombic shape. The genesis of open fractures is always problematic in rotary-cut cores where even polished surfaces (slickensides) and slickenlines can be drilling-induced artificial features. The variations in intensity and concentration of fracturing, the strong preferred orientation, and the association with faults inferred from other evidence all lead us to believe that the wedge sediments in Domain I are highly fractured in situ. Therefore, we noted zones of concentrated fracture networks, believing them to demonstrate brittle shear strain of the wedge sediments, but did not attempt detailed interpretation of their structural significance.

Hole 1040C was washed down to 159 mbsf, and RCB coring commenced. Even though the cored interval overlapped with Hole 1040B XCB cores by more than 30 m, different structures were observed in the RCB cores than in the base of Hole 1040B. From Core 170-1040C-1R through 15R, zones of pervasive deformation bands on a

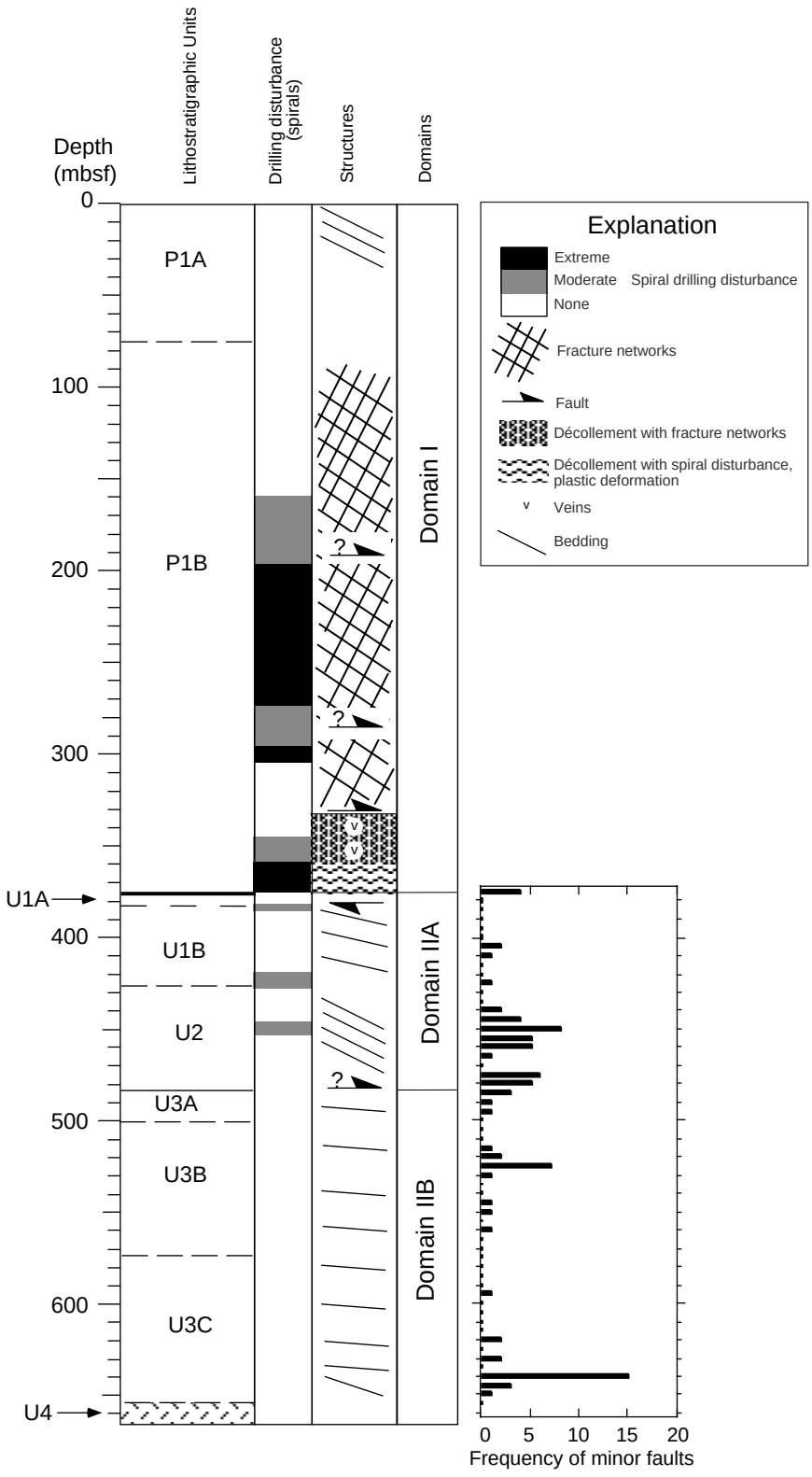

Figure 7. Structural summary diagram. Histogram indicates the frequency of minor faults observed in the core face per 5 m of core length in structural Domain II.

millimeter-spacing scale, plastic folding (Fig. 8), fissility, stratal disruption, and incipient scaly fabrics were documented. Because of evidence that these cores experienced extreme spiral drill disturbance (see "Biostratigraphy and Magnetostratigraphy" section, this chapter), we believe, or at least highly suspect, that these structures are primarily drilling induced. The entire interval from Cores 170-1040C-1R through 16R (159–305 mbsf) exhibits the paleomagnetic signature of this drilling disturbance (Fig. 7; see also "Biostratigraphy and Magnetostratigraphy" section, this chapter) and includes the depth range over which deformation band zones alternate with fracture networks above the décollement. This alternation of brittle vs. macroscopically plastic response to shear appears to be controlled by subtle variations in clay vs. silt content of the cores, revealed by slightly lighter and darker colors. Given the tectonic setting, signifi-

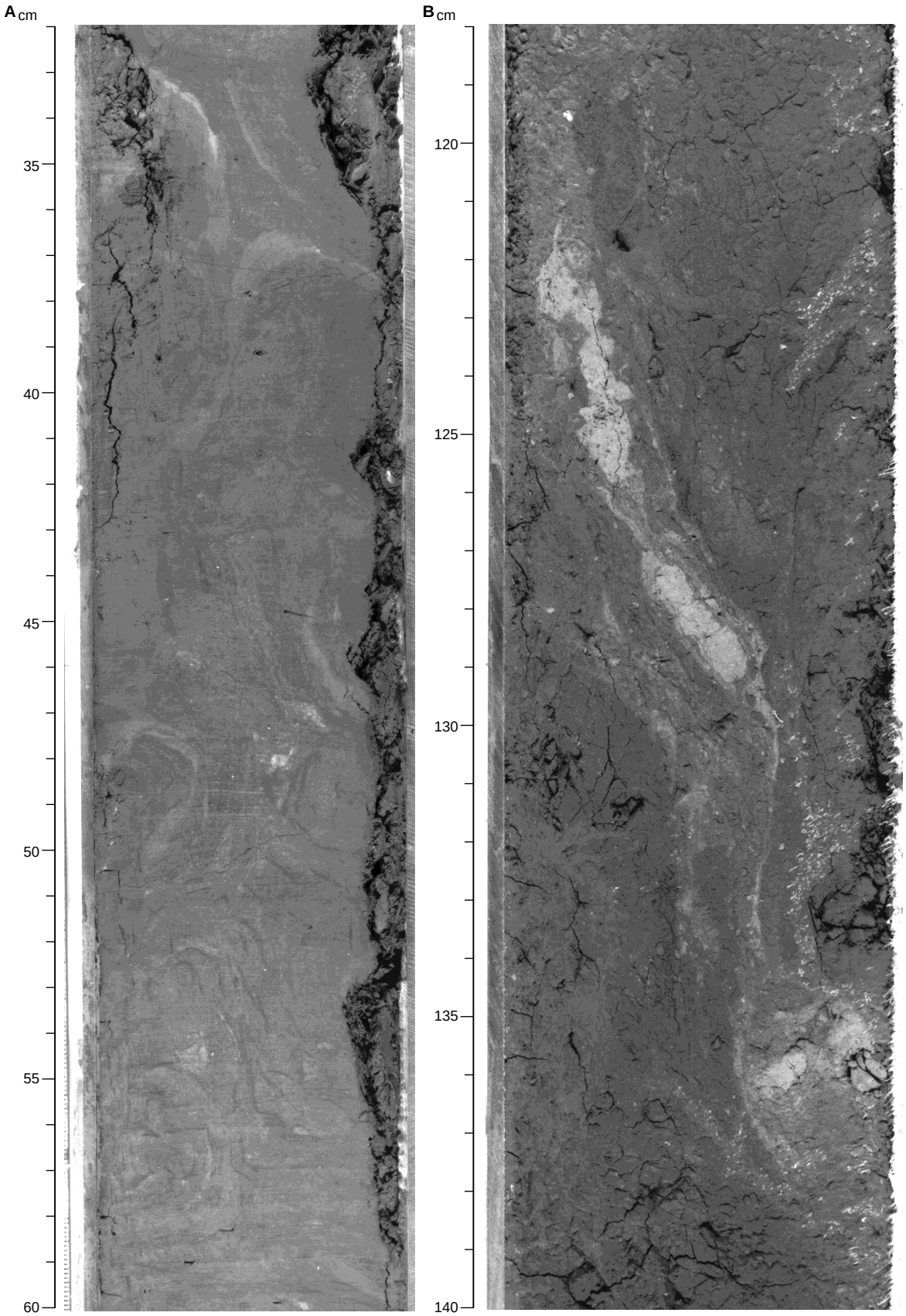

Figure 8. Examples of “spiral” core disturbance, mimicking natural structures. **A.** Apparent biscuited plastic folding of cored sediment (e.g., 47–50 cm, convex-right recumbent fold), with pervasive submillimeter deformation bands down central axis of core. This is within a zone shown by paleomagnetic remanence directions to be twisted in a continuous spiral by extreme drill disturbance (interval 170-1040C-1R-5, 32–60 cm). **B.** Torsionally sheared and extended calcareous mud clast, in fractured clayey matrix, also in zone of intense drilling disturbance (interval 170-1040C-10R-2, 118–140 cm).

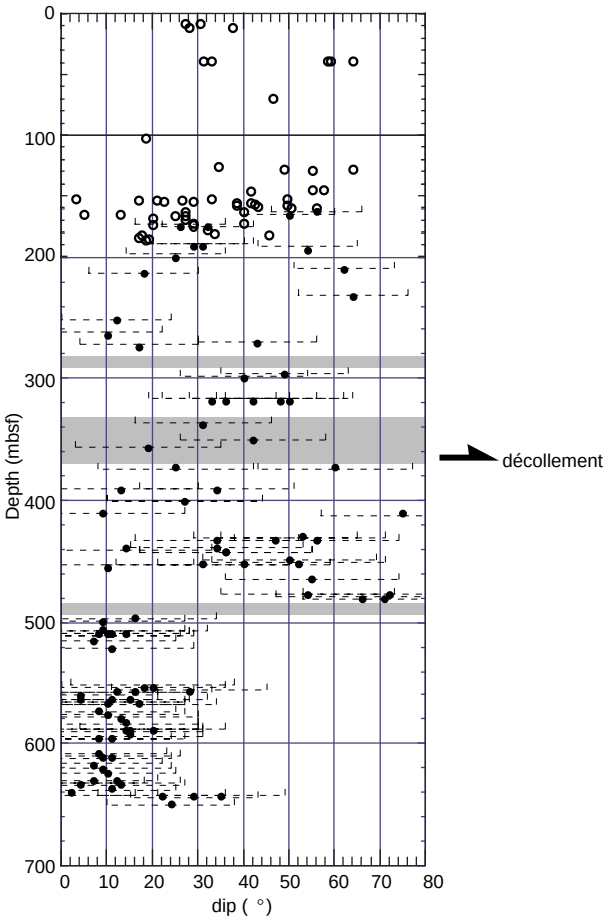

Figure 9. True bedding dip vs. depth. Open symbols are from Hole 1040B; solid symbols are from Hole 1040C. Error bars indicate uncertainty in measurements with respect to true vertical because of 19° hole inclination in Hole 1040C.

cant natural deformation of this interval is likely, but the extent is unknown because of the extreme drilling disturbance.

Based on the paleomagnetic evidence, the spiral disturbance ceases in the middle of Core 170-1040C-16R, and a much more intact zone persists from 305 to 345 mbsf, including the upper part of the décollement zone (see "Biostratigraphy and Magnetostratigraphy" section, this chapter). In this interval, the plastic folding and deformation bands are not evident, supporting the interpretation that those above were drilling induced. Cores 170-1040C-16R through 18R exhibit intervals up to tens of centimeters long of mostly intact silty claystone bounded by zones of closely spaced fracture networks and incipient scaly fabric (Fig. 10). The proportion and length of intact core pieces increases downward through Core 170-1040C-18R.

Macroscopically, the décollement zone is the detachment fault that separates the sedimentary wedge domain from the underthrust section and the latter is carried beneath the toe of the wedge with the downgoing plate. It is recognized in the cores as a shear zone of finite thickness at the base of the wedge. The bottom of the décollement zone is sharply defined by a change in both lithology and deformational style. The top of the décollement zone is less well defined, perhaps because of the drilling disturbance in the wedge cores and/or a more gradational structural signature. With the beginning of Core 170-1040C-19R, fracture networks abruptly become finely spaced and intense (Fig. 11). Only very short core sections are intact in Cores 170-1040C-19R through 22R. We place the top of the décollement zone at this apparent sudden increase in brittle fracture deformation at 332.6 mbsf, although the exact location is uncertain because of me-

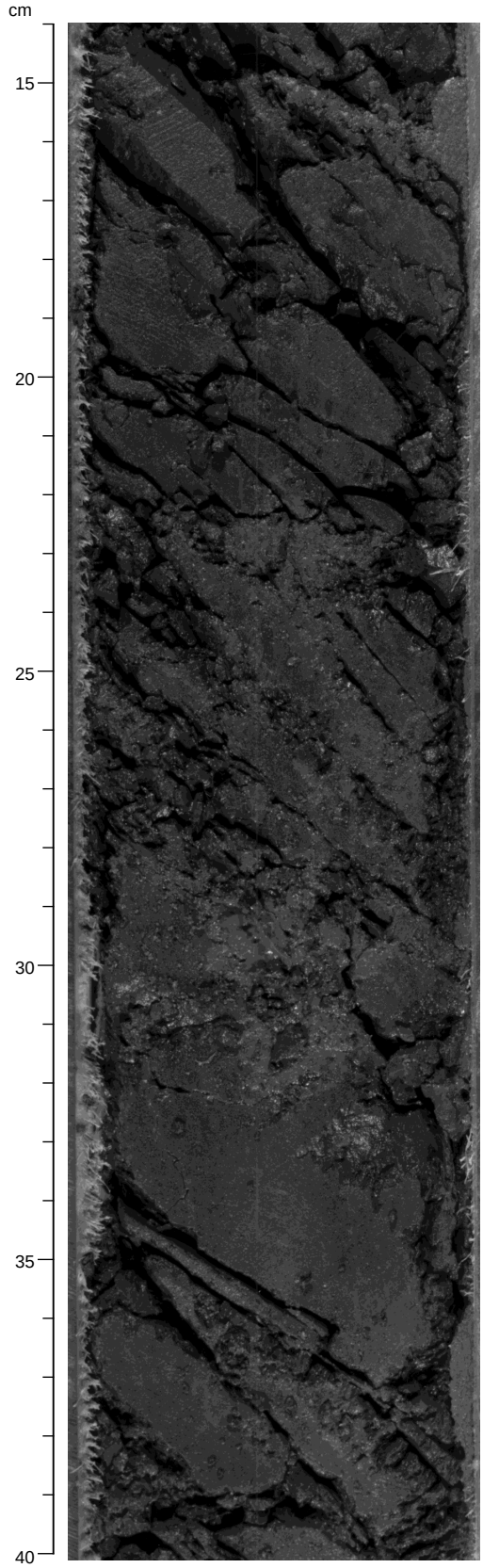

Figure 10. Silty claystone ~20 m above décollement zone, showing strong preferred orientation of fissility and fractures, as well as intact intervals (interval 170-1040C-17R-3, 14–40 cm).

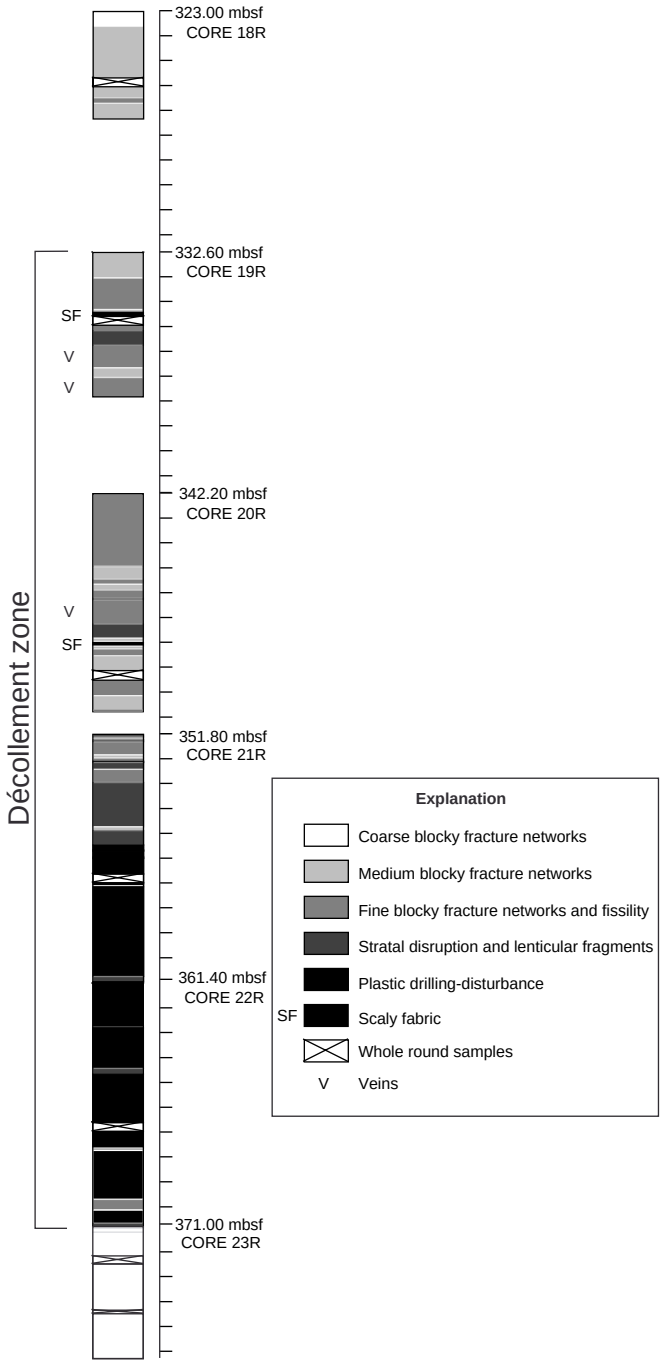

Figure 11. Detailed structural log of the décollement zone, Hole 1040C.

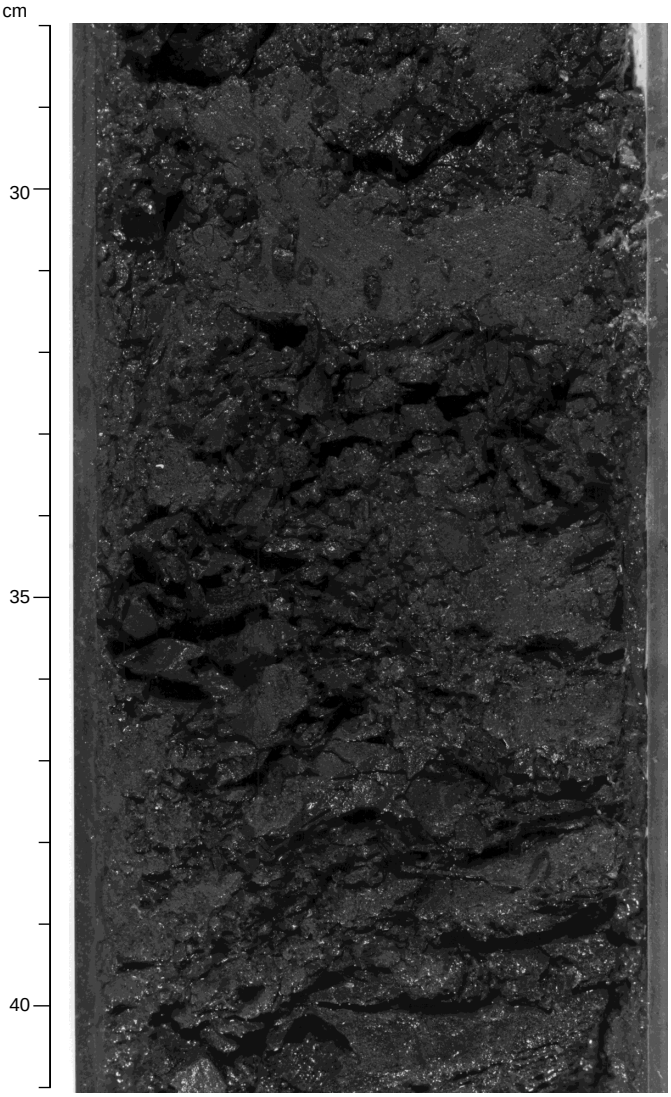

Figure 12. Silty claystone within the décollement zone, illustrating typical intense finely spaced fracture networks and lenticular polished and striated fragments that define the upper subdomain (interval 170-1040C-19R-4, 28–41 cm).

diocre core recovery. We distinguish two subdomains within the décollement zone. From interval 170-1040C-19R-1, 0 cm (332.6 mbsf), to 21R-4, 50 cm (356.8 mbsf), the cores are broken into lenticular to blocky fragments of millimeter to centimeter scale by fracture networks, strongly aligned in places (Fig. 12). Fragment surfaces are typically polished and striated. Several millimeter-scale veinlets of manganese oxide and rhodochrosite or siderite occur in Cores 170-1040C-19R and 20R, apparently as fracture fill (although these intervals are badly disaggregated). This upper subdomain is dominated by brittle fracture deformation at a fine scale. Bedding dip shows a trend toward shallower dips in the interval from 300 to 357 mbsf.

In the lower subdomain, from 356.8 to 371.2 mbsf, the sediment rheology abruptly changes to a stiff, but plastically deformed, silty clay. Fractures are mostly absent, but the extreme drilling disturbance is present throughout this zone, along with the plastic folding and incipient scaly fabric associated with this form of disturbance, as seen higher in Domain I. The drillers reported a sharp decrease in ROP through this interval, also suggesting a change in formation rheology. We cannot determine from the cores what the in situ state of deformation was before the drilling disturbance. We attribute all of the evident plastic deformation in this interval to drilling disturbance. Clearly, the subdomains within the décollement represent a change in rheology of the fault zone sediments, but the partitioning of strain between them remains unknown. However, considered on a large scale, the abrupt change in structural style and lithology between Cores 170-1040C-22R and the top of 23R sharply defines the detachment surface between the sedimentary wedge and the underthrust section.

Domain IIA: Upper Underthrust Section (371.2–483 mbsf)

With the top of Core 170-1040C-23R, the structural style changes abruptly, coinciding with a change in lithology to a diatom-rich sediment similar to that of Unit U1 at Site 1039. Primary sedimentary

structures and bioturbation are well preserved in this domain. From 371 to ~420 mbsf, bedding is gently to moderately inclined, 9°–35°, in part because of the deviation of the hole from vertical. Sediment-filled vein arrays are common in Cores 170-1040C-27R and 28R. Minor faults, typically exhibiting millimeter to several centimeter apparent offset in the core face, become more common and are especially abundant in Core 170-1040C-23R, just below the base of the wedge section. Such faults are rare through most of this domain, down to the lowermost 30–40 m of Domain IIA. At about 423 mbsf, bedding dip sharply increases from relatively shallow to steep (Fig. 9). Dips average 40°–45° in the interval 423–483 mbsf. This zone of steep dips is accompanied by a sharp increase in minor faults (Figs. 7, 13). Normal, reverse, and indeterminate (strike-slip or oblique?) offsets were observed, with reverse offsets dominating to the base of the steeply dipping zone at 483 mbsf. Below this depth, in Core 170-1040C-34R, dip sharply decreases, the minor faults become dominantly normal, and the number of minor faults decreases. We interpret this dip discontinuity as the location of a probable fault, although obvious fault fabrics were not recovered in the cores. We place this fault a few meters below the Unit U2/U3 boundary (Fig. 7), at the base of Core 170-1040C-34R (483 mbsf). Sense of fault slip or orientation is unknown, but the change from reverse minor faults to normal minor faults is consistent with compression in the hanging wall, suggesting reverse sense of shear.

Domain IIB: Lower Underthrust Section (483–661 mbsf)

The lowermost 180 m cored at this site have the most consistent dips and relatively few small-scale faults (Fig. 7). Dips cluster about an average of 10°–15° throughout this domain, except at the base of the domain in Cores 170-1040C-51R and 52R. Minor faults are much less common than above, are typically high angle, and always normal or strike-slip where sense can be determined (Fig. 14). The temporal sequence of sedimentary, diagenetic, and structural features is (1) bioturbation and formation of liesegang banding, (2) vertical axis flattening, and (3) fault displacement. Burrows throughout the underthrust domains have been flattened in the vertical or *Zoophycos*-perpendicular direction. This domain is thinner, less porous (see "Physical Properties" section, this chapter), more indurated, and has more numerous faults than the equivalent interval at Site 1039. The common small-scale normal faults are interpreted as a brittle accommodation of vertical axis shortening associated with compaction.

In Cores 170-1040C-51R and 52R, just above the contact with the gabbro intrusion, evidence of deformation increases again. As at Site 1039, dips steepen by about 20°; layer-parallel extension and boudinage, slump folds, and sedimentary breccia are present; and minor faults increase. Fluid escape structures or fluidized sediment injections (Fig. 15) appear to have formed contemporaneously with burrowing. We interpret these features taken together as indications of post-depositional tilting, perhaps during near-ridge normal faulting and/or emplacement of intrusions, producing oversteepened conditions that led to layer-parallel extension and local reworking by mass-wasting. Poorly developed, incipient stylolites are also evident in the lowest few meters above the gabbro. The stylolites indicate pressure solution perpendicular to a steep to subvertical compressional stress direction, consistent with emplacement of an intrusive body. We therefore ascribe these features near the bottom of Subunit U3C to very early near-ridge deformation and sedimentary reworking rather than to subduction zone processes.

The low and consistent dips of Domain IIB, taken with the known 15° deviation of the hole from vertical, allowed a shipboard estimate of the hole deviation azimuth to be made. If in situ dips are assumed to be subhorizontal in this domain, then the paleomagnetically reoriented dip azimuths give the azimuth of the hole deviation.

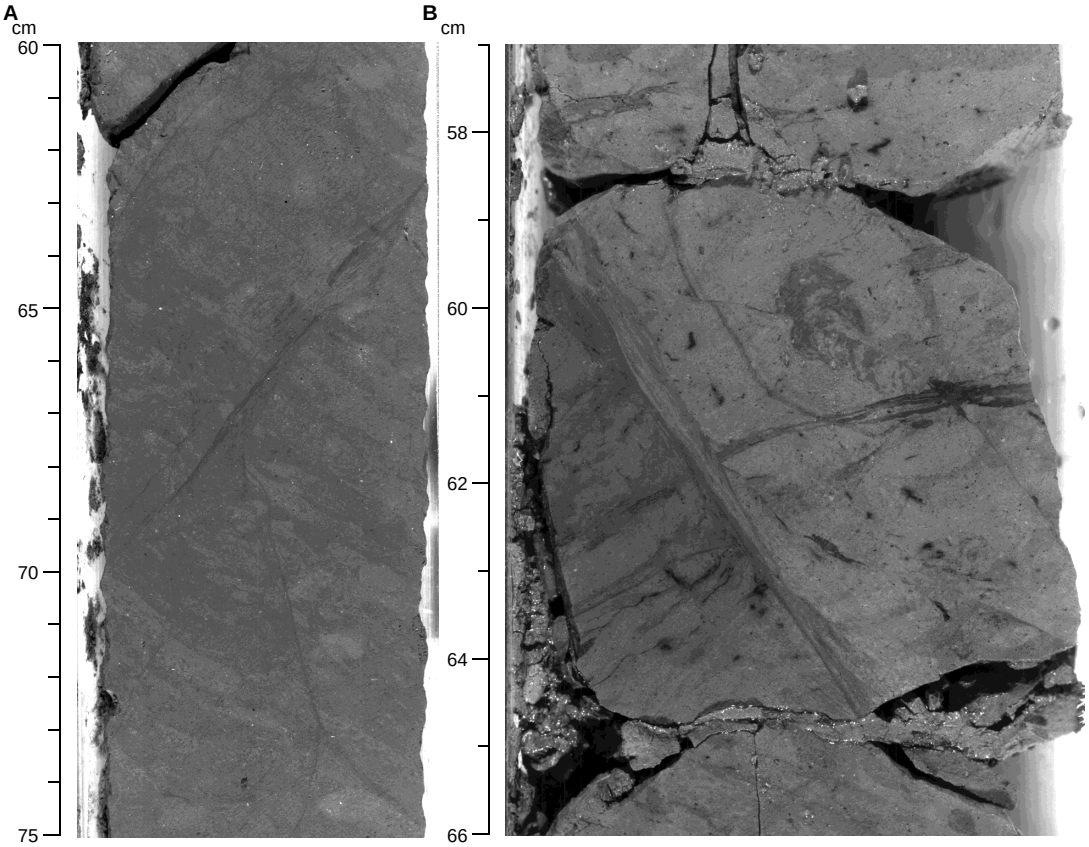

Figure 13. Examples of steeply dipping fault zones in Unit U2 silty claystone, beneath the décollement. Sense of slip not apparent in these examples. **A.** Interval 170-1040C-31R-1, 60–75 cm. **B.** Interval 170-1040C-31R-4, 57–66 cm. Note that the scale differs between parts A and B.

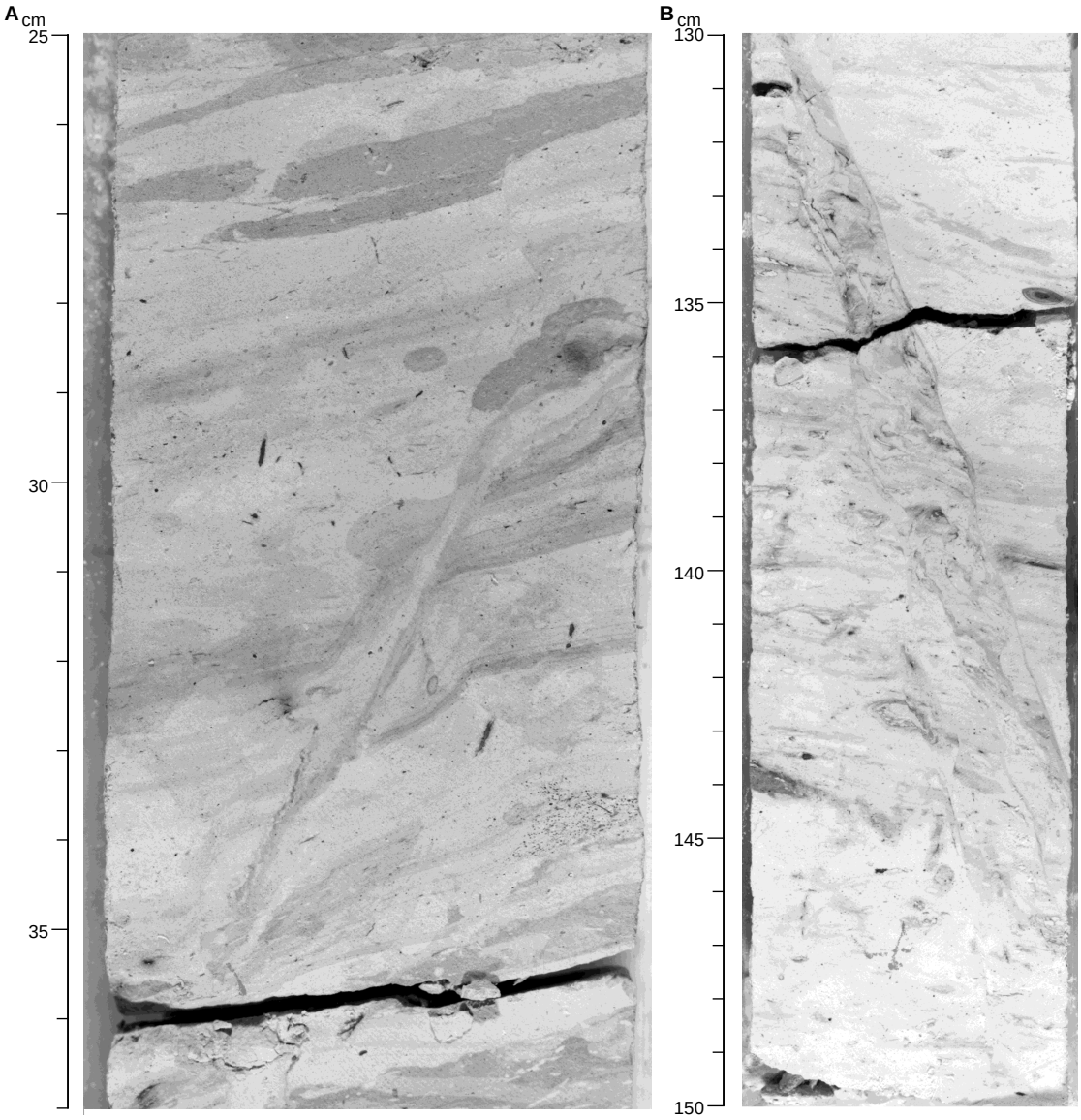

Figure 14. Typical minor faults in nannofossil chalks of structural Domain IIB. Offset dark features are liesegang bands and burrows, not depositional laminations. **A.** Interval 170-1040C-36R-1, 25–37 cm. Steeply dipping fault with normal sense of displacement. Apparent core face displacement of ~1 cm. **B.** Interval 170-1040C-46R-3, 130–150 cm. A fault zone, 1 cm wide, of apparent normal displacement, with evidence of plastic flow between bounding faults. Note that the scale differs between parts A and B.

We reoriented selected dip measurements into true coordinates using paleomagnetic declination and plotted the resulting cluster (Fig. 16). The data cluster is improved by the reorientation and averages 12° dip toward 270° azimuth. This result suggests that the assumption of horizontal bedding before drilling is reasonable and that the hole inclination azimuth at the bottom of the hole is 270°, the same direction shown by log results in the upper part of the hole. This suggests the deviation direction is consistent throughout the length of Hole 1040C. Unfortunately, this is the only interval in which structural data can be reoriented into geographic coordinates, so knowledge of the deviation direction is of limited use in orienting the structural data.

Discussion and Summary

The stratigraphic section cored at Site 1040 consists of 371 m of lithologically homogeneous sedimentary wedge section, made up of hemipelagic silty claystone, overlying 290 m of hemipelagic and pelagic sediment and gabbro of the underthrust section. The thickness of uncored intrusions and sediments from the bottom of Hole 1040C to oceanic basement is unknown. The underthrust section below the décollement zone is thinner and much more indurated than at Site 1039 seaward of the trench, but apparently includes a virtually identical stratigraphic succession. There is no sedimentologic evidence that any portion of the sedimentary wedge represents offscraped equivalents of any part of the Site 1039 lithostratigraphy.

Because of the tectonic partitioning of the sedimentary section at Site 1040, structural domains correspond well to the stratigraphic units. Domain I is the variably deformed sedimentary wedge that, based on lithology, has not accumulated by offscraping of oceanic plate sediments, but by accumulation and deformation of lower slope deposits (and possibly of trench axis deposits that do not extend to the reference site 1.5 km seaward of the wedge toe) brought to the wedge toe primarily by hemipelagic sedimentation and downslope mass transport processes. Deformational features of the wedge domain remain ambiguous because of the extensive drilling disturbance, poor

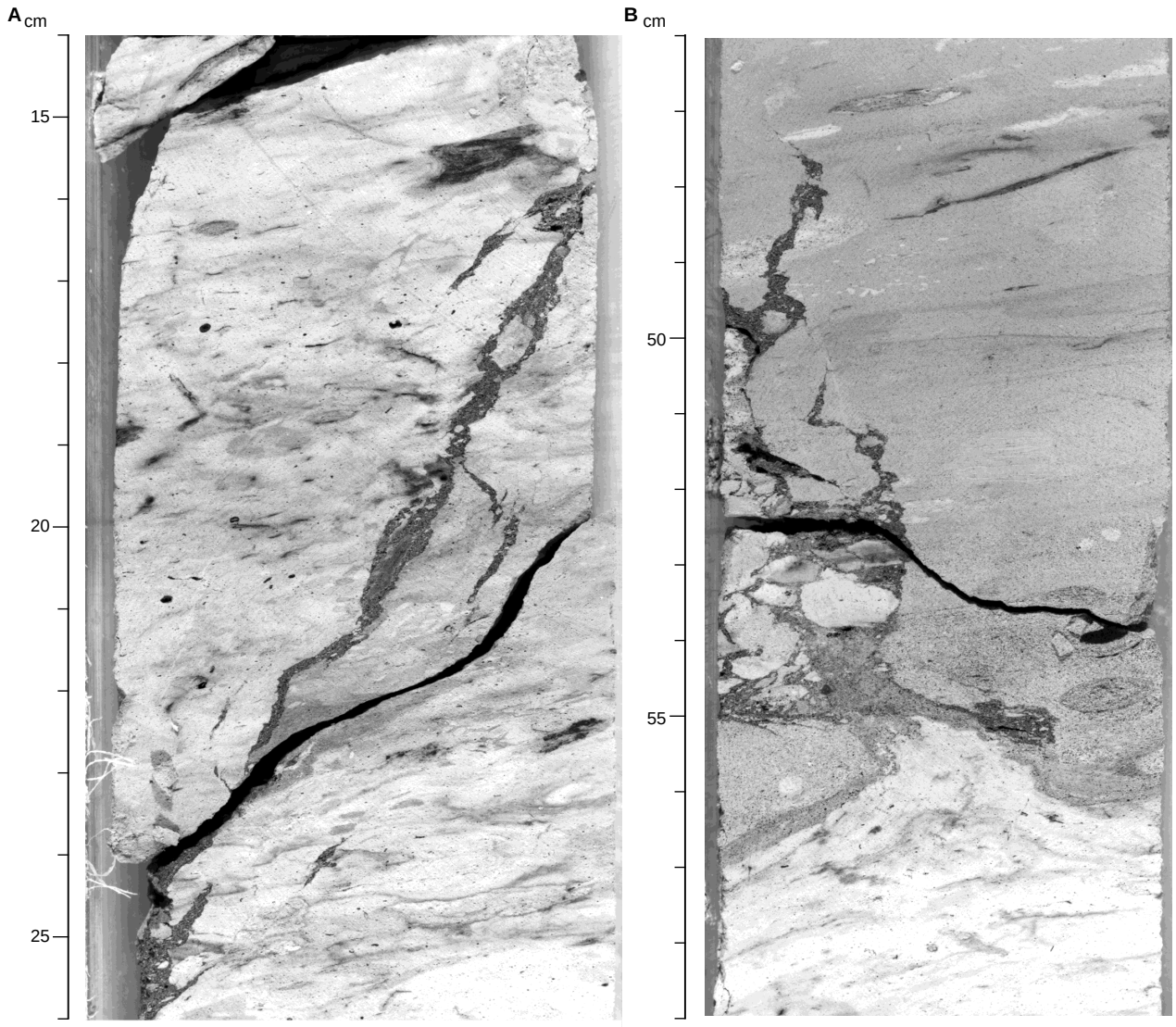

Figure 15. Examples of fluidized sediment injection structures in sedimentary Subunit U3C, 22 m above the gabbro intrusion. **A.** A 2- to 3-mm dark seam filled with sand- to pebble-sized fragments of ash and chalk (interval 170-1040C-50R-5, 14–26 cm). **B.** Small diapir of ash and chalk clasts that intruded overlying sediment contemporaneously with burrowing (e.g., diapir cuts burrow at 49 cm, but burrow cuts diapir at 47.3 cm; interval 170-1040C-50R-5, 46–59 cm). Note that the scale differs between parts A and B.

core recovery, and absence of preserved markers. The main structural hallmarks of the wedge are the well-developed brittle fracture networks that occur from tens of meters below the seafloor to the décollement zone. Zones lacking in fractures are typically less-lithified silty clay, and they exhibit the plastic deformation features we attribute to spiral disturbance, but which may have a natural deformational component.

The décollement zone is not marked by especially distinctive structural features compared to the rest of the wedge domain, although it has more intense fracture fabrics than the zones above and below, as well as some incipient scaly fabric. It consists of 25 m of brittlely deformed silty claystone overlying 14 m of plastically deformed and spiraled clay. The status of this zone as the primary detachment is recognized by the sharp contrast in lithology and deformation across its base at 371 mbsf. We cannot distinguish whether Unit P1 represents a structurally coherent sequence or repeated thrust sheets, given the lack of age control and extensive drilling disturbance throughout the 371-m thickness of the unit; however, no clearly repeated sections or markers were documented.

Beneath the décollement, the underthrust section is much more intact than the sedimentary wedge, but has not entirely escaped deformation. Significant dip and small-scale faults mark a tectonically deformed zone from 371 to 483 mbsf, probably fault bounded at the base. Beneath this inferred fault at 483 mbsf, the biogenic chalks of Unit U3 are essentially flat lying. Observed structures below 483 mbsf are consistent with vertical-axis compaction. The base of the sedimentary section just above the gabbro intrusion shows an increase in deformation that we interpret as having been caused by near-ridge deformation very early in the sediment history.

BIOSTRATIGRAPHY AND MAGNETOSTRATIGRAPHY

Biostratigraphy

Calcareous nannofossils, diatoms, and planktonic foraminifers are present in Holes 1040B and 1040C drilled at Site 1040, ~1.5 km from the toe of the sedimentary prism, near the base of the slope.

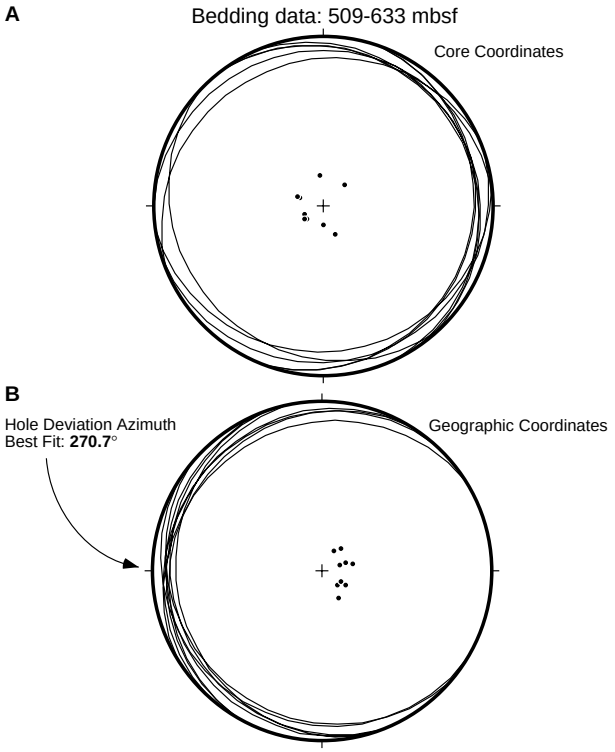

Figure 16. Stereoplot of bedding dips reoriented using paleomagnetic remanence directions in Domain IIB chalks. **A.** Core reference frame. **B.** True geographic coordinates. Dip azimuth direction indicates hole-deviation azimuth if beds were subhorizontal before drilling.

Only one core was recovered from Hole 1040A, and it was not biostratigraphically analyzed. With a few exceptions, descriptions of the microfossil assemblages from each core are from core-catcher samples only. A summary of the biostratigraphic zones observed at Site 1040 is given in Figure 17.

Calcareous Nannofossils

The occurrence, abundance, and preservation of the calcareous nannofossils recovered from Holes 1040B and 1040C are reported in range distribution charts (Tables 7, 8, respectively). In the Holes 1040B and 1040C descriptions below, the letters in parentheses after species names indicate that species' abundance as discussed in the "Explanatory Notes" chapter (this volume). These additional descriptions were derived from samples taken directly from the split core surfaces onboard ship between routine core-catcher samples and are not included in the range-distribution tables.

Hole 1040B

Diverse assemblages composed of varying amounts of Pleistocene, Pliocene, and middle and late Miocene calcareous nannofossils are present in Samples 170-1040B-1H-CC through 17X-CC. Although age-diagnostic marker species are present in some samples, it has not been possible to make any meaningful age determinations because some, if not all, of the nannofossils in this interval may be reworked. The degree of reworking, however, is not readily apparent.

Sample 170-1040B-1H-CC contains *Calcidiscus leptoporus*, small *Gephyrocapsa*, and small placoliths. Positive identification of these small placoliths will be made with the SEM to determine if they are *Emiliania huxleyi.* Also present in this sample are reworked Miocene and Pliocene species *Sphenolithus heteromorphus* and *S. abies.*

The added presence of reworked six-rayed discoasters distinguishes Sample 170-1040B-2H-CC from the overlying core-catcher sample. These discoasters are poorly preserved to the point where species identification is not possible.

Samples 170-1040B-3X-CC through 8X-CC contain a variety of poorly preserved, reworked assemblages that differ from each other by the presence of unidentifiable six-rayed discoasters and *S. neoabies/abies.* Common to all assemblages in this interval are small reticulofenestrids, *C. leptoporus*, and other badly dissolved placoliths. In most instances, species identification is not possible. The occurrence of large, poorly preserved discoasters in Sample 170-1040B-6X-CC is noteworthy.

Samples 170-1040B-9X-CC through 11X-CC contain few poorly preserved small reticulofenestrids only. Several samples taken within these cores between core-catcher samples exhibit the same paucity of species.

Sample 170-1040B-12X-CC consists of very badly dissolved and/or overgrown helicosphaerids, reticulofenestrids, and six-rayed discoasters that cannot be identified at the species level. However, there are a few *Gephyrocapsa caribbeanica* present that exhibit moderate preservation.

Calcareous nannofossil diversity is greater, and preservation is better in Sample 170-1040B-13X-CC than in the overlying samples. Moderately preserved *Discoaster berggreni, C. leptoporus, Gephyrocapsa oceanica, Helicosphaera carteri, Pontosphaera discopora, Coccolithus miopelagicus, Helicosphaera sellii, Calcidiscus macintyrei*, and poorly preserved six-rayed discoasters comprise the nannofossil assemblage.

Samples 170-1040B-14X-CC through 17X-CC contain very poorly preserved small reticulofenestrids, *H. carteri, P. discopora, C. miopelagicus, Discoaster surculus*, and diagenetically altered unidentifiable placoliths and six-rayed discoasters. In addition, *H. sellii* is also present in Sample 170-1040B-17X-CC. Compared to the overlying samples, there is a large increase in micrite in this four-core interval. We believe that these carbonate grains are remnant calcareous nannofossils that have been overgrown or recrystallized.

Samples 170-1040B-18X-CC through 21X-CC do not contain calcareous nannofossils. Several samples taken within the cores directly from the split-core surfaces in this interval are also barren of calcareous nannofossils.

Hole 1040C

As in Hole 1040B, the calcareous nannofossil assemblages found in Samples 170-1040C-1R-CC through 21R-CC may all be reworked. A mix of Pliocene through middle Miocene calcareous nannofossil species are found in all the core-catcher samples in this interval. In a few samples from this interval, Pleistocene calcareous nannofossil species are also observed. The extent of reworking, at this time, is not readily apparent. However, we have not ruled out the possibility of deciphering the biostratigraphic chronology for this interval.

The same stratigraphic section cored at the Site 1039 reference section is also seen in interval 170-1040C-22R through 51R. The base of the décollement likely lies somewhere within Core 22R. The lithology of this interval below the décollement is essentially the same as that at Site 1039, and the biostratigraphy of this interval is easily interpreted. A more detailed calcareous nannofossil biostratigraphy for Hole 1040C follows (Table 8).

Sample 170-1040C-1R-CC contains poorly preserved *H. carteri, P. discopora, H. sellii*, and small reticulofenestrids. Helicoliths dominate the assemblage. Discoasters and sphenoliths are absent.

The assemblage of calcareous nannofossils in Sample 170-1040C-2R-CC is very different from that seen one core above. Although they are poorly preserved, nannofossils present include *C. pelagicus, C. leptoporus*, six-rayed discoasters, and small reticulofenestrids. Helicoliths are absent.

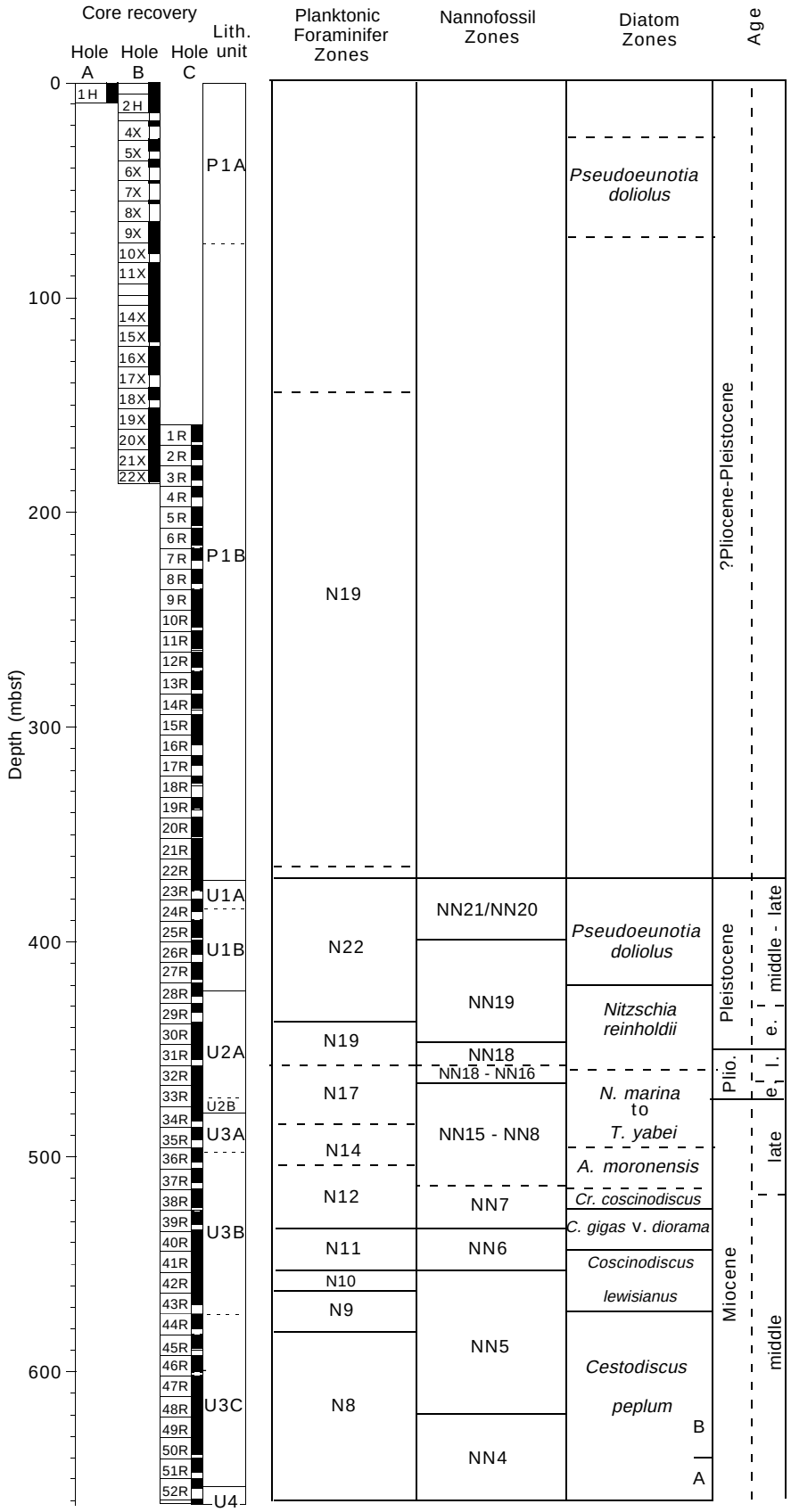

Figure 17. Correlation of the planktonic foraminifer, calcareous nannofossil, and diatom zones with Site 1040 cores and sedimentary units. Dashed lines represent uncertainty in placement of the zonal boundary.

Table 7. Calcareous nannofossil range distribution chart for Hole 1040B.

Calcareous nannofossil zone	Hole, core, section	Depth (mbsf)	Abundance	Preservation	*Discoaster surculus*	*Helicosphaera carteri*	*Coccolithus miopelagicus*	*Pontosphaera discopora*	*Calcidiscus leptoporus*	*Calcidiscus macintyrei*	*Discoaster berggrenii*	*Helicosphaera sellii*	*Sphenolithus abies/neoabies*	*Sphenolithus moriformis*	*Hayaster perplexus*	*Reticulofenestra pseudoumbilicus*	*Discoaster variabilis*	*Sphenolithus verensis*	*Emiliania huxleyi*	*Gephyrocapsa caribbeanica*	*Gephyrocapsa oceanica*	*Sphenolithus heteromorphus*	Six-rayed discoasters	Small reticulofenestrids	Unidentifiable helicosphaerids
NN21	1040B-1H-CC	5.49	A	M					C				r	F					C	A	C	r			
	1040B-2H-CC	14.02	C	M		F			F										F	C	F	r	C		
	1040B-3X-CC	14.25	R	P															R						
?	1040B-5X-CC	31.89	A	P														R						A	
	1040B-6X-CC	39.01	R	P									F				R								
	1040B-7X-CC	46.5	F	P									F		R	F							C	F	
	1040B-8X-CC	56.4	F	P					R				R	F											
	1040B-9X-CC	73.04	R	P																				R	
	1040B-10X-CC	79.63	R	P																				R	
	1040B-11X-CC	93.84	R	P																				R	
	1040B-12X-CC	98.48	F	P																			C	F	
	1040B-13X-CC	106.9	C	P		R	R	R	F	R	R	R											C	C	F
	1040B-14X-CC	112.33	R	P		R		R																F	
	1040B-15X-CC	120.86	R	P			R																	R	
	1040B-16X-8	132.43	R	P	R	R																			
	1040B-17X-CC	135.42	B																						
	1040B-18X-CC	147.17	B																						
	1040B-19X-CC	160.7	B																						
	1040B-20X-CC	171.11	B																						
	1040B-21X-CC	179.26	B																						

Notes: Abbreviations for abundances are as follows: A = abundant, C = common, F = few, R = rare, B = barren, and lowercase letters = reworked. Abbreviations for preservation are as follows: G = good, M = moderate, and P = poor. For abundance and preservation definitions refer to the "Explanatory Notes" chapter (this volume).

This table also appears on the volume CD-ROM.

Sample 170-1040C-3R-CC is comprised of assemblages characteristic of both Samples 170-1040C-1R-CC and 2R-CC, with the addition of the Pleistocene species *G. oceanica* and Pliocene–Miocene species *Sphenolithus moriformis* and *S. abies.*

Calcareous nannofossils are absent in Samples 170-1040C-4R-CC and 5R-CC, although the smear slides contain a large amount of micritic grains. These grains, seen upsection in this hole and in the similar horizon in Site 1039 cores, may be all that is left of an assemblage of nannofossils that has been severely altered.

Samples 170-1040C-6R-CC through 21R-CC, with the exception of barren Sample 170-1040C-15R-CC, contain considerably fewer carbonate grains and calcareous nannofossils than seen upsection in this hole. The calcareous nannofossil assemblages in this long (146 m) interval are characterized by small reticulofenestrids with lower abundances of six-rayed discoasters, *C. miopelagicus, H. carteri, Discoaster pentaradiatus, H. sellii,* and *C. leptoporus.* In addition, *Discoaster berggreni* (F) is present in Sample 170-1040C-18R-CC, and sphenoliths occur in Sample 170-1040C-21R-CC.

The assemblage of calcareous nannofossils observed in Sample 170-1040C-22R-CC is characteristic of the late Pleistocene Zones NN21/NN20, dominated by abundant *G. oceanica* and *G. caribbeanica.* This is the highest upsection sample in Hole 1040C that apparently contains a relatively pristine fossil assemblage. Shore-based SEM analysis is needed to ascertain the presence of *E. huxleyi.* Included in this assemblage are *P. discopora, H. carteri,* and coccospheres of *G. oceanica.* The calcareous nannofossil preservation is moderate.

Samples 170-1040C-23R-CC through 25R-CC contain the same assemblage of calcareous nannofossils as found upsection in Sample 170-1040C-22R-CC, except that the abundances are an order of magnitude less. In addition, *Ceratolithus telesmus* is present in Sample 170-1040C-25R-CC. The calcareous nannofossil assemblage places these three samples in Zone NN21/NN20.

The last occurrence (LO) of *Pseudoemiliania lacunosa* (0.46 Ma) is observed in Sample 170-1040C-26R-CC. Other nannofossils present are *H. carteri,* large *G. oceanica, C. leptoporus, G. caribbeanica,* and *P. discopora.* The occurrence of *P. lacunosa* and the absence of *Discoaster brouweri* indicates that this assemblage is characteristic of Pleistocene Zone NN19. Similar assemblages, all with moderately preserved calcareous nannofossils, are found in Samples 170-1040C-27R-CC through 30R-CC immediately downsection. In addition, Sample 170-1040C-30R-CC also contains the LO of *H. sellii* (1.47 Ma, equatorial Pacific).

The LO of *D. brouweri* (1.95 Ma) defines the top of late Pliocene Zone NN18 and is found in Sample 170-1040C-31R-3, 49 cm. Other species present in this sample include *H. carteri* (F), *P. lacunosa* (F), small reticulofenestrids (C), and *C. leptoporus* (C). The assemblage is poorly preserved. Samples 170-1040C-31R-4, 125 cm, and 31R-CC contain a similar assemblage. Samples taken between the core-catcher samples are not plotted in Table 8 between Cores 170-1040C-30R and 33R.

Sample 170-1040C-32R-CC does not contain nannofossils. However, additional sampling of the split-core surface (Sample 170-1040C-32R-3, 40 cm) indicates the common occurrence of broken specimens of *D. brouweri.* No other calcareous nannofossils are observed. Sample 170-1040C-32R-4, 50 cm, contains *P. discopora* (C), *Ceratolithus rugosus* (F), *P. lacunosa* (C–F), *D. brouweri* (C), *H. carteri* (C), *Ceratolithus armatus* (R), and *C. macintyrei* (R), all moderately preserved. These samples can only be placed within the range of Pliocene Zones NN18–NN16.

The LOs of *S. abies* and *S. neoabies* (3.60 Ma), as well as the LO of *Reticulofenestra pseudoumbilica* (3.75 Ma), are observed in Sample 170-1040C-32R-5, 66 cm, placing this sample in Zone NN15. Nannofossils occurring in this sample include *P. lacunosa* (F), *H. carteri* (F), *Discoaster challengeri* (R), and *D. brouweri* (F). All are poorly to moderately preserved.

The LO and first occurrence (FO) of *Discoaster quinqueramus* (5.6 and 8.6 Ma, respectively) defines the top and bottom of late Miocene Zone NN11. The LO of *D. quinqueramus* is found in Sample 170-1040C-33R-CC. The top of Zone NN11 lies just below the Mio-

Table 8. Calcareous nannofossil range distribution chart for Hole 1040C.

Calcareous nannofossil zone	Hole, core, section	Depth (mbsf)	Abundance	Preservation	*Calcidiscus leptoporus*	*Coccolithus miopelagicus*	*Cyclicargolithus floridanus*	*Discoaster deflandrei*	*Helicosphaera ampliaperta*	*Helicosphaera carteri*	*Sphenolithus heteromorphus*	*Sphenolithus moriformis*	*Sphenolithus verensis*	*Coronocyclus nitescens*	*Reticulofenestra pseudoumbilicus*	*Calcidiscus macintyrei*	*Pontosphaera discopora*	*Discoaster exilis*	*Discoaster variabilis*	*Discoaster kugleri*	*Discoaster berggrenii*	*Discoaster surculus*	*Helicosphaera sellii*	*Triquetrorhabdulus farnsworthii*	*Discoaster quinqueramus*	*Sphenolithus abies*	*Gephyrocapsa caribbeanica*	*Gephyrocapsa oceanica*	*Pseudoemiliania lacunosa*	*Ceratolithus telesmus*	*Coccolithus pelagicus*	*Gephyrocapsa sinuosa*	*Discoaster intercalaris*	*Gephyrocapsa aperta*	*Discoaster pentaradiatus*	*Helicosphaera scissura*	small reticulofenestrids
	1040C-1R-CC	166.94	F	M						F													R											R	F
	1040C-2R-CC	175.24	F	P	R																									R						F
	1040C-3R-CC	184.99	F	R	R	R						F											R			R									F
	1040C-4R-CC	192.85	B																																
	1040C-5R-CC	206.14	B																																
	1040C-6R-CC	215.14	F	P																							F								F
	1040C-7R-CC	222.36	R	P																												R		R	R
	1040C-8R-CC	233.21	R	P						R													R										R		
	1040C-9R-CC	246.05	R	P	R																												F		R
Undetermined	1040C-10R-CC	253.31	B																																
	1040C-11R-CC	264.35	C	P						R													R												C
	1040C-12R-CC	272.14	F	P						R																									F
	1040C-13R-CC	282.7	C	P	F					R																									C
	1040C-14R-CC	291.95	F	P	R					R																									F
	1040C-15R-CC	303.91	B																																
	1040C-16R-CC	306.84	F	P						A																									F
	1040C-17R-CC	317.58	F	P						R																									F
	1040C-18R-CC	327.11	R	P	R																R														
	1040C-19R-CC	338.33	R	P	R																R														
	1040C-20R-CC	350.78	F	P	R	R																											R		F
	1040C-21R-CC	361.64	F	P	R	R																				F							F		R
	1040C-22R-CC	371.21	C	P						F							R										C				R	C			
	1040C-23R-CC	376.2	F	P																								F							
NN21-NN20	1040C-24R-CC	385.6	F	P																								F							
	1040C-25R-CC	397.88	R	P						R																	R	R		R					
	1040C-26R-CC	405.74	F	P	R																						F	F	R						
NN19	1040C-27R-CC	417.37	F	P	R					R														R			F	C							
	1040C-28R-CC	425.3	F	P	F					F																									
	1040C-29R-3	432.57	F	M						F							R										F	F	R						F
	1040C-30R-CC	446.73	F	M						F							R							F											F
NN18	1040C-31R-CC	454.17	C	P	F																														C
	1040C-32R-CC	466.26	B																																
NN15	1040C-33R-CC	476.89	C	M	F										F				R			F			R	R									
NN11	1040C-34R-CC	483.46	C	M						R											C	F	R	R											
	1040C-35R-4	491.79	F	M		F									R						R														F
NN8	1040C-36R-CC	502.33	C	M		C						F							C																
	1040C-37R-CC	511.76	C	P	F	C						C								F															F
NN7	1040C-38R-6	523.13	C	M	F	C						C								F															F
	1040C-39R-5	531.31	C	M		C				F		F		F				F	R																
NN 6	1040C-40R-CC	544.31	F	M		F				F		F		F				F	R																
	1040C-41R-CC	553.94	A	M			F			F	C	C		F	C	F																			A
	1040C-42R-CC	563.46	C	M		C	F			F	C	C		F		F	F																		C
	1040C-43R-CC	568.57	A	M		C	F			F	C	C		F	C	F	F																		C
	1040C-44R-CC	579.31	A	M	F	C	F			F	C	C	C	F	C	F	F																		C
NN5	1040C-45R-CC	590.02	A	M	F	C	F			C	F	C	C	F	C	F	F																		C
	1040C-46R-CC	598.86	A	M	F	C	F				F	C	F	F	C	F	R																		C
	1040C-47R-CC	611.78	A	M	F	C	F			F	F	C	F	F	C	F	R																		C
	1040C-48R-CC	621.45	A	M	R	F	R			F	F	C	F	F	C	R	R																		C
	1040C-49R-6	629.99	A	M	F	F	R	F	F	F	F	C	F	F	A																				
NN4	1040C-50R-6	638.28	A	M	F	C	F	F	F	F	F	F		F	F																				C
	1040C-51R-CC	646.55	A	P	F	C	F	F	F	F	F	C	F																						C

Notes: Abbreviations for abundances are as follows: A = abundant, C = common, F = few, R = rare, B = barren, and lowercase letters = reworked. Abbreviations for preservation are as follows: G = good, M = moderate, and P = poor. For more specific definitions, refer to the "Explanatory Notes" chapter (this volume).

This table also appears on the volume CD-ROM.

cene/Pliocene boundary within Chron C3r. This indicates that the entire Pliocene sequence in Hole 1040C lies within Cores 170-1040C-32R and 33R. The obviously low age-depth rates within this interval make it highly unlikely that all of the Pliocene nannofossil zones would be observed in this shipboard reconnaissance study. Thus, it is not surprising that Pliocene calcareous nannofossil Zones NN17, NN16, NN14, NN13, and NN12 were not resolved at this site.

The nannofossil assemblage in Sample 170-1040C-33R-CC includes *R. pseudoumbilica, S. abies, C. leptoporus, D. quinqueramus, D. brouweri, D. surculus,* and three-rayed *Discoaster variabilis.* Assemblage preservation is moderate to poor.

The FO of *D. berggreni* and *D. quinqueramus* are nearly coeval. The FO of *D. berggreni* is observed in Sample 170-1040C-34R-CC, characterizing the nannofossil assemblages in Samples 170-1040C-34R-CC and 35R-CC as representative of Zone NN11. Calcareous nannofossils in Samples 170-1040C-34R-CC and 35R-CC include moderately to well-preserved *D. berggreni, D. surculus,* sphenoliths, *Triquetrorhabdus farnsworthi, Amaurolithus delicatus, H. sellii,* large *R. pseudoumbilica,* and *Coccolithus miopelagicus.*

The LO of *C. miopelagicus* (10.8 Ma) is observed in Sample 170-1040C-36R-CC. This sample does not contain five-rayed discoasters, *Discoaster bollii, Discoaster hamatus, Discoaster loeblichii, Catinaster coalitus,* or *D. surculus,* indicating that Zones NN10, NN9, and NN8 have not been resolved by the marker species in this interval. *D. variabilis* and *C. miopelagicus* are abundant and moderately preserved.

The LO and FO of *Discoaster kugleri,* delineating Zone NN7, (11.5–11.8 Ma) are recognized in Samples 170-1040C-37R-CC and

38R-CC, respectively. Species of nannofossils seen in these samples include *C. miopelagicus, Sphenolithus moriformis,* six-rayed discoasters, *D. kugleri, C. leptoporus,* and reticulofenestrids.

Samples 170-1040C-39R-CC and 40R-CC are assigned to Zone NN6 based on the absence of *D. kugleri* and *Sphenolithus heteromorphus* and the presence of *Cyclicargolithus floridanus.* Zone NN6 is bound on the top by the FO of *D. kugleri* (11.8 Ma) and on the bottom by the LO of *S. heteromorphus* (13.6 Ma). Species in this interval include *C. miopelagicus, S. moriformis, Discoaster exilis, D. variabilis, H. carteri,* and *Coronocyclus nitiscens.*

The LO of *S. heteromorphus* defines the top of Zone NN5 and is found in Sample 170-1040C-41R-CC. The base of Zone NN5 is defined as the LO of *Helicosphaera ampliaperta* (15.6 Ma). Samples 170-1040C-42R-CC through 48R-CC are assigned to Zone NN5 based on the presence of *S. heteromorphus* and absence of *H. ampliaperta.* Species typical of these samples are *S. heteromorphus, C. miopelagicus, S. moriformis, R. pseudoumbilica,* reticulofenestrids, *Coronocyclus nitiscens, H. carteri, C. macintyrei, P. discopora,* and *Cyclicargolithus floridanus.*

Zone NN4 is defined as the interval between the LO of *Sphenolithus belemnos* (18.3 Ma) at the base, to the LO of *H. ampliaperta* (15.6 Ma). The LO of *H. ampliaperta* is observed in Sample 170-1040C-49R-CC. *H. ampliaperta* is present in Samples 170-1040C-49R-CC through 51R-CC. The LO of *S. belemnos* is not encountered in this hole. Thus, this interval is assigned to Zone NN4 and cannot be older than 18.3 Ma. Species of nannofossils typical in this interval are *S. heteromorphus, S. moriformis, C. nitiscens, C. miopelagicus, H. carteri, Discoaster deflandrei, C. leptoporus,* small reticulofenestrids, *C. floridanus,* and unidentifiable six-rayed discoasters. Preservation decreases rapidly with depth in this interval. Sample 170-1040-52R-2, 150 cm, taken directly from the split-core surface, consists of an assemblage of carbonate grains, which are barely recognizable as calcareous nannofossils because of the intense degree of diagenesis.

Diatoms

Hole 1040B

Samples 170-1040B-1H-CC through 3X-CC are barren of diatoms, and Sample 170-1040B-4X-CC is the first sample from this hole to have common diatoms showing moderate preservation (Table 9). The assemblage has common *Thalassionema nitzschiodes* and few *Pseudoeunotia doliolus* and *Thalassiosira oestrupii,* with rare *Nitzschia marina.* This assemblage is characteristic of the *P. doliolus* Zone of the late Pleistocene and ranges in age from 0 to 0.62 Ma. Also observed in this sample are common reworked diatoms such as *Rhizosolenia praebergonii* var. *robusta,* a Pliocene species, and a few shallow-water benthic diatoms. Sample 170-1040B-5X-CC is barren of diatoms. Although diatoms are present in Sample 170-1040B-6X-CC, they are rare and include only poorly preserved long-ranging taxa. Samples 170-1040B-7X-CC and 8X-CC are barren of diatoms.

Sample 170-1040B-9X-CC has common diatoms showing moderate to poor preservation. The assemblage is similar to that observed in Sample 170-1040B-4X-CC with common *T. oestrupii,* few fragments of *N. marina,* and rare *P. doliolus* and *T. nitzschiodes* fragments, along with reworked Pliocene and Miocene taxa and some shallow-water diatoms. The absence of *Nitzschia reinholdii* suggests that the age of the sample is still within the *P. doliolus* Zone of the late Pleistocene with a maximum age of 0.62 Ma; however, the range of *P. doliolus* extends to 2.01 Ma, so it is possible that the sample could be latest Pliocene. Samples 170-1040B-10X-CC through 14X-CC are barren. Sample 170-1040B-15X-CC has rare diatoms that are poorly preserved benthic taxa, such as species of *Actinoptychus* and *Navicula.* Samples 170-1040B-16X-CC through 21X-CC are barren.

Hole 1040C

In Samples 170-1040C-1R-CC through 22R-CC, diatoms are absent in nearly all of the core-catcher samples except for rare amounts of poorly preserved frustules of *Actinoptychus senarius,* a long-ranging benthic diatom found in some samples. Below the décollement surface, beginning with Sample 170-1040C-23R-CC and continuing to Sample 170-1040C-50R-CC, diatoms are present on a more consistent basis and abundance and preservation shows similar variation to that observed at Site 1039, coinciding with the major lithologic unit boundaries (Table 9).

Diatoms in Samples 170-1040C-23R-CC through 27R-CC are part of lithologic Unit U1 (clayey diatomite) and are mostly common to abundant with moderate to good preservation. *P. doliolus, T. oestrupii, Azpeitia nodulifer, N. marina,* and *T. nitzschiodes* dominate the assemblage and are characteristic of the late Pleistocene *P. doliolus* Zone (0–0.62 Ma).

The LO of *N. reinholdii* occurs in Sample 170-1040C-28R-2, 125–150 cm, and marks the 0.62 Ma datum and the top of the Pleistocene to latest Pliocene *N. reinholdii* Zone. Diatoms are fewer in abundance beginning in Core 28R, marking the beginning of lithologic Unit U2 (silty claystone). Samples 170-1040C-28R-3, 42–43 cm, 28R-CC, and 29R-3, 96–100 cm, all have rare to few diatoms characteristic of the *N. reinholdii* Zone (*N. reinholdii, P. doliolus, T. oestrupii, A. nodulifer, N. marina,* and *T. nitzschiodes),* which ranges from 0.62 to 2.01 Ma. Samples 170-1040C-30R-CC through 32R-CC are barren of diatoms. Sample 170-1040C-33R-CC contains only rare amounts of taxa that are not diagnostic; therefore, the ages of these samples can only be inferred to be Pliocene from the age-depth plot (see Fig. 18).

Core 170-1040C-34R marks the beginning of lithologic Unit U3 (siliceous nannofossil chalk) and a greater abundance and preservation of diatoms. In Sample 170-1040C-34R-3, 125–150 cm, the presence of few specimens of *Thalassiosira praeconvexa* and *Nitzschia miocenica* suggest that the sample is between 6.17 and 6.69 Ma (the range of *T. praeconvexa*), or part of the latest Miocene *Thalassiosira convexa* Subzone A, or *N. miocenica* Subzone B. Consistent with our findings at Site 1039, the Unit U2–U3 lithologic transition coincides with a slower sedimentation rate; therefore 1.5 m.y. can be represented by the length of one core. Consequently, the presence of few *Rossiella paleacea* in Sample 170-1040C-35R-3, 132–152 cm, suggests that the sample is older than 7.37 Ma (the LO of *R. paleacea*). This is followed by the LO of *Actinocyclus moronensis,* occurring in Sample 170-1040C-35R-CC at an age of 9.66 Ma. Sample 170-1040C-36R-CC contains common diatoms that show good preservation and includes *A. moronensis* along with *Denticulopsis hustedtii, Thalassiosira yabei, Nitzschia porteri,* and *Coscinodiscus temperi* var. *delicata,* which are characteristic of the late Miocene *A. moronensis* Zone (9.66–11.34 Ma).

The LO of *Craspedodiscus coscinodiscus* occurs in Sample 170-1040C-37R-CC, marking the 11.34-Ma datum and the upper boundary of the late middle Miocene *C. coscinodiscus* Zone (11.34–12.06 Ma). Sample 170-1040C-38R-CC has *Cestodiscus pulchellus,* in addition to *D. hustedtii, T. yabei, Actinocyclus ellipticus* var. *javanicus,* and *Coscinodiscus gigas* var. *diorama,* which are characteristic of the *C. gigas* var. *diorama* Zone (12.06–12.86 Ma). Sample 170-1040C-39R-CC contains *Crucidenticula nicobarica,* whose LO is 12.4 Ma, along with taxa characteristic of the *C. gigas* var. *diorama* Zone. The top of the middle Miocene *Coscinodiscus lewisianus* Zone (12.86 Ma) is marked in Sample 170-1040C-40R-CC by the LO of *C. lewisianus.* The sample also includes common *C. nicobarica, Thalassiothrix longissima,* few *C. pulchellus, Actinocyclus ingens,* and *D. hustedtii.* Although *C. lewisianus* is present in Samples 170-1040C-35R-CC through 39R-CC, it is present as rare and poorly preserved specimens and is probably reworked in these samples. Another datum within the *C. lewisianus* Zone is the LO of *Thalassiosira tappanae,* which is observed in Sample 170-1040C-41R-CC at an age of 13.2 Ma. Sample 170–1040C-42R-CC contains abundant diatoms showing good preservation with taxa characteristic of the *C. lewisianus* Zone: *C. lewisianus, C. nicobarica, C. pulchellus,* and *A. ingens.* In addition, the acicular tests of the diatom *T. longissima* dominate the assemblage and, as observed in Unit U3 at Site 1039, this particular

Table 9. Diatom range distribution chart for Holes 1040B and 1040C.

Diatom zone	Core, section, interval (cm)	Depth (mbsf)	Abundance	Preservation	*Actinocyclus ellipticus*	*Actinocyclus ellipticus* var. *javanica*	*Actinocyclus ingens*	*Actinocyclus moronensis*	*Actinoptychus senarius*	*Annellus californicus*	*Asteromphalus elegans*	*Azpeitia nodulifer*	*Cavitatus jouseanus*	*Cestodiscus peplum*	*Cestodiscus pulchellus*	*Coscinodiscus lewisianus*	*Coscinodiscus lewisianus* var. *similis*	*Coscinodiscus marginatus*	*Coscinodiscus temperei* var. *delicata*	*Craspedodiscus coscinodiscus*	*Cruciculenicula nicobarica*	*Denticulopsis hustedtii*	*Hemidiscus cuneiformis*	*Nitzschia fossilis*	*Nitzschia marina*	*Nitzschia miocenica*	*Nitzschia portei*	*Nitzschia reinholdii*	*Pseudoeunotia doliolus*	*Rhizosolenia praebergonii* var. *robusta*	*Rossiella paleacea*	*Thalassionema nitzschioides*	*Thalassiosira oestrupii*	*Thalassiosira praeconvexa*	*Thalassiosira tappanae*	*Thalassiosira yabei*	*Thalassiothrix longissima*	*Triceratium pileus*
	170-1040B-																																				
	1H-CC	5.49	B																																		
	2H-CC	14.02	B																																		
	3X-CC	14.25	B																																		
	4X-CC	19.44	C	M																			r	R			F	r		C	R					
	5X-CC	31.89	B																																		
P. doliolus	6X-CC	39.01	R	P					R			R																				R	R				
	7X-CC	46.5	B						R																												
	8X-CC	56.4	B																																		
	9X-CC	73.04	C	P								R												F				R	r		R	C				
	10X-CC	79.63	B																																		
	11X-CC	93.84	B																																		
	12X-CC	98.48	B																																		
	13X-CC	106.9	B																																		
	14X-CC	112.33	B																																		
	15X-CC	120.86	R	P					R																												
	16X-8	132.43	B																																		
	17X-CC	135.42	B																																		
	18X-CC	147.17	B																																		
	19X-CC	160.7	B																																		
	20X-CC	171.11	B																																		
	21X-CC	179.26	B																																		
	170-1040C-																																				
	19R-CC	338.33	B																																		
	20R-CC	350.78	B																																		
	21R-CC	361.64	B																																		
	22R-CC	371.21	B																																		
	23R-CC	376.2	F	M								R											R	r	F			R			F	F				
	24R-CC	385.6	C	M					R															r	F			F	r		F	F				R	r
P. doliolus	25R-CC	397.88	C	M					R			R		r									R	r	F			F	r		F	C					r
	26R-CC	405.74	C	M				r			R												R	r	F		r	F	r		F	F					
	27R-CC	417.37	A	M	r							R													R			F			F	A					
	28R-2, 125-150	420.37	F	P							R																F	r									
	28R-3, 42-43	420.8	F	P								R											R		R			R	r		R	F					
	28R-CC	425.3	R	P																											R	R					
N. reinholdii	29R-3	432.57	F	G					R														R	R	R			r		F	F				R		
	30R-CC	446.73	B																																		
	31R-CC	454.17	B																																		
	32R-CC	466.26	B																																		
	33R-CC	476.89	R	P														R							R												
	34R-3, 125-150	481.39	F	M																						R						R	R			R	
N. marina to	34R-CC	483.46	F	M																												R	R			R	
T. yabei	35R-3, 132-152	487.96	F	P														F					R							R		R			F	
	35R-4	491.79	C	P	r			R				R				r		F					F							R	R	F			F	
A. moronensis	36R-CC	502.33	C	G				R				F				r			F			F					F			F	F	F			F	r
Cr. coscinodiscus	37R-CC	511.76	C	M								F				r			C	F		F								R					F	C	
C. gigas v. *diorama*	38R-6	523.13	A	G		R						F			r	r						F								F	F				F	C	r
	39R-5	531.31	C	G			F									r	r				R	F								F					R	C	r
	40R-CC	544.31	A	M			F		R		R	C			F	C				F	C	F								F	F					C	
C. lewisianus	41R-CC	553.94	A	G			F	R				F				C					A									F	F				F	A	
	42R-CC	563.46	A	M			C					R			F	F				F	A	F									F				F	A	
	43R-CC	568.57	A	M			F							R	F	F				F	A	F														A	
	44R-CC	579.31	A	M			F					F		R	F	F					C														F	A	
	45R-CC	590.02	A	G			C		R					R	C	F		F			A									F	F					A	
C. peplum sz B	46R-CC	598.86	A	G										R	C					F	A									F						A	
	47R-CC	611.78	A	G			C	R				F		R	F	R		C		F	C									F	F					A	
	48R-CC	621.45	A	M			F						F	R	C	R		F			F	R								R	F					A	
	49R-6	629.99	A	M									F	F	F	F		F			C									R						A	
C. peplum sz A	50R-6	638.28	A	M						R			F					F			C	F								F						A	
	51R-CC	646.55	B																																		

Notes: Abbreviations for abundances are as follows: A = abundant, C = common, F = few, R = rare, B = barren, and lowercase letters = reworked. Abbreviations for preservation are as follows: G = good, M = moderate, and P = poor. For more specific definitions, refer to the "Explanatory Notes" chapter (this volume). Sz = subzone.

This table also appears on the volume CD-ROM.

taxon is often concentrated in laminated intervals in siliceous nannofossil ooze.

The contact of the *C. lewisianus* Zone and the *Cestodiscus peplum* Zone is 14.03 Ma and is marked in Sample 170-1040C-43R-CC by the LO of *C. peplum.* In Samples 170-1040C-44R-CC through 49R-CC, diatoms are abundant and moderately preserved and consist of *C. peplum, Craspedodiscus coscinodiscus, C. nicobarica, C. pulchellus,* and *T. longissima,* typical of *C. peplum* Subzone B. Sample 170-1040C-50R-CC contains the LO of *Annellus californicus* at an age of 15.0 Ma, which marks the early middle Miocene Subzone A/B boundary of the *C. peplum* Zone. Samples 170-1040C-51R-CC and 52R-2, 32–34 cm, are barren of diatoms.

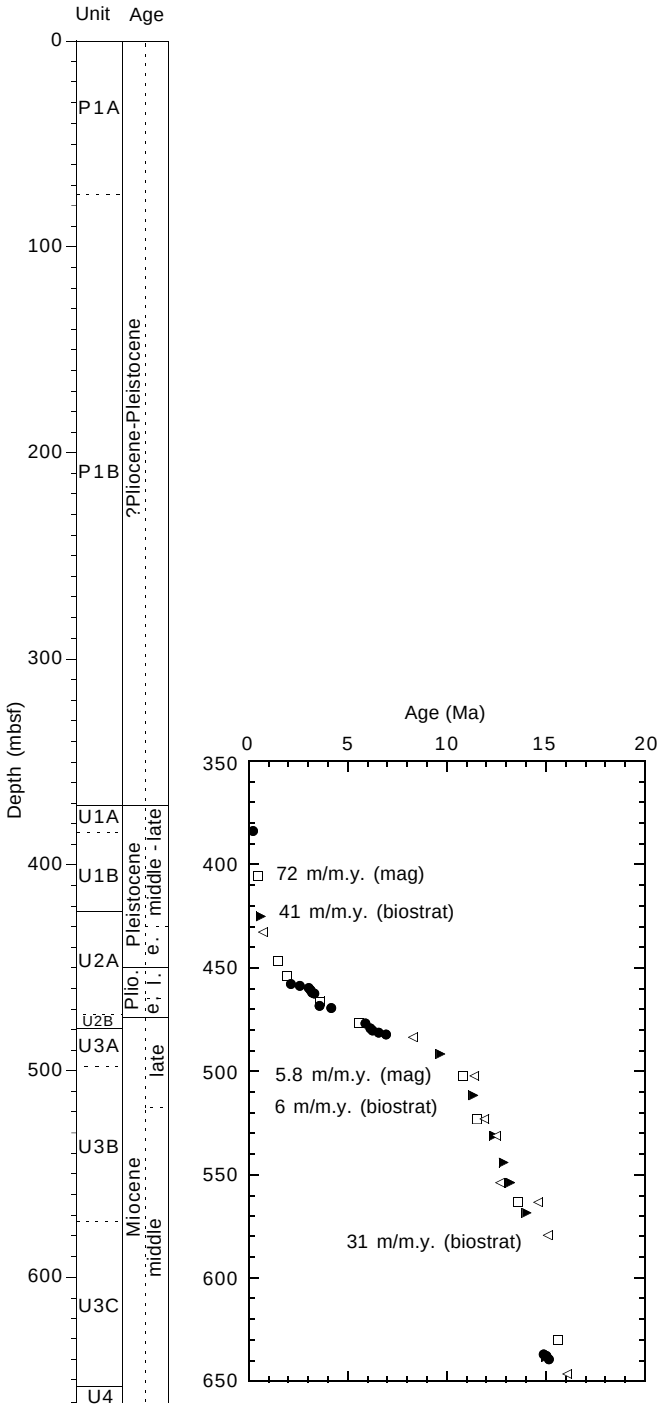

Figure 18. Age-depth relationship of key biostratigraphic datums from Hole 1040C. Calcareous nannofossils are represented by open boxes, diatoms by solid triangles, and planktonic foraminifers by open triangles. Linear age-depth rates are approximated for each major biostratigraphic segment (biostrat) of the age-depth curve. Paleomagnetic datums are plotted as solid circles for comparison with the biostratigraphic datums. Paleomagnetic linear age-depth rates (mag) are also approximated for each major paleomagnetic interval.

Planktonic Foraminifers

Planktonic foraminifers are rare and poorly preserved to barren in all core-catcher samples of Hole 1040B and in the upper part of Hole 1040C, from Samples 170-1040C-1R-CC through 25R-CC. The lower part of Hole 1040C, from Samples 170-1040C-26R-CC through 52R-2, 32–34 cm, ranges in age from the Pleistocene to the earliest part of the middle Miocene. In the Pleistocene to the late Miocene interval from Samples 170-1040C-26R-CC through 35R-CC, planktonic foraminifers are rare to absent and moderately preserved. The middle Miocene interval from Samples 170-1040C-36R-CC through 52R-2, 32–34 cm, yields common to abundant planktonic foraminifers that are moderately well preserved.

It was not possible to establish the planktonic foraminiferal zones in Hole 1040B and the upper part of Hole 1040C because of the absence of zonal marker species and reworking of older species. However, in the lower part of the sequence, middle Miocene assemblages are dominant, and some zonal marker species are present, so it may be possible to establish zonal intervals.

Hole 1040B

Planktonic foraminifers from Hole 1040B are rare to absent, and their preservation is moderate to poor (Table 10). Samples 170-1040B-1H-CC through 3X-CC, 7X-CC through 8X-CC, 12X-CC, and 14X-CC through 15X-CC include a mix of Pleistocene to Miocene marker planktonic foraminiferal species. Samples 170-1040B-4X-CC through 6X-CC, 13X-CC, 17X-CC, and 22X-CC are barren. In Sample 170-1040B-9X-CC, planktonic foraminifers are rare, including *Globigerinoides extremus, Globigerinoides ruber, Pulleniatina obliquiloculata,* and *Orbulina universa.* The sample is older than 1.77 Ma, based on the presence of *G. extremus.* The assemblages in Sample 170-1040B-20X-CC consists of *G. extremus, Globigerinoides trilobus, Neogloboquadrina humerosa, Pulleniatina primalis,* and *Sphaeroidinella dehiscens.* The sample ranges in age from 3.95 to 5.2 Ma, based on presence of sinistrally coiled *P. primalis* and *S. dehiscens.*

Hole 1040C

Planktonic foraminifers are rare to absent and, when present, are moderate to poorly preserved in the upper part of Hole 1040C, Samples 170-1040C-1R-CC through 24R-CC (Table 10). Below the décollement, planktonic foraminifers range in age from the Pleistocene to the earliest part of the middle Miocene. The Pleistocene to late Miocene interval from Samples 170-1040C-26R-CC through 35R-CC yield rare to few planktonic foraminifers that are moderately preserved. The middle Miocene interval from Samples 170-1040C-36R-CC through 52R-2, 32–34 cm, yield common to abundant planktonic foraminifers that are moderately well preserved.

In the upper part of Hole 1040C, from Samples 170-1040C-1R-CC through 24R-CC, planktonic foraminiferal assemblages consist of solution-resistant species that are rare and poorly preserved. Planktonic foraminiferal assemblages from Sample 170-1040C-1R-CC contain *G. extremus, Globigerinoides obliquus, G. trilobus, Globorotalia crassaformis, Globorotalia tumida, Globoquadrina venezuelana, Neogloboquadrina acostaensis, N. humerosa,* and *Dentoglobigerina altispira.* The age of the sample is 1.77–4.5 Ma based on presence of *G. extremus* and *G. crassaformis.* Planktonic foraminiferal assemblages in the interval from Samples 170-1040C-2R-CC through 21R-CC yield *Globigerina decoraperta, Globigerinoides immaturus, G. obliquus, G. trilobus, Globorotalia menardii, Globorotalia scitula, D. altispira, N. acostaensis,* and *P. primalis.* The age of the interval is 3.65–3.95 Ma, based on occurrence of dextrally coiled *P. primalis.* Sample 170-1040C-22R-CC contains the assemblages *G. menardii, G. scitula, G. crassaformis, G. inflata,* and *P. primalis.* The age of the sample is 3.95–4.5 Ma, based on co-occurrence of *P. primalis* (sinistral coiling) and *G. crassaformis.* Samples 170-1040C-23R-CC and 24R-CC lack age-diagnostic

Table 10. Planktonic foraminifer range distribution chart for Holes 1040B and 1040C.

Planktonic foraminifer zone	Hole, core, section	Depth (mbsf)	Abundance	Preservation	*Catapsydrax dissimilis*	*Catapsydrax stainforthi*	*Dentoglobigerina altispira*	*Dentoglobigerina globosa*	*Fohsella fohsi lobata*	*Fohsella fohsi sensu stricto*	*Fohsella peripheroacuta*	*Fohsella praefohsi*	*Globigerina falconensis*	*Globigerina nepenthes*	*Globiferina praebulloides*	*Globigerinatella insueta*	*Globigerinita glutinata*	*Globigerinoides altiapertura*	*Globigerinoides bulloideus*	*Globigerinoides conglobatus*	*Globigerinoides diminutus*	*Globigerinoides extremus*	*Globigerinoides immaturus*	*Globigerinoides kennetti*	*Globigerinoides obliquus*	*Globigerinoides quadrilobatus*	*Globigerinoides ruber*	*Globigerinoides sacculifer*	*Globigerinoides sicanus*	*Globigerinoides subquadratus*	*Globigerinoides tenellus*	*Globigerinoides trilobus*	*Globoconella conoidea*	*Globoconella conomiozea*	*Globoconella inflata*	*Globoquadrina baroemoenensis*	*Globoquadrina dehiscens*	*Globoquadrina venzuelana*	*Globorotalia bermudezi*	*Globorotalia birnageae*	*Globorotalia crassaformis*	*Globorotalia fohsi lobata*	*Globorotalia inflata*	*Globorotalia kugleri*	*Globorotalia margaritae*	*Globorotalia menardii*	*Globorotalia peripheroacuta*	*Globorotalia peripheroronda*	*Globorotalia plesiotumida*	*Globorotalia praemenardii*	*Globorotalia praescitula*	*Globorotalia scitula*	*Globorotalia siakensis*	*Globorotalia theyeri*	*Globorotalia tumida*	*Globorotaloides hexagona*	*Neogloboquadrina acostaensis*	*Neogloboquadrina dutertrei*	*Neogloboquadrina humerosa*	*Neogloboquadrina mayeri*	*Orbulina suturalis*	*Orbulina universa*	*Pulleniatina obliquiloculata*	*Pulleniatina primalis*	*Sphaeroidinellopsis kochi*	*Sphaeroidinellopsis seminulina*	*Tenuitella minutissima*	*Zeaglobigerina decoraperta*	*Zeaglobigerina druryi*
	170-1040B-																																																																					
N22	1H-CC	5.49	R	M	R	R																					R					R												R				R									R											
	2H-CC	14.02	R	M			R																				R					R					R	R						R		R		R					R				R											
	3X-CC	14.25	R	M																		R										R														R									R	R													
	4X-CC	19.44	B																																																																		
	5X-CC	31.89	B																																																																		
	6X-CC	39.01	B																																																																		
	7X-CC	46.5	R	P	T																				R																					R											R					R							
	8X-CC	56.4																																																																			
	9X-CC	73.04	R	M																		R					R																																			R	R						
N19	10X-CC	79.63	R	G																			R				R					R																														R		R					
	11X-CC	93.84	R	G																											T															T																							
N21	12X-CC	98.48	R	M									R												R							R														R							R				R	R											R	
N19	13X-CC	106.9	B																																																																		
	14X-CC	112.33	R	M																		R										R						R								R		R								R													
	15X-CC	120.86	R	M											R																									T																	R										T		
	17X-CC	135.42	B																																																																		
	18X-CC	147.17	T	M																																																	T																	
	19X-CC	160.7	R	M																		R			R							R														R							R			R		R		R					R					
	20X-CC	171.11	R	M																		R										R																											R					R	R				
	21X-CC	179.26	R	M																		R																								R											R											R	
	22X-4	186.19	B																																																																		
	170-1040C-																																																																				
N22	1R-CC	166.94	R	M																		R										R									R														R		R		R										
N19	2R-CC	175.24	R	P																								R				R														R							R					R							R					
	3R-CC	184.99	R	P			R															R																																											R		T			
	4R-CC	192.85	B																																																																		
	5R-CC	206.14	T	P																												T																																							
	6R-CC	215.14	R	P																																																					R									R		R	
	7R-CC	222.36	R	P																					R																					R							R					R							R					
	8R-CC	233.21	R	P			R																					R				R									R					R												R							R		R			
	9R-CC	246.05	R	P			R																																							R																			T				R	
	10R-CC	253.31	R	M																			R									R														R							R					R							R				R	
	11R-CC	264.35	R	P																		R																								R												R							T					
	12R-CC	272.14	R	M																					R			R																		R							R					R												
	13R-CC	282.7	R	P																		R					R					R																										R							R					
	14R-CC	291.95	R	P																					R																					R							R					R												
	15R-CC	303.91	R	P																		R			R	R						R														R							R					R												
	16R-CC	306.84	B																																																																		
	17R-CC	317.58	R	P			R															R																																											R				R	
	18R-CC	327.11	R	P			R															R		R	R		R					R														R												R							R					
	19R-CC	338.33	T	P																T																										T																								
	20R-CC	350.78	T	P																					T																																											T	
	21R-CC	361.64	B																																																																		
	22R-CC	371.21	R	M																	R										T				R						R					R							R			R								T	T					
N22	23R-CC	376.2	R	P																												R														R													R											
	24R-CC	385.6	F	P																		R											R													R										R		R	R					R						
	25R-CC	397.88	B																																																																		
	26R-CC	405.74	F	M																								R				R														R													R											
	27R-CC	417.37	F	M																							R	R				R							R																R				R					R						
	28R-CC	425.3	F	P																							R	R																		R										R			R					R						
	29R-3	432.57	F	M														R									R	F											R				R			R							R				R		R					F						
	30R-CC	446.73	R	M																			R		R		R	R																		R											R													

Table 10 (continued).

Planktonic foraminifer zone	Hole, core, section	Depth (mbsf)	Abundance	Preservation	*Catapsydrax dissimilis*	*Catapsydrax stainforthi*	*Dentoglobigerina altispira*	*Dentoglobigerina globosa*	*Fohsella fohsi lobata*	*Fohsella fohsi sensu stricto*	*Fohsella peripheroacuta*	*Fohsella praefohsi*	*Globigerina falconensis*	*Globigerina nepenthes*	*Globiferina praebulloides*	*Globigerinatella insueta*	*Globigerinita glutinata*	*Globigerinoides altiapertura*	*Globigerinoides bulloideus*	*Globigerinoides conglobatus*	*Globigerinoides diminutus*	*Globigerinoides extremus*	*Globigerinoides immaturus*	*Globigerinoides kennetti*	*Globigerinoides obliquus*	*Globigerinoides quadrilobatus*	*Globigerinoides ruber*	*Globigerinoides sacculifer*	*Globigerinoides sicanus*	*Globigerinoides subquadratus*	*Globigerinoides tenellus*	*Globigerinoides trilobus*	*Globoconella conoidea*	*Globoconella conomiozea*	*Globoconella inflata*	*Globoquadrina baroemoenensis*	*Globoquadrina dehiscens*	*Globoquadrina venzuelana*	*Globorotalia bermudezi*	*Globorotalia birnageae*	*Globorotalia crassaformis*	*Globorotalia fohsi lobata*	*Globorotalia inflata*	*Globorotalia kugleri*	*Globorotalia mararitae*	*Globorotalia menardii*	*Globorotalia peripheroacuta*	*Globorotalia peripheroronda*	*Globorotalia plesiotumida*	*Globorotalia praemenardii*	*Globorotalia praescitula*	*Globorotalia scitula*	*Globorotalia siakensis*	*Globorotalia theyeri*	*Globorotalia tumida*	*Globorotaloides hexagona*	*Neogloboquadrina acostaensis*	*Neogloboquadrina dutertrei*	*Neogloboquadrina humerosa*	*Neogloboquadrina mayeri*	*Orbulina suturalis*	*Orbulina universa*	*Pulleniatina obliquiloculata*	*Pulleniatina primalis*	*Sphaeroidinellopsis kochi*	*Sphaeroidinellopsis seminulina*	*Tenuitella minutissima*	*Zeaglobigerina decoraperta*	*Zeaglobigerina druryi*
N19	31R-CC	454.17	R	M																		R			R	R		R				R													R	R										R			R					R					
	32R-CC	466.26	B																																																																			
	33R-CC	476.89	B																																																																			
N17	34R-CC	483.46	R	M			R	R																	R													R								R			R																				R		R	
N14	36R-CC	502.33	C	M			R							R																							R	F								R														R						R			
N12	37R-CC	511.76	A	M			R														R									R		R		R		R	R	F				R											F							F		R				R			F
	38R-6	523.13	A	M			F		R	F																		R		R							R	F				R											R							F		R				R		R	R
	39R-5	531.31	A	M			F	R		R																											R												R	R										R				R	R			
N11	40R-CC	544.31	A	M			F	R		R	R	R											F		R							R					R	F									R			R	R		R							F						R			
	41R-CC	553.94	C	G						R	R	R																R				R						F									R						R							F	R					R			
N10	42R-CC	563.46	A	M			R																R					R							R	F	F									R	R												R					R			R
N9	43R-CC	568.57	A	M																			R						R								F		R									R					R							R	R					R		R	
	44R-CC	579.31	C	M			R	R										R							R			R		R						R		R										R			R		R							R	R							R	R
N8	45R-CC	590.02	C	M			R																		R			R									R	R		R								R			R		R							R								R	
	46R-CC	598.86	F	M			R																R		R													R										R					R							R									R
	47R-CC	611.78	F	M																			R															R		R								R					R							R									
	48R-CC	621.45	C	M			R									R		R					R		R					R						R	R	R										R																					R
	49R-6	629.99	A	M												R		R					R					R	R							R		R		R								R					R							R						R			
	50R-6	638.28	R	M														R											R	R							R																	R															
	51R-CC	646.55	A	M																	R								R									R										R												R									
	52R-3	653.32	C	P																					R			R							R	R	R																						R									

Notes: Abbreviations for abundances are as follows: A = abundant, C = common, F = few, R = rare, and B = barren. Abbreviations for preservation are as follows: G = good, M = moderate, and P = poor. For more specific definitions, refer to the "Explanatory Notes" chapter (this volume).

This table also appears on the volume CD-ROM.

planktonic foraminifers. Cores 170-1040C-4R-CC, 16R, 21R, and 25R are barren of planktonic foraminifers.

Planktonic foraminifers in Samples 170-1040C-26R-CC through 35R-CC range in age from the Pleistocene to late Miocene. The sequences yield rare to few planktonic foraminifers that are moderately preserved. Samples 170-1040C-32R-CC through 33R-CC are barren of planktonic foraminifers. Planktonic foraminifers are Pleistocene in age in Samples 170-1040C-26R-CC through 29R-CC, yielding *G. ruber, G. trilobus, Globigerinoides sacculifer, G. menardii, Globorotalia bermudezi, G. tumida, Neogloboquadrina dutertrei,* and *P. obliquiloculata.* In Sample 170-1040C-28R-CC, the coiling change in *Pulleniatina* spp. indicates an age of 0.74 Ma.

Planktonic foraminifers from Pliocene sequences in Sample 170-1040C-31R-CC yield *G. ruber, Globigerinoides quadrilobatus, G. extremus, N. humerosa,* and *P. primalis.* The sample was assigned to Zone N19, based on the occurrence of *Globorotalia margaritae* and sinistrally coiled *P. primalis.* Samples 170-1040C-32R-CC through 33R-CC are barren of planktonic foraminifers. Planktonic foraminifers from the late Miocene are present in Sample 170-1040C-34R-CC and include *G. decoraperta, G. obliquus, D. altispira, G. venezuelana, G. menardii, Globorotalia plesiotumida,* and *Sphaeroidinellopsis seminulina.* The sample was assigned to Zone N17, based on occurrence of *G. plesiotumida* and absence of *G. tumida.* Coarse fraction residues of Sample 170-1040C-35R-CC are dominated by abundant radiolarians, and age marker planktonic foraminifers are absent.

Middle Miocene assemblages in Samples 170-1040C-36R-CC through 52R-2, 32–34 cm, are dominated by *D. altispira, G. immaturus, G. sacculifer, G. trilobus, Globorotalia foshi*-group, *Globorotalia peripheroronda, Globorotalia siakensis, Globoquadrina baroemoenensis, G. venezuelana, G. dehiscens, Neogloboquadrina mayeri,* and *S. seminulina.*

Sample 170-1040C-36R-CC was assigned to Zone N14 (late middle Miocene) on the basis of the co-occurrence of *N. mayeri* and *Globigerina nepenthes.* Zone N13 was not identified. The interval from Samples 170-1040C-37R-CC through 39R-CC was assigned to Zone N12 (late middle Miocene) on the basis of the co-occurrence of *Globorotalia foshi foshi* and *Globorotalia foshi lobata.* The interval from Samples 170-1040C-40R-CC through 41R-CC was assigned to Zone N11 (late middle Miocene) on the basis of the occurrence of *G. foshi foshi, Globorotalia praefoshi,* and *Globorotalia peripheroacuta.* Sample 170-1040C-42R-CC was assigned to Zone N10 (middle middle Miocene) on the basis of the co-occurrence of *G. peripheroacuta* and *G. peripheroronda.* The interval from Samples 170-1040C-43R-CC through 44R-CC was assigned to Zone N9 (early middle Miocene) on the basis of the FO of *Orbulina suturalis* in 44R-CC. The interval from Samples 170-1040C-45R-CC through 52R-2, 32–34 cm, was assigned to Zone N8 (early middle Miocene), based on presence of *Globigerinoides sicanus* and absence of *Orbulina* spp.

The lower part of Hole 1040C, Samples 170-1040C-26R-CC through 52R-2, 32–34 cm, correlates with Hole 1039B, Samples 170-1039B-8H-CC through 6R-CC. At both Site 1039 and Site 1040, late Miocene sequences were not recovered.

Paleomagnetism

Demagnetization of both split cores and discrete samples was used to characterize the remanence directions in Site 1040 sediments. As was the case at Site 1039, poor core quality and drilling disturbance had degraded portions of the magnetostratigraphy at this site. Additional uncertainty is added to magnetostratigraphy by the high (up to 18°) hole deviation (see "Operations" section, this chapter). When added to the moderate to steep bedding dips at portions of this site, the borehole deviation can prevent a unique determination of remanence polarity given the shallow inclinations expected at this location.

Spiral Core Disturbance

Cores drilled with the RCB system at Site 1040 were often highly disturbed. In contrast to the normal random array of magnetic remanence declinations expected for severely biscuited sediment, a characteristic counterclockwise progression of declination downcore with sharp breaks between some of the declination trends was observed (Fig. 19). The most likely interpretation is that the sediment has been sheared into a series of spirals either within the core liner or during the time the sediment is being cut by the drilling shoe. Comparison between sediment physical properties (see "Physical Properties" section, this chapter) from overlapping XCB cores in Hole 1040B and RCB cores with spiraled declinations from Hole 1040C also shows lower (3%–10%) porosities in the comparable RCB cores relative to the XCB cores.

To serve as a measure of core quality, the number of complete spirals, defined as continuous 360° rotations of declination per meter of recovered core, was counted for each core at Hole 1040C (Fig. 20). Peaks in rotations per meter occur within Cores 170-1040C-9R, 15R, 20R, and 21R. These peaks seem to occur within a sticky clay lithology (see "Lithostratigraphy" section, this chapter), and correlate with decreased ROP during drilling.

Magnetostratigraphy

Within the slope and wedge sediments (0–330 mbsf), numerous normal and reversed polarity intervals have been determined (Fig.

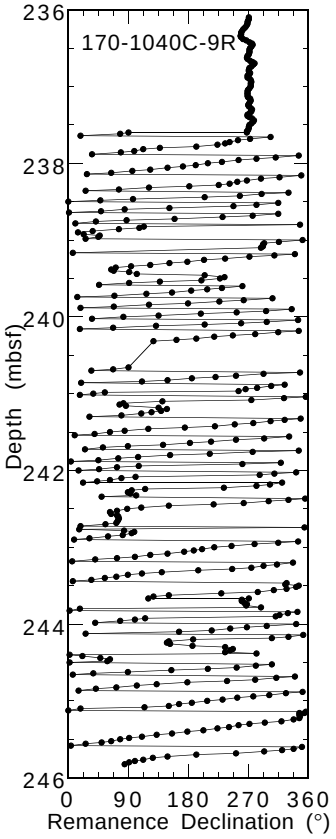

Figure 19. Remanence declination after 20-mT AF demagnetization from Core 170-1040C-9R. The declinations define a quasi-continuous series of counterclockwise spirals, resulting from penetrative shearing of this RCB core.

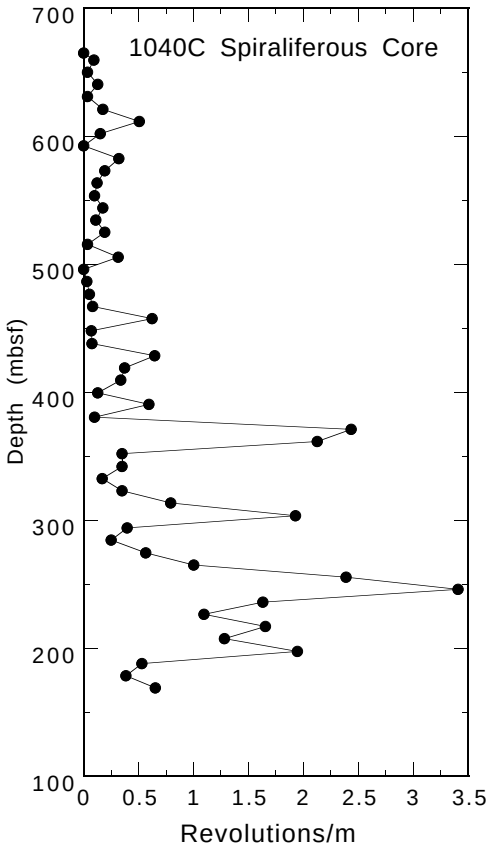

Figure 20. Number of 360° spirals of remanence declination per meter for all cores from Hole 1040C. Peaks in revolutions per meter occur within Cores 1040C-9R, 15R, 20R, and 21R, which have a sticky clay lithology.

21). Lack of good biostratigraphic age control and the high probability of multiple thrust faults within these sediments have prevented a unique assignment of our reversal stratigraphy to any specific portion of the magnetic polarity time scale. The reversed-polarity results at 5 mbsf at Site 1040B do suggest, however, that these near-surface sediments are at least 0.78 Ma in age.

Beneath the décollement (371–655 mbsf), a good magnetostratigraphic record has been obtained from the underthrust sediments (Fig. 22). In particular, the Jamaica Event (0.2 Ma) has been located at 383.7 mbsf, and a complete set of reversals ranging in age from 2.14 (C2r.1n) to 6.935 Ma (C3Bn) occurs between 458 and 482 mbsf in Hole 1040C.

Age-Depth Correlation

Unfortunately, although nannofossils and diatoms are generally present in the slope and accretionary prism of this section (0–330 mbsf), the assemblages appear to be reworked Pleistocene through early Miocene taxa, which generally exhibited poor preservation. Thus, an age-depth correlation within the slope and prism sediments based on nannofossil or diatom biostratigraphy has not been attempted. Limited age control within the prism was possible utilizing foraminifer datums. However, even these data are too sparse to yield an age-depth plot for the sequence.

The section below the décollement at Site 1040 (371–655 mbsf) appears to be identical to the section cored at reference Site 1039 with one exception. The section at Site 1040 is compressed by an average of ~33% compared to the reference site. The underthrust section at Site 1040 contains a nearly complete late Pleistocene through middle Miocene assemblage of calcareous nannofossils, diatoms, and planktonic foraminifers very similar to those seen at Site 1039. A linear age-depth model estimated from the combined index microfossil datums (Table 11; Fig. 18) indicates that age-depth rates of apparent sedimentation are ~41 m/m.y. for the Pleistocene (405.74–446.73 mbsf), 5.8 m/m.y. for the Pliocene and upper Miocene interval (446.73–502.33 mbsf), and 31 m/m.y. for the middle Miocene interval (502.33–646.55 mbsf). An age-depth model estimated from the magnetostratigraphy indicates rates of ~72 m/m.y. for the Pleistocene (383.7–457.8 mbsf), 5.8 m/m.y. for the Pliocene and upper Miocene interval (457.8–482.10 mbsf), and 2 m/m.y. for the middle Miocene interval (636.95–639.3 mbsf).

More detailed age-depth rate curves are shown in Figure 1. These curves are generated by fitting a smoothed curve to the biostratigraphic and paleomagnetic data (see “Explanatory Notes” chapter for a description of the procedure).

GEOCHEMISTRY

Overview of Results

The main objectives for determining key geochemical parameters of the volatile hydrocarbons, pore waters, and sediment and igneous rocks at Site 1040, located ~1.6 km arcward from the deformation front, are

1. To characterize the deformed wedge material and identify its sources;
2. To recognize in the deformed wedge material the hemipelagic section of the subducting sediments and estimate its contribution to frontal accretion;
3. To document the changes in the chemical and isotopic properties that underthrusting inflicts upon the pelagic and hemipelagic sediments and pore waters of the reference Site 1039, located just ~3 km westward;
4. To decipher their origin and source;
5. To determine the loss of water and solid mass in the underthrust section and utilize these data for geochemical and material mass balance calculations; and
6. To learn about the nature of the décollement zone and its hydrogeochemical significance.

The chemical compositions of the volatile hydrocarbons and pore waters are distinctly different in the deformed wedge and underthrust sections, having sharp transitions across the base of the décollement zone at ~371 mbsf. In the deformed wedge, methane (C_1), ethane (C_2), and propane (C_3) concentrations are significantly higher than in the underthrust section. The latter is characterized by mostly background volatile hydrocarbon concentrations (except for ~110 ppmv C_1 in hemipelagic Unit U1). On average, in the deformed wedge, the pore-fluid salinity and chlorinity are lower than that of seawater by 17% and 12%, respectively, with focused excursions of higher dilutions up to a maximum of 34% in salinity and 28% in chlorinity; one of the main excursions occurs at the décollement. The two main focused salinity and chlorinity minima also show ethane, propane, and Ca-concentration maxima. We infer that fluid has migrated along conduits and permeated the lower half of the deformed wedge from a deep source of several kilometers. Assuming that the geothermal gradient is somewhat higher at the source region than the very low gradient measured at this site (probably similar to that at Site 1041, ~2.5°C/100 m), then the source region must occur at >4 km depth because the minimum temperature required for thermogenic gas formation is 90°–100°C. Gas hydrate dissociation caused by drilling causes other lesser Cl dilution excursions in the pore-water concentration depth profiles. These excursions, however, are not accompanied by thermogenic gases or Ca maxima.

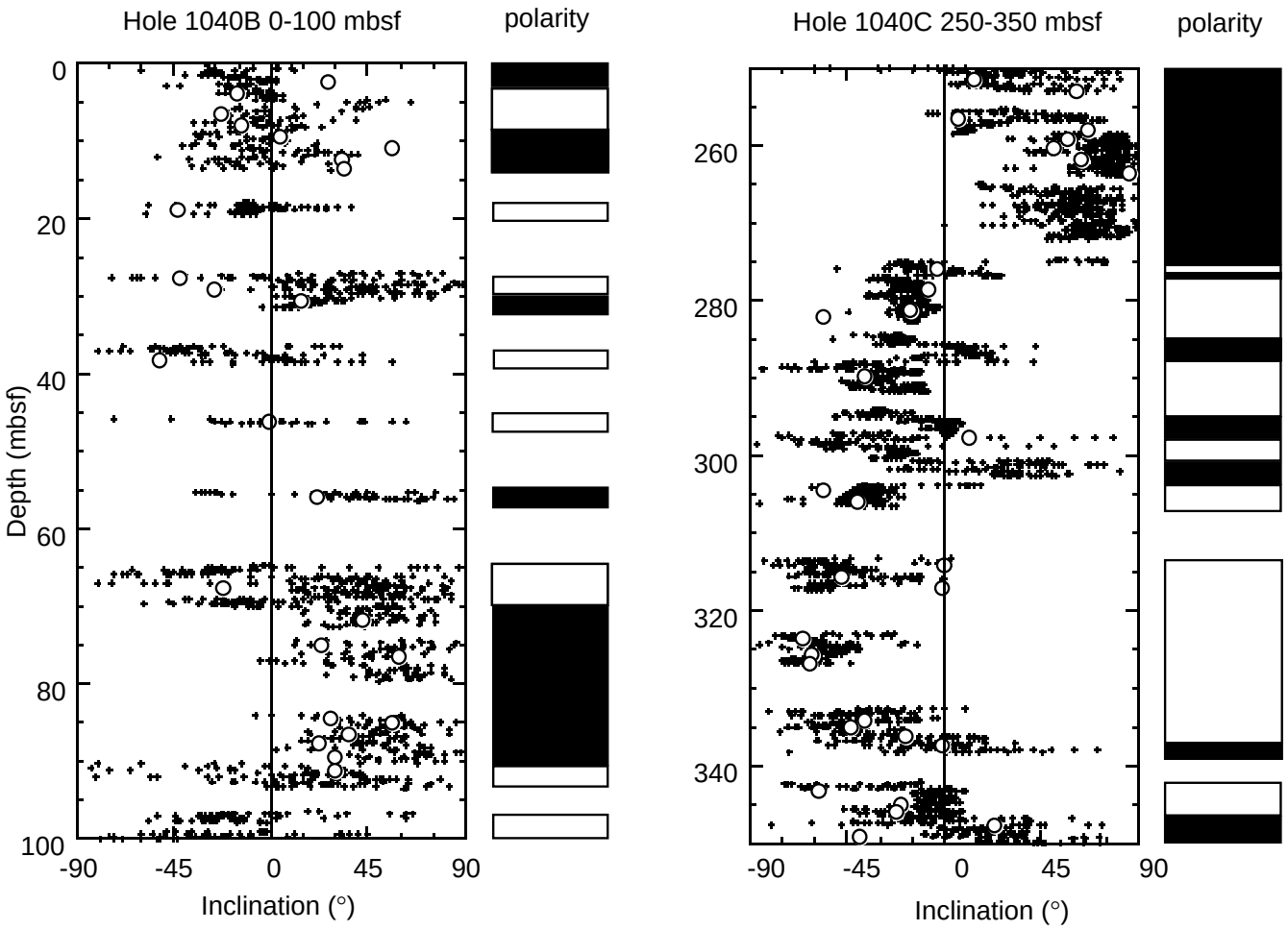

Figure 21. Examples of intervals showing reversal of polarity. Inclinations of remanence after 20-mT demagnetization of split cores from Hole 1040B, 0–100 mbsf, and Hole 1040C, 250–350 mbsf (crosses), and from discrete samples (circles). The interpreted magnetostratigraphy is shown on the right column.

Each pore-fluid component analyzed shows a major concentration discontinuity across the décollement. Furthermore, a second significant geochemical discontinuity occurs at ~180 mbsf, just above the most intense Cl minimum interval. The pore-fluid chemistry of the section below this boundary is typified by very high-Ca, low-Mg, and low-K concentrations, suggesting that this deformed wedge section has been permeated by a fluid that has been generated at greater depth. Several physical properties (see "Physical Properties" section, this chapter) clearly show discontinuities at this depth interval. The boundary at ~180 mbsf seems to be lithologically indistinct (see "Lithostratigraphy and Structures" section, this chapter), but is observed in the sediment geochemistry of mobile components (for example in Si, alkalies, and Fe_2O_3* concentrations at the depth interval 175–200 mbsf, but not below it). This geochemical response suggests that the main sediment source has maintained uniform chemical composition throughout the time interval represented by Subunit P1B (see "Lithostratigraphy and Structures" section, this chapter) and that the changes in pore-water chemistry result from fluid infiltration into the lower half of the deformed wedge section. The chemical changes observed in the boundary conduit at 180 mbsf are similar to those observed in the décollement conduit.

Except for the biogeochemical components, the pore-fluid concentration depth profiles of the underthrust section are similar to those at Site 1039. The concentrations themselves are lower or higher than at Site 1039, reflecting the changes in solubilities and dissolution rates of the major sediment components under the new pressure regime. These concentration differences also imply that little vertical advection has occurred, despite the considerable shortening of the sediment column, especially of the hemipelagic section. The fluid flow induced by tectonic compaction seems to be primarily lateral; the fluid must connect and migrate out through faults. In the underthrust hemipelagic section, despite similar TOC contents, the chemical gradients reflecting sulfate reduction, alkalinity, ammonium, and phosphate production are more intense than at Site 1039. This increased intensity is a result of the loss upon subduction of diffusional communication with bottom seawater, which sustained the bacterially mediated sulfate-reduction system at a steady-state rate for ~2.5 Ma at Site 1039 (see "Site 1039" chapter, this volume), as well as the continuous production and diffusion of alkalinity, ammonium, and phosphate. Sulfate reduction thus reaches completion in the uppermost few meters of the underthrust hemipelagic section, resulting in somewhat elevated methane concentrations at the zero-sulfate depth interval. The chemical profiles of the biogeochemical components, and also of Si and K, indicate that only 3–4 m (±1 m) of the uppermost hemipelagic sediments of Subunit U1A have been removed. Thus, on the basis of the pore-water chemistry, ~99% of the incoming sediments are being underthrusted. This is supported by the lithology and physical properties of the underthrust section (see "Lithostratigraphy and Structures" and "Physical Properties" sections, this chapter).

The XRF sediment geochemistry may be used for several purposes. A sharp increase in Ba, Cu, and Ni is observed between samples taken at 367 and 372 mbsf and identifies the underthrust section. The sediments of the deformed wedge are homogeneous in composition,

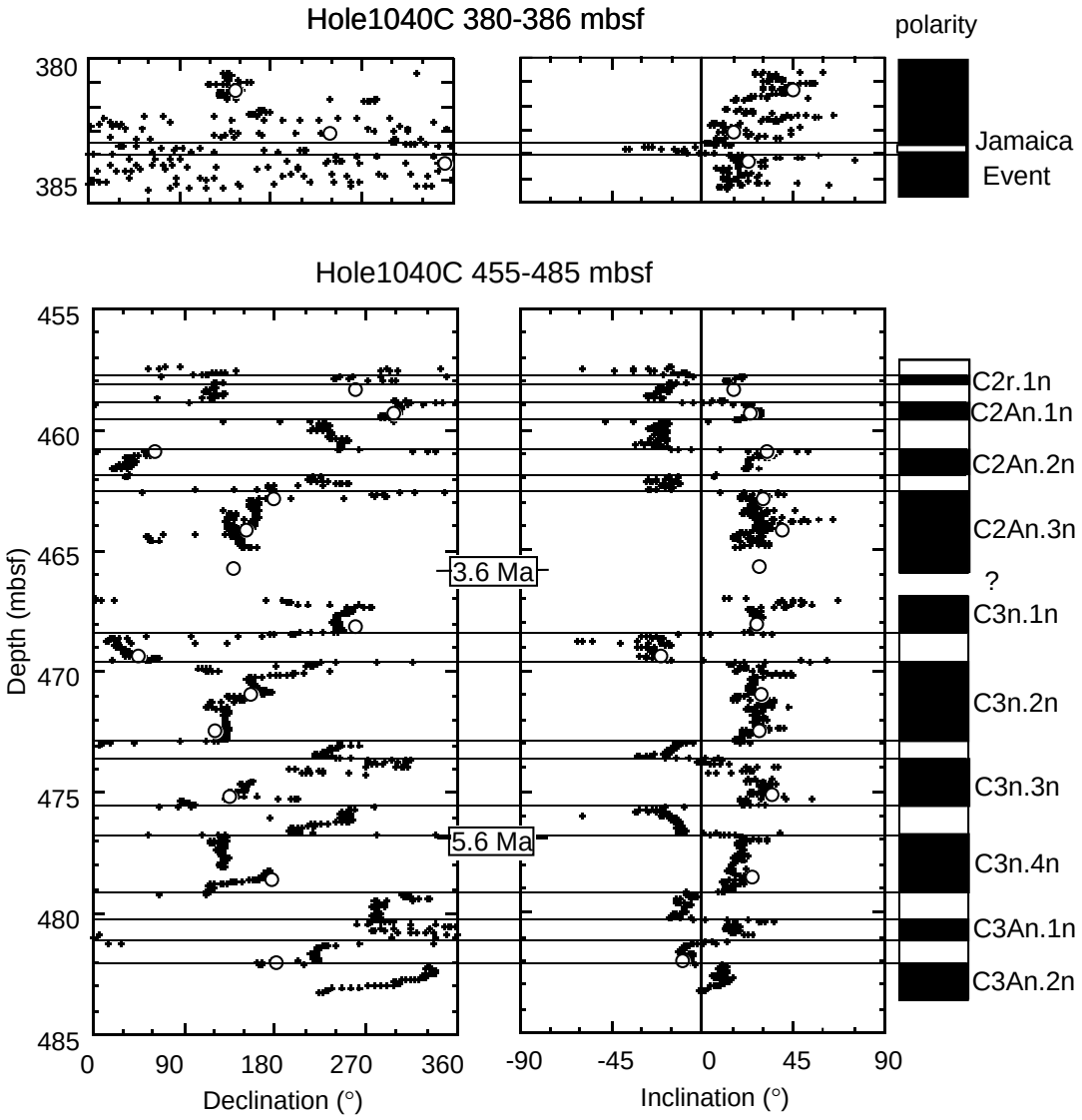

Figure 22. Declinations and inclinations of remanence after 20-mT demagnetization of split cores from Hole 1040C, intervals 380–386 mbsf and 455–485 mbsf (crosses), and from discrete samples (circles). The interpreted magnetostratigraphy, with the horizon of Jamaica event, and normal polarity chrons from Berggren et al. (1995a, 1995b) are shown on the right.

with the exception of a single ash layer at 180 mbsf that serves as a fluid conduit. The chemical composition of all the wedge sediments indicates significant contributions from the volcanic arc. The subducted Ba flux beneath Costa Rica is comparable to, or slightly larger than, that of Guatemala.

Gas Results

Volatile Hydrocarbons

Volatile gases (methane, ethane, and propane) were measured routinely in the sediments of Site 1040 as part of the shipboard safety and pollution-prevention monitoring program. The results are displayed in Table 12 and Figure 23. Methane concentrations in the headspace volumes range between 3 and 116,561 ppmv. The C_1 concentration profile can be divided into three zones. In the uppermost part of Unit P1, the methane increases sharply from 3 ppmv at 1.5 mbsf to 8996 ppmv at 28.5 mbsf (Fig. 23A). The interval from 28.5 to 374 mbsf is characterized by generally high concentrations ranging from 4818 to 116,561 ppmv. Below the base of the décollement (see "Lithostratigraphy and Structures" section, this chapter), methane decreases considerably to 4 ppmv and remains low throughout the whole underthrust sequence. Ethane and propane were also detected. The downhole profiles for ethane and propane measured by the headspace technique are shown in Figure 23B and 23C, respectively. Both compounds are absent in the first two cores of Hole 1040B. Ethane and propane are first detected at a depth of 28.5 mbsf. Ethane concentrations show a maximum of 209 ppmv at 45.8 mbsf. Below this depth, the ethane concentrations decrease and vary between 5 and 78 ppmv. In the subducted sediments, ethane is almost absent. Propane concentrations show two distinct maxima of 24 ppmv (between 191 and 203.6 mbsf) and 19 ppmv (between 348.2 and 357.8 mbsf). These two intervals of higher propane concentrations are characterized by anomalies in composition of the pore waters (see below), suggesting a significant input of allochthonous thermogenic gas. Below 374 mbsf, only small amounts of propane were detected throughout the whole underthrust section.

The first obvious gas voids occurred at about 71.8 mbsf, and vacutainer samples were taken whenever voids were observed. The results are displayed in Table 13. The gas voids were found to contain hydrocarbons in the C_1 (methane) to C_5 (pentane) range. The hydrocarbon concentrations are significantly higher (up to 99.9 vol%) than those obtained by headspace technique, but they present similar gas

Table 11. Depths of biostratigraphic and magnetostratigraphic datums for underthrust sediments of Hole 1040C.

Depth (mbsf)	Nannofossil datums (Ma)	Diatom datums (Ma)	Foraminifer datums (Ma)	Paleomagnetic datums (Ma)
371.21				
376.20				
383.70				0.20
385.60				
397.88				
405.74	0.46			
417.37				
425.30		0.62		
432.57			0.74	
446.73	1.47			
454.17	1.95			
457.80				2.14
458.00				2.15
458.80				2.58
459.70				3.04
460.90				3.11
461.90				3.22
462.60				3.33
466.26	3.60			
468.50				3.58
469.50				4.18
476.80				5.89
476.89	5.60			
479.20				6.14
480.30				6.27
481.30				6.57
482.10				6.94
483.46			8.30	
491.79		9.66		
502.33	10.80		11.40	
511.76		11.34		
523.13	11.50		11.90	
531.31		12.40	12.50	
544.31		12.86		
553.94		13.20	12.70	
563.46	13.60		14.60	
568.57		14.03		
579.31			15.10	
590.02				
598.86				
611.78				
621.45				
629.99	15.60			
636.95				14.89
637.82				15.03
638.28		15.00		
639.30				15.16
646.55			16.10	

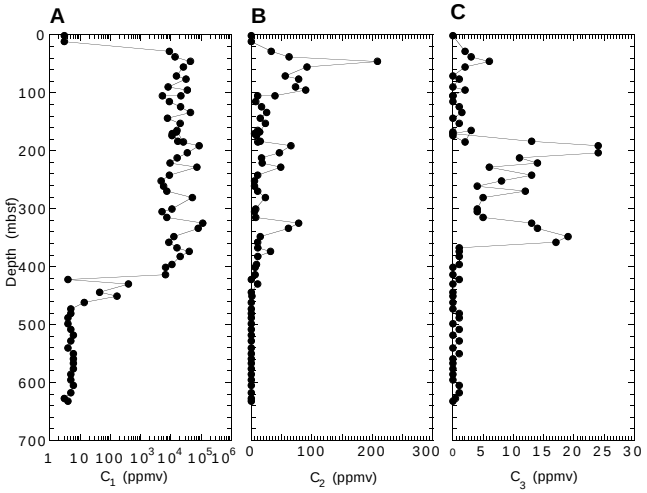

Figure 23. Results of headspace gas analyses for (**A**) methane, (**B**) ethane, and (**C**) propane vs. depth.

Table 12. Composition of headspace gases.

Core, section, interval (cm)	Depth (mbsf)	C_1 (ppmv)	C_2 (ppmv)	C_3 (ppmv)	C_1/C_2
170-1040B-					
1H-2, 0-5	1.53	3	0	0	ND
2H-5, 0-5	11.53	3	0	0	ND
5X-2, 0-5	28.53	8,996	33	2	273
6X-2, 0-5	37.93	13,779	62	3	222
7X-1, 0-5	45.83	43,884	209	6	210
8X-1, 0-5	55.23	25,970	92	2	282
9X-5, 0-5	70.83	15,540	56	0	278
10X2 0-5	75.93	31,933	78	1	409
11X-5, 0-5	90.03	8,339	73	0	114
12X-2, 0-5	95.13	36,432	90	2	405
13X-5, 0-5	105.13	21,384	39	0	548
14X-3, 0-5	105.33	5,395	10	0	540
15X-5, 0-5	115.07	8,992	7	0	1,285
16X-2, 0-5	124.43	21,060	17	1	1,239
17X-2, 0-5	134.03	44,529	25	2	1,781
18X-3, 0-5	143.73	7,742	15	0	516
19X-5, 0-5	153.33	20,399	23	1	887
20X-5, 0-5	167.43	15,678	14	0	1,120
21X-4, 0-5	174.03	10,926	9	0	1,214
22X-4, 0-5	185.13	25,997	11	2	2,363
170-1040C-					
1R-5, 0-5	165.33	15,727	11	3	1,430
2R-2, 0-5	170.33	11,251	5	0	2,250
3R-4, 0-5	183.93	17,266	15	13	1,151
4R-3, 0-5	191.03	87,043	65	24	1,339
5R-5, 0-5	203.63	35,431	46	24	770
6R-4, 0-5	211.83	16,619	17	11	978
7R-4, 0-5	221.43	9,527	18	14	529
8R-2, 0-5	228.03	74,653	49	6	1,524
9R-5, 0-5	242.13	9,097	10	13	910
10R-5, 0-5	251.83	4,818	5	8	964
11R-5, 0-5	261.43	5,711	5	4	1,142
12R-4, 0-5	269.63	7,510	10	12	751
13R-5, 0-5	280.73	50,886	23	5	2,212
15R-5, 0-5	300.13	10,936	7	4	1,562
16R-2, 0-5	305.23	5,127	5	4	1,025
17R-2, 0-5	314.83	7,434	7	5	1,062
18R-2, 0-5	324.53	116,556	78	13	1,494
19R-2,0-5	334.13	81,593	61	14	1,338
20R-5, 0-5	348.23	12,724	15	19	848
21R-5, 0-5	357.83	8,767	10	17	877
22R5 0-5	367.43	15,730	11	1	1,430
23R-3, 0-5	374.03	41,065	32	1	1,283
24R-2, 0-5	382.13	20,466	11	1	1,861
25R-5, 0-5	396.23	11,064	9	1	1,229
26R-2, 0-5	401.33	6,842	6	0	1,140
27R-4, 0-5	413.93	6,644	6	0	1,107
28R-3, 0-5	422.13	4	0	1	ND
29R-2, 0-5	430.13	399	10	0	40
30R-5, 0-5	444.23	46	0	0	ND
31R-3, 0-5	450.83	169	1	0	169
32R-4, 0-5	461.93	14	0	0	ND
33R-5, 0-5	473.03	5	0	0	ND
34R-4, 0-5	481.23	5	0	1	ND
35R-2, 0-5	487.93	4	0	1	ND
36R-3, 0-5	499.03	4	0	0	ND
37R-4, 0-5	508.63	5	0	1	ND
38R-3, 0-5	518.33	6	0	0	ND
39R-3, 0-5	527.93	5	0	1	ND
40R-5, 0-5	540.53	4	0	0	ND
41R-5, 0-5	550.13	6	0	1	ND
42R-5, 0-5	559.13	6	0	0	ND
43R-3, 0-5	566.43	6	0	0	ND
44R-3, 0-5	576.13	6	0	0	ND
45R-3, 0-5	585.73	5	0	0	ND
46R-3, 0-5	595.33	5	0	0	ND
47R-3, 0-5	604.93	6	0	1	ND
48R-5, 0-5	617.63	5	0	1	ND
49R-5, 0-5	627.23	3	0	1	ND
50R-2, 0-5	632.33	4	0	0	ND
51R-2, 0-5	641.93	4	0	1	ND

Notes: C_1, C_2, and C_3 represent methane, ethane, and propane, respectively. ppmv = parts per million by volume. ND = not determined.

This table also appears on the volume CD-ROM.

Table 13. Results of vacutainer gas analyses.

Core, section, interval (cm)	Depth (mbsf)	C_1 (ppmv)	$C_{2=}$ (ppmv)	C_2 (ppmv)	C_3 (ppmv)	*i*-C_4 (ppmv)	*n*-C_4 (ppmv)	*i*-C_5 (ppmv)	*n*-C_5 (ppmv)	*i*-C_6 (ppmv)	*n*-C_6 (ppmv)	C_1/C_2
170-1040B-												
9X-5, 94-95	71.75	706,183	ND	858	2	3	ND	ND	ND	ND	ND	823.06
11X-6, 51-52	92.02	1,000,000	ND	1,561	43	ND	ND	ND	ND	ND	ND	640.62
14X-5, 146-147	111.27	748,078	ND	351	ND	ND	ND	ND	ND	ND	ND	2,131.28
15X-4, 130-131	119.21	1,000,000	ND	504	ND	ND	ND	ND	ND	ND	ND	1,984.13
16X-4, 130-131	128.71	985,594	ND	631	4	ND	ND	ND	ND	ND	ND	1,561.96
17X-2, 80-81	134.81	973,670	ND	686	6	ND	ND	ND	ND	ND	ND	1,419.34
18X-2, 104-105	144.75	986,157	ND	564	6	ND	ND	ND	ND	ND	ND	1,748.51
19X-2, 53-54	153.84	1,000,000	ND	550	7	1	ND	ND	8	ND	ND	1,818.18
20X-3, 49-50	164.90	1,000,000	ND	519	6	ND	ND	ND	ND	ND	ND	1,926.78
21X-3, 81-82	174.82	1,000,000	ND	542	3	ND	ND	ND	ND	ND	ND	1,845.02
170-1040C-												
3R-2, 58-59	180.49	989,668	ND	577	74	ND	ND	ND	ND	ND	ND	1,715.20
6R-2, 106-107	209.87	1,000,000	ND	595	48	23	ND	4	ND	ND	ND	1,680.67
7R-2,144-145	219.85	1,000,000	ND	540	155	25	1	9	ND	ND	ND	1,851.85
8R-3, 98-99	230.49	1,000,000	ND	472	80	26	ND	5	ND	ND	ND	2,118.64
9R-7, 10-11	245.21	899,795	13	456	73	16	ND	5	ND	ND	ND	1,973.24
10R-5, 68-69	252.49	1,000,000	ND	405	169	18	ND	6	ND	ND	ND	2,469.14
11R-3, 56-57	258.97	689,227	ND	473	27	8	ND	ND	ND	ND	ND	1,457.14
12R-1, 143-144	266.54	511,807	ND	226	21	17	7	5	ND	ND	3	2,264.63
18R-1, 22-23	323.23	926,349	ND	444	44	13	ND	ND	ND	ND	ND	2,086.37
19R-1, 96-97	333.57	1,000,000	36	730	36	12	ND	1	ND	ND	ND	1,369.86
20R-1, 148-149	343.68	799,386	ND	595	64	25	ND	3	ND	ND	ND	1,343.51
21R-4, 82-83	357.13	984,169	ND	781	76	29	ND	1	ND	ND	ND	1,260.14

Notes: C_1 = methane, $C_{2=}$ = ethylene, C_2 = ethane, C_3 = propane, *i*-C_4 = iso-butane, *n*-C_4 = n-butane, *i*-C_5 = iso-pentane, *n*-C_5 = n-pentane, *i*-C_6 = iso-hexane, *n*-C_6 = n-hexane, and C_1/C_2 = methane/ethane ratio. ND = not determined.

ratios for equivalent depth intervals. The difference between headspace and vacutainer data is explained by the different sampling techniques causing a loss of the more mobile methane before sealing the headspace sediment in the glass vial (Stein et al., 1995). Between 209.8 and 357.2 mbsf, small amounts of higher molecular weight hydrocarbons were detected, probably reflecting an admixture of thermogenic gas.

Pore-Water Results

Chloride and Salinity

The concentration depth profile of dissolved chloride (Fig. 24A; Table 14) is dominated by (1) a distinct shift in Cl concentration across the décollement, from lower than seawater values in the deformed wedge to approximately seawater values in the underthrust section, and (2) the nonsteady-state profile in the deformed wedge with several Cl minima and their absence in the underthrust section. Concentrations of other components, especially of Ca and the Na/Cl values, indicate dilution with a fresher, significantly lower Cl fluid that must be advected from deeper in the deformed wedge. In situ production of such a low-Cl fluid from clay minerals or opal-A dehydration at the very low geothermal gradient of <1°C/100 m is implausible. Simple dilution by gas hydrate dissociation would not affect the Ca or Na concentrations when normalized to Cl concentrations. The origin of this low-Cl fluid that both permeates the deformed wedge section and migrates along the conduits at ~180 mbsf and at the décollement is deep seated, as indicated by its elevated Ca concentration, lower Mg/Cl and higher Na/Cl values, and the association with ethane and propane, which are produced at >90°–100°C. At the décollement conduit, the Cl concentration is ~13% more dilute than the seawater Cl concentration, and at the ~180 mbsf minimum, it is ~29% more dilute. The higher dilution at the shallower conduit is an artifact of gas hydrate dissociation, which also dilutes the other components analyzed by the same proportion. Small amounts of disseminated gas hydrate and high methane concentrations are present through the deformed wedge section (Fig. 23A), between about 20 mbsf and the décollement zone. The gas hydrate distribution is uneven, with somewhat higher concentrations in the coarser and ash-rich intervals, as clearly depicted in the Cl concentration profile in which the less distinct minima reflect elevated gas hydrate concentrations and hence dissociation and dilution. A very distinct Cl minimum associated with gas hydrate dissociation occurs at ~90 mbsf; at this depth all the other less-reactive components analyzed show a proportional dilution. The only gas hydrate sample recovered and immediately frozen is associated with a carbonate concretion, Sample 170-1040C-11R-2, 49–52 cm; the gas hydrate filled the pores of this concretion.

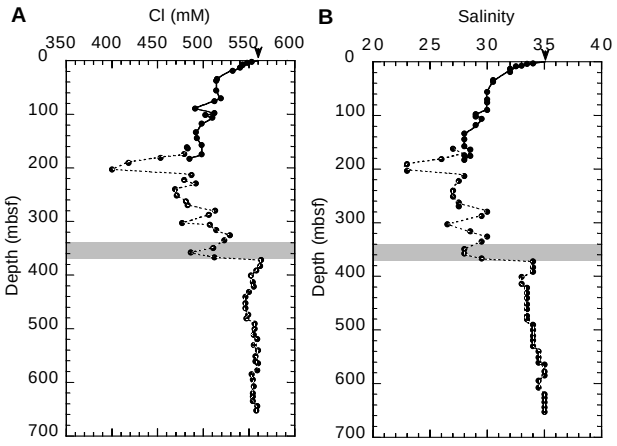

Figure 24. Concentration depth profiles of (**A**) Cl and (**B**) salinity. Arrow = seawater concentration.

Like the Cl concentration depth profile, the salinity depth profile (Fig. 24B) divides the sediment section into two section. One is a low-salinity zone (20%–25% lower than seawater salinity) in the deformed wedge with superimposed salinity minima at the fluid conduit horizons and gas hydrate dissociation. The second section is a seawater salinity zone in the underthrust section that is most similar to the salinity profile at the reference Site 1039.

Sodium and Potassium

Except for the two sections with low Na/Cl at the top of the deformed wedge and underthrust sediment and the two small maxima at ~180 mbsf and the décollement, the Na/Cl values in the pore waters are similar to the seawater value (Fig. 25A). The origin of the two distinct low-Na/Cl zones is as yet unclear, because there is no known diagenetic reaction that involves Na uptake at the very low temperatures encountered at this site, except for uptake by clay minerals into

Table 14. Pore-water chemical data of major and minor constituents, Site 1040.

Core, section, interval (cm)	Depth (mbsf)	Volume (cm^3)	pH	Alkalinity (mM)	Salinity	Cl (mM)	SO_4 (mM)	Mg (mM)	Ca (mM)	K (mM)	Na (mM)	Si (µM)	NH_4 (µM)	PO_4 (µM)	Na/Cl	Mg/Ca
170-1040A-																
1H-2, 140-150	2.95	12	7.76	4.71	34.00	553	23.8	50.4	9.9	13.5	466	422	795	7.5	0.84	5.07
1H-5, 140-150	7.45	10	7.93	6.77	33.00	543	18.0	48.1	8.9	11.9	453	384	614	9.1	0.83	5.38
170-1040B-																
1H-3, 135-150	4.43	50	7.67	6.25	33.50	548	20.6	47.5	9.0	12.90	463	763	567	9.9	0.85	5.30
2H-2, 135-150	8.43	28	8.00	8.50	32.50	543	13.6	47.4	7.9	10.80	449	678	991	24.4	0.83	5.99
2H-5, 135-150	12.93	17	8.05	9.84	32.00	540	7.8	48.4	6.9	10.40	435	587	1,361	35.0	0.80	7.03
4X-1, 110-120	19.15	34	7.92	13.05	32.00	532	2.9	41.8	5.8	10.60	432	761	2,318	42.2	0.81	7.20
5X-2, 135-150	34.43	24	7.82	13.67	30.50	515	0.0	39.2	5.7	9.90	415	824	3,355	11.7	0.81	6.88
6X-1, 130-150	37.80	24	7.90	13.48	30.50	514	0.0	39.0	6.0	10.10	414	761	3,773	8.5	0.81	6.54
8X-1, 74-84	55.99	12	ND	ND	30.00	514	0.0	36.1	6.4	10.40	419	646	4,532	17.5	0.81	5.64
9X-4, 124-144	70.64	26	8.10	14.22	30.00	519	0.0	34.3	5.3	10.40	429	543	5,016	11.8	0.83	6.43
10X-1, 130-150	75.80	20	7.91	12.92	30.00	512	0.0	33.2	6.9	9.00	423	577	6,007	18.7	0.83	4.85
11X-4, 130-150	89.90	24	ND	ND	30.00	491	0.0	28.3	6.8	8.50	412	350	8,562	5.4	0.84	4.15
12X-3, 125-150	97.98	15	7.96	12.65	29.00	512	0.0	25.6	7.5	9.24	437	443	11,640	6.1	0.85	3.42
13X-2, 120-150	101.95	28	8.04	12.06	29.00	502	0.0	23.0	7.1	10.10	432	474	13,487	7.9	0.86	3.26
14X-2, 120-150	106.70	25	7.87	12.00	29.50	510	0.0	24.0	7.6	9.90	437	658	13,795	7.5	0.86	3.18
15X-4, 125-150	117.73	20	8.08	13.45	29.00	498	0.0	22.3	7.1	9.70	430	504	13,736	ND	0.86	3.15
17X-1, 120-150	133.90	22	7.81	13.99	28.00	492	0.0	22.6	7.3	9.30	423	642	12,748	4.7	0.86	3.08
18X-2, 120-150	145.05	13	ND	ND	28.00	493	0.0	22.2	6.8	9.20	426	498	13,607	ND	0.86	3.25
19X-4, 120-150	157.65	38	8.28	11.72	28.00	498	0.0	19.4	6.6	10.10	436	411	15,488	5.5	0.88	2.94
20X-2, 120-150	164.25	19	7.99	12.29	28.50	483	0.0	21.6	7.0	9.80	416	479	13,123	ND	0.86	3.08
21X-3, 120-150	175.35	14	8.03	10.88	28.50	498	0.0	21.7	7.6	8.50	431	490	13,057	ND	0.87	2.87
22X-2, 120-150	183.45	20	8.10	9.25	28.00	485	0.0	20.9	8.1	9.00	418	360	11,022	2.3	0.86	2.59
170-1040C-																
WSTP		10.5	ND	ND	35.10	557	28.2	53.7	10.8	10.4	474	134	28	0.5	0.85	4.99
1R-2, 120-150	162.15	8	ND	ND	27.00	482	0.0	21.7	11.4	8.3	408	215	11,209	ND	0.85	1.91
2R-4, 115-150	174.63	10	ND	ND	28.00	479	0.0	21.2	12.1	7.4	405	390	9,516	ND	0.85	1.75
3R-2, 115-150	181.65	6	ND	ND	26.00	453	0.0	ND	ND	6.4	ND	95	8,500	ND	ND	ND
4R-2. 120-150	190.85	4	ND	ND	23.00	418	0.0	13.5	16.7	3.9	354	121	ND	ND	0.85	0.81
5R-4, 115-150	203.45	4	ND	ND	23.00	400	0.0	11.9	19.1	3.8	334	117	ND	ND	0.84	0.62
6R-4, 120-150	213.15	8	ND	ND	28.00	487	0.0	ND	ND	5.2	ND	102	7,261	ND	ND	ND
7R-4, 120-150	222.75	10	ND	ND	27.50	479	0.0	18.8	16.8	4.9	403	97	6,715	1.1	0.84	1.11
8R-2, 115-150	229.33	4	ND	ND	ND	492	0.0	ND	ND	5.2	ND	197	ND	ND	ND	ND
9R-3, 115-150	240.43	5	ND	ND	27.00	469	0.0	ND	ND	5.1	ND	134	ND	ND	ND	ND
10R-4, 115-150	251.63	7	ND	ND	27.00	471	0.0	ND	ND	4.7	ND	115	5,884	ND	ND	ND
11R-5, 115-150	262.73	8	ND	ND	27.50	481	0.0	21.0	16.3	4.0	403	121	5,730	ND	0.84	1.29
12R-3, 115-150	269.43	6	ND	ND	27.50	483	0.0	ND	ND	4.3	ND	97	ND	ND	ND	ND
13R-4, 75-110	280.13	5	ND	ND	30.00	513	0.0	20.9	19.4	5.5	427	106	ND	ND	0.83	1.08
14R-3, 0-35	287.58	5	ND	ND	29.50	506	0.0	ND	ND	4.6	ND	91	ND	ND	ND	ND
15R-6, 115-150	302.93	5	ND	ND	26.50	477	0.0	15.4	19.4	4.0	403	69	ND	ND	0.85	0.80
16R-2, 120-150	306.55	6	ND	ND	ND	507	0.0	ND	ND	4.4	ND	80	ND	ND	ND	ND
17R-2, 115-150	316.13	8	8.36	6.08	28.50	514	0.0	19.6	19.5	4.3	432	104	5,699	ND	0.84	1.01
18R-2, 115-150	325.83	10	ND	ND	30.00	529	0.0	20.3	20.5	4.5	443	124	6,499	ND	0.84	0.99
19R-2, 115-150	335.43	7	ND	ND	29.50	523	0.0	17.7	21.1	4.5	441	78	6,530	ND	0.84	0.84
20R-5, 115-150	349.53	3	ND	ND	28.00	511	0.0	ND	ND	4.3	ND	80	ND	ND	ND	ND
21R-4, 115-150	357.73	3	ND	ND	28.00	486	0.0	12.9	22.9	3.3	411	84	ND	ND	0.85	0.56
22R-4, 115-150	367.23	10	ND	ND	29.50	512	0.0	28.9	10.1	6.8	427	352	6,345	4.2	0.83	2.86
23R-1, 115-150	372.33	60	7.97	35.583	34.00	563	0.0	45.3	5.0	11.5	451	965	3,851	62.4	0.80	9.04
24R-2, 120-150	383.45	60	8.00	39.33	34.00	562	0.0	47.3	4.1	11.7	447	952	3,210	85.8	0.80	11.54
25R-1, 125-150	391.58	60	7.79	35.79	34.00	558	0.0	43.8	4.8	11.8	449	926	2,617	66.5	0.80	9.19
26R-1, 125-150	401.18	50	7.79	31.862	33.00	552	2.5	43.0	5.4	11.7	448	917	2,066	48.2	0.81	8.00
27R-3, 125-150	413.78	55	7.79	22.024	33.00	554	6.7	42.5	6.6	11.7	457	923	1,562	29.2	0.83	6.48
28R-2, 125-150	421.98	60	7.79	17.50	33.50	555	13.0	43.0	8.8	12.1	465	949	1,388	18.2	0.84	4.92
29R-2, 118-150	431.44	75	7.79	14.989	33.50	550	14.4	42.5	9.4	11.7	463	1,010	ND	ND	0.84	4.52
30R-2, 125-150	441.05	55	7.87	14.884	33.50	546	15.8	42.7	10.4	11.2	460	943	983	18.0	0.84	4.11
31R-3, 125-150	452.18	52	7.87	13.259	33.50	546	17.9	42.3	10.7	11.8	464	978	929	8.7	0.85	3.93
32R-3, 125-150	461.78	37	7.92	9.352	33.50	546	18.5	42.7	10.9	12.0	464	917	820	5.1	0.85	3.93
33R-5, 120-150	474.35	50	7.98	7.025	33.50	549	19.2	42.1	11.2	12.1	469	843	731	2.7	0.85	3.76
34R-3, 125-150	481.08	75	7.71	4.131	33.50	547	20.1	42.7	10.8	12.5	468	1,065	661	1.7	0.86	3.96
35R-3, 132-150	490.82	70	7.72	3.677	34.00	556	21.6	43.3	12.1	12.2	476	1,028	557	1.7	0.86	3.57
36R-3, 135-150	500.43	35	7.56	3.166	34.00	556	20.2	43.3	12.1	11.9	474	1,132	515	1.5	0.85	3.58
37R-4, 135-150	511.53	40	7.56	2.824	34.00	555	21.7	44.4	13.1	11.5	472	1,178	459	1.5	0.85	3.39
38R-3, 130-150	519.7	45	7.5	2.806	34.00	559	21.6	44.0	12.9	11.8	476	1,140	417	1.3	0.85	3.40
39R-4, 115-150	530.73	70	7.53	2.756	34.00	555	22.4	42.6	14.0	11.6	475	1,149	388	1.3	0.86	3.03
40R-4, 130-150	540.4	45	7.58	2.844	34.50	560	23.4	43.5	14.4	11.5	480	1,201	333	1.1	0.86	3.02
41R-5, 130-150	551.5	34	7.57	2.594	34.50	557	23.3	43.6	14.5	11.7	476	1,184	307	1.1	0.85	3.00
42R-5, 130-150	561.1	50	7.66	2.668	34.50	557	24.1	43.3	15.9	10.7	476	1,286	270	1.1	0.85	2.73
43R-1, 130-150	564.8	47	7.63	2.77	35.00	560	24.9	43.2	16.4	10.5	480	1,426	235	ND	0.86	2.63
44R-3. 126-150	577.48	50	7.68	2.699	35.00	559	25.2	43.3	16.5	11.8	478	1,291	229	ND	0.85	2.62
45R-2, 130-150	585.6	50	7.65	2.065	35.00	553	24.4	43.3	16.0	10.9	472	1,230	224	1.1	0.85	2.70
46R-2, 130-150	595.2	47	7.65	2.043	34.50	554	23.9	43.5	15.7	11.5	472	1,243	210	ND	0.85	2.77
47R-4, 130-150	607.8	46	7.66	1.997	34.50	555	24.8	43.4	16.2	11.8	474	1,238	181	1.1	0.85	2.68
48R-6, 130-150	620.5	46	7.66	1.508	35.00	554	25.8	43.2	16.2	12.3	474	1,184	163	ND	0.86	2.66
49R-4, 115-150	627.0	70	7.87	1.618	35.00	554	25.8	43.7	16.6	12.7	473	1,195	147	1.1	0.85	2.64
50R-3, 130-150	635.2	50	8.08	1.393	35.00	554	26.3	43.6	16.7	12.2	474	1,147	116	1.3	0.86	2.61
51R-3, 120-140	644.7	30	8.14	1.603	35.00	559	27.2	40.5	14.9	10.4	492	645	72	ND	0.88	2.73
52R-2, 125-150	652.88	44	8.44	1.811	35.00	558	28.0	45.3	16.7	10.2	480	380	54	1.5	0.86	2.71
53R	Gabbro sill 659.60-665. 00 mbsf															

Note: ND = not determined.

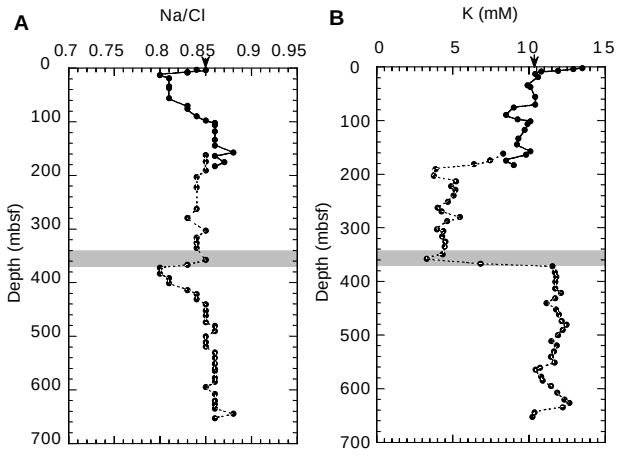

Figure 25. Depth profiles of (**A**) Na/Cl and (**B**) K concentrations. Arrow = seawater concentration.

the interlayer exchange sites or by zeolite formation. The clay uptake, however, happens almost instantaneously upon exposure to seawater; assuming that for some reason the exchange with seawater Na has been delayed, the magnitude of the decrease in the Na/Cl values observed at this site would have required an almost pure clay section to exchange all its ion-exchange sites with Na, an impossible scenario in a mixed-electrolyte solution like seawater. Also, no zeolite-rich sediments were observed. Furthermore, in organic matter–rich sediments of >1 wt% total organic carbon (TOC), as in the deformed wedge and the hemipelagic underthrust sediments at this site, an increase in the Na/Cl values near the sediment/seawater interface is expected, because the ammonium produced displaces Na and K from the clay ion-exchange sites, producing ammonium clays, evident at the very top of the K concentration depth profile in Figure 25. Possibly the Na uptake is related to carbonate diagenesis at these depth intervals at this site. The two Na/Cl minima provide important insights into the chemistry and thus into fluid-sediment reactions at the source of the low-Cl fluid that was migrating from greater depths.

In addition to the high-K concentrations at the top of the deformed wedge section caused by ion exchange with ammonium, as discussed above, the K-concentration depth profile (Fig. 25B) clearly divides the deformed wedge sediments into two parts, with the boundary at the ~180 mbsf fluid conduit. The underthrust section has its own distinct chemical signature. The rather constant, but significantly lower, K concentrations between ~180 mbsf and the décollement supports the conclusion that the lower deformed wedge sediments have undergone a different history of diagenesis and have been permeated by a fluid from an elevated temperature source of 80°–120°C where the illitization reaction is effective. The K-concentration minima at ~180 mbsf and the décollement conduit horizons further indicate that the migrating deep-seated fluid is depleted in K. The K-depletion signature of this fluid also provides an approximate upper limit to the temperature at the source of ~<150°C. Above this approximate temperature, fluid-rock reactions leach K from rocks.

Sulfate, Alkalinity, Ammonium, and Phosphate

The steep sulfate concentration gradient, which reaches zero-sulfate concentration at <35 mbsf in the deformed wedge section (Fig. 26A), indicates that sediment accumulation rates are very high, greater than 100–150 m/m.y. Below this depth, the deformed wedge sediments remain anaerobic and are within the zero-sulfate zone. High methane concentrations therefore prevail throughout the zero-sulfate zone, as shown in Figure 23A, providing an environment conducive to gas hydrate formation. The zero-sulfate zone extends below

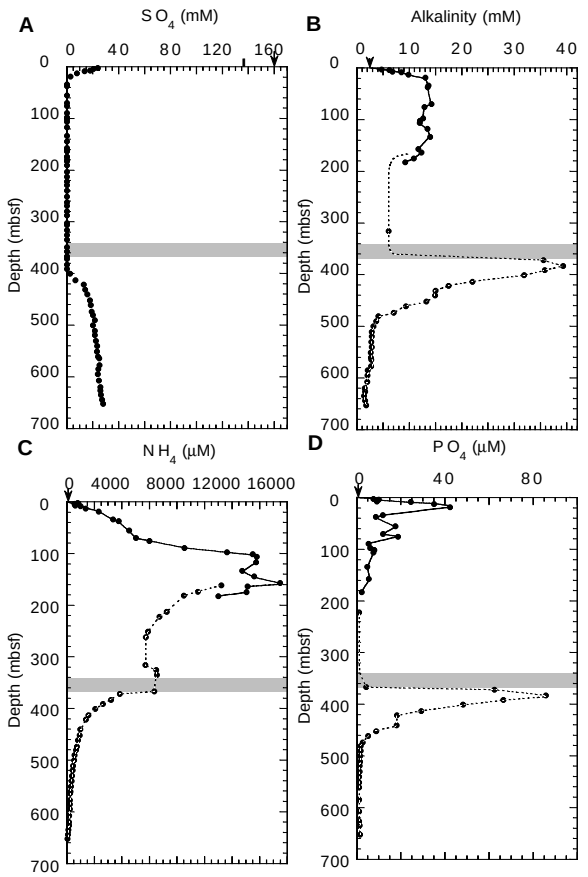

Figure 26. Concentration depth profile of (**A**) sulfate, (**B**) alkalinity, (**C**) ammonium, and (**D**) phosphate. Arrow = seawater concentration.

the décollement, despite the fact that at Site 1039 the minimum sulfate concentration encountered at ~24 mbsf is 13.2 mM. Upon underthrusting, the supply of sulfate from seawater by diffusion ceased, and the underthrust sulfate-reducing bacteria utilized the remaining sulfate at the top of the section, depleting it to zero concentration. The deeper pelagic section has been partially depleted; unless dissolved sulfate is supplied from below, sulfate depletion will migrate arcward. The consequence of the more intense sulfate reduction in the hemipelagic section of the underthrust sediment is alkalinity production, which promotes carbonate formation. The maximum alkalinity at the top of the underthrust section of 39.33 mM (Fig. 26B) is more than twice the maximum alkalinity at Site 1039. Alkalinity is also high in the deformed wedge sediments above the ~180 mbsf boundary and lower in the lower deformed wedge section. The most interesting feature of Figure 26 is the truncated nature of the sulfate and alkalinity concentration profiles at the very top of the underthrust section. The truncation prevents either profile from showing the complete uppermost portion of typical sulfate reduction and alkalinity production profiles, or the complete evolution from seawater concentration to the minimum and maximum concentrations, respectively, as seen in the corresponding concentration depth profiles of Site 1039. Because of its complete depletion at the top few meters of the section and its very different nature when compared with the profile at Site 1039, the sulfate profile cannot be used for estimating the truncation thickness. On the basis of the alkalinity profile, corrected for porosity reduction, the truncation is >3 m (±1 m).

The ammonium and phosphate concentration profiles (Fig. 26C, D) are also truncated at their top. Because of the intense ammonium production at zero-sulfate concentrations, ammonium concentrations

are much higher in the underthrust section than at the reference Site 1039; therefore, the ammonium profile is not suitable for the truncation calculation. The phosphate profile, however, which peaks above the sulfate minimum depth and is independent of sulfate reduction, can be used for this purpose. Indeed, except for the truncation at the very top of the underthrust section, the phosphate concentrations at Sites 1039 and 1040 are almost identical. After correcting for porosity reduction, only ~3 m (±1 m) are missing from the top.

The very high ammonium concentrations in the deformed wedge section, especially above the ~180 mbsf conduit, suggest that sediment accumulation rates are high and that the pore-water system is practically closed. Therefore, the ammonium produced after exchanging with clay minerals remains buried in the section.

Calcium, Magnesium, and Silica

The Ca and Mg concentrations and the Mg/Ca value (Fig. 27) depth profiles divide the sediment column into three geochemically distinct sections: two are in the deformed wedge, and the third is the underthrust section. In the deformed wedge, above the ~180 mbsf boundary, Ca concentrations decrease rapidly at first and then remain constant at about 50% of seawater concentration; concurrently, Mg concentrations decrease steadily to ~120 mbsf, then more gradually below. The Mg/Ca values reflect the relative intensities of involvement of Ca and Mg in carbonate formation reactions, which are most important in the uppermost 100–120 m and below 180 m. In the uppermost ~20 m of the section, Ca is the important player, but at the depth of maximum alkalinity and minimum sulfate concentrations, Mg becomes the important player. Because of high sedimentation rates, the system is practically closed geochemically; therefore seawater cannot diffuse in to replenish the Ca and Mg utilized for carbonate formation. Within the lower deformed wedge section, however, Ca is introduced by the deep-seated fluid. Because this fluid has low-Mg concentrations, the Mg/Ca values at this depth interval are low and range from 2 to 3 in the lower deformed wedge section. At such low values of Mg/Ca, calcite diagenesis, but not dolomite diagenesis, occurs in the presence of sufficient alkalinity, for kinetic reasons.

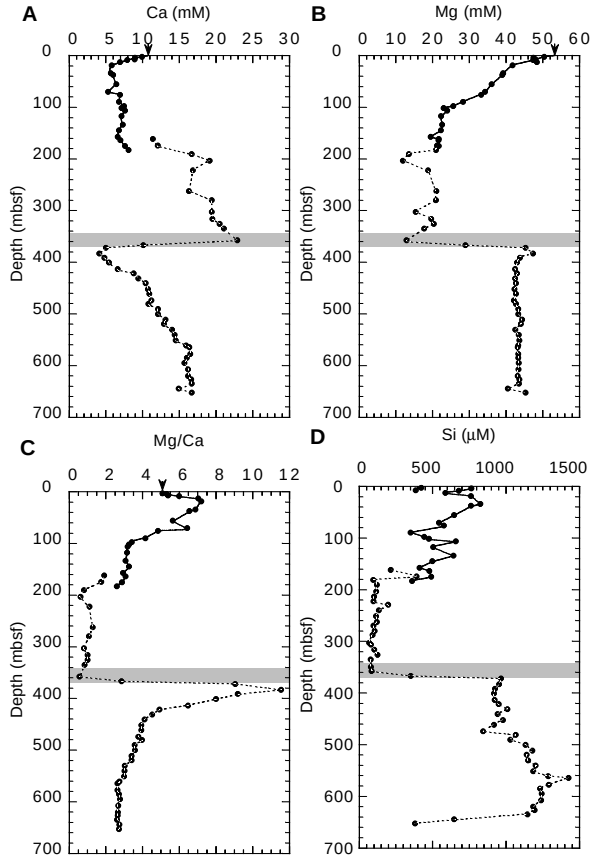

Figure 27. Concentration depth profiles of (**A**) Ca, (**B**) Mg, (**C**) Mg/Ca, and (**D**) silica. Arrow = seawater concentration.

In the underthrust section, both Ca and Mg concentrations are generally lower than at the reference site in the corresponding depth and age intervals. Upon underthrusting, the pore waters lost communication with bottom water, and the geochemical supply of sulfate by diffusion into the sulfate reduction zone ceased. Consequently, alkalinity production slowed down. Ca and Mg diffusion from bottom water ceased as well, resulting in the sharp discontinuity in the concentrations of Ca and Mg across the décollement (Fig. 27B).

In the lower part of the deformed wedge, the low and relatively constant Si concentrations suggest either more mature Si diagenesis (with all the opal-A transformed to the less soluble Si phases) or the absence of opal-A in the original sediment. The latter possibility would, however, imply an original lithology that is different from what is observed. The deep-seated fluid is not enriched in dissolved Si.

The underthrust section has the highest Si concentrations as a result of the abundance of diatoms. The Si concentration depth profile of the underthrust section is almost identical in detail to the profile observed at Site 1039, despite the considerable compaction of the underthrust section by nearly 33%, suggesting that lateral fluid flow prevails. Vertical advection would have erased or at least smoothed out the details of this concentration profile.

The very low-Si concentrations observed at the bottom of the section may indicate communication with a low-Si fluid conduit like seawater, or may be the result of reaction with the underlying gabbro. The return to seawater concentration is, however, less clear at this site in the Ca concentration profile, possibly because of the more elevated position of the gabbro in the sediment section and the greater distance from the basement seawater conduit, which is suggested by preliminary paleomagnetic dating of the gabbro. At this site, only dissolved Si, sulfate, and possibly Mg show clear trends of a return to their seawater concentration, whereas Cl concentration, salinity, and Na/Cl are at seawater values throughout the bottom half of the underthrust section.

Sediment and Igneous Rock Results

Inorganic Carbon, Organic Carbon, and Total Sulfur

The results of inorganic and organic carbon, calcium carbonate, nitrogen and sulfur analyses in the sediments from Holes 1040B and 1040C are presented in Table 15 and Figure 28. Sediments were generally analyzed at a frequency of three samples per core.

Weight percentage of calcium carbonate ($CaCO_3$) was calculated from the inorganic carbon concentrations, assuming that all of the carbonates are present as pure calcite. In the upper 470 mbsf, $CaCO_3$ contents are characterized by relatively small-scale variations (0.7–8.9 wt%). The $CaCO_3$ concentrations of the sediments in the underthrust section show the same distinct patterns as reported for the sediments at Site 1039 and correspond to lithologic Units U1–U3 (see "Lithostratigraphy and Structures" section, "Site 1039" chapter, this volume). Below the décollement, $CaCO_3$ varies from 0.5 to 87.8 wt% (Fig. 28A). TOC data for Site 1040 are presented in Figure 28B and in Table 15. TOC contents range from almost zero to 2.1 wt%. In Unit P1, TOC fluctuates between 0.06 and 1.65 wt%. The highest concentrations in this unit occur between 357 and 360 mbsf. In the upper part of the underthrust sediments (371–416.3 mbsf), TOC ranges between 0.60 and 2.08 wt%. The lowermost interval of the sedimentary sequence is characterized by low-TOC concentrations ranging from zero to 0.82 wt%. Total sulfur (TS) concentrations at Site 1040 in the hemipelagic sediments (Units P1, U1 and U2; 0–497 mbsf) vary be-

Table 15. Inorganic carbon, calcium carbonate, total carbon, total organic carbon, total nitrogen, total sulfur, and TOC/TN in sediments.

Core, section, interval (cm)	Depth (mbsf)	IC (wt%)	$CaCO_3$ (wt%)	TC (wt%)	TOC (wt%)	TN (wt%)	TS (wt%)	TOC/TN
170-1040B-								
1H-2, 12-13	1.63	0.45	3.7	1.54	1.09	ND	0.24	ND
1H-4, 12-13	4.63	0.30	2.5	1.09	0.79	ND	0.14	ND
2H-2, 133-134	2.84	0.63	5.2	1.89	1.26	ND	0.31	ND
2H-3, 37-38	3.38	0.33	2.7	1.10	0.77	0.09	0.53	9
2H-5, 136-137	7.37	0.58	4.8	1.61	1.03	ND	ND	ND
4X-1, 92-93	18.33	0.09	0.7	1.23	1.14	ND	0.11	ND
5X-2, 132-133	29.83	0.55	4.6	1.76	1.21	ND	1.64	ND
6X-2, 1-2	37.92	0.62	5.2	1.73	1.11	ND	1.38	ND
7X-CC, 1-2	44.32	0.90	7.5	2.30	1.40	ND	0.96	ND
8X-CC, 2-3	53.73	0.81	6.7	1.90	1.09	ND	0.13	ND
9X-2, 34-35	66.65	0.56	4.7	1.36	0.80	0.11	0.70	7
9X-4, 118-119	70.49	0.13	1.1	1.06	0.93	ND	ND	ND
9X-6, 34-35	72.65	0.81	6.7	ND	ND	ND	ND	ND
10X-1, 128-129	75.69	0.94	7.8	1.78	0.84	ND	0.08	ND
11X-2, 33-34	85.84	0.78	6.5	2.07	1.29	0.16	0.53	8
11X-4, 127-128	89.78	0.47	3.9	1.07	0.60	ND	0.06	ND
11X-5, 34-35	90.35	0.72	6.0	ND	ND	ND	ND	ND
12X-3, 122-123	97.83	0.39	3.2	1.39	1.00	ND	0.08	ND
13X-2, 31-32	100.92	0.90	7.5	1.90	1.00	ND	ND	ND
13X-2, 118-119	101.79	1.00	8.3	ND	ND	ND	ND	ND
14X-2, 24-25	105.55	0.83	6.9	1.85	1.02	ND	0.72	ND
14X-3, 2-3	106.83	0.64	5.3	ND	ND	ND	ND	ND
14X-6, 34-35	111.65	0.78	6.5	1.67	0.89	0.17	0.59	5
15X-2, 35-36	115.26	0.60	5.0	1.34	0.74	ND	0.00	ND
15X-4, 124-125	119.15	0.49	4.1	ND	ND	ND	ND	ND
16X-2, 34-35	124.75	0.73	6.1	1.71	0.98	ND	0.00	ND
16X-6, 34-35	130.75	0.77	6.4	ND	ND	ND	ND	ND
17X-2, 33-34	134.34	0.62	5.2	1.98	1.36	ND	0.38	ND
18X-2, 32-33	144.03	0.90	7.5	1.82	0.92	ND	0.00	ND
18X-2, 108-109	144.79	1.07	8.9	ND	ND	ND	ND	ND
19X-2, 33-34	153.64	0.77	6.4	2.02	1.25	ND	0.25	ND
19X-4, 115-116	157.46	0.68	5.7	ND	ND	ND	ND	ND
19X-6, 38-39	159.69	0.61	5.1	1.55	0.94	0.17	0.35	6
20X-2, 34-35	163.25	0.69	5.7	1.41	0.72	ND	0.27	ND
20X-2, 119-120	164.1	0.77	6.4	ND	ND	ND	ND	ND
20X-6, 34-35	169.25	1.02	8.5	1.92	0.90	ND	0.00	ND
21X-2, 35-36	172.86	0.75	6.2	2.03	1.28	ND	0.72	ND
21X-3, 106-107	175.07	0.33	2.7	ND	ND	ND	ND	ND
21X-6, 31-32	178.82	0.41	3.4	1.46	1.05	ND	0.21	ND
22X-2, 26-27	182.37	0.80	6.7	1.77	0.97	ND	0.00	ND
22X-2, 112-113	183.23	0.61	5.1	ND	ND	ND	ND	ND
22X-4, 132-133	186.43	0.30	2.5	0.36	0.06	ND	0.00	ND
170-1040C-								
1R-2, 34-35	161.15	0.55	4.6	1.79	1.24	0.18	ND	7
1R-4, 34-35	164.15	0.26	2.2	1.42	1.16	0.16	0.02	7
2R-2, 34-35	170.65	0.95	7.9	2.04	1.09	0.16	0.30	7
2R-4, 34-35	173.65	0.84	7.0	1.94	1.10	0.16	0.03	7
3R-2, 34-35	180.25	0.52	4.3	1.97	1.45	0.20	1.24	7
3R-4, 36-37	183.27	0.41	3.4	1.68	1.27	0.18	1.38	7
3R-5, 32-33	184.73	0.31	2.6	1.33	1.02	0.17	0.44	6
4R-1, 34-35	188.35	0.43	3.6	1.24	0.81	0.15	0.22	5
4R-2, 113-114	190.64	0.40	3.3	1.56	1.16	0.16	0.57	7
5R-2, 33-34	199.44	0.62	5.2	1.32	0.70	0.16	0.59	4
5R-6, 34-35	205.45	0.57	4.7	1.85	1.28	0.17	0.61	8
6R-2, 34-35	209.15	0.38	3.2	1.64	1.26	0.16	1.04	8
6R-4, 34-35	212.15	0.26	2.2	1.19	0.93	0.14	ND	7
7R-2, 115-116	219.56	0.18	1.5	1.20	1.02	0.14	0.38	7
7R-4, 35-36	221.76	0.51	4.2	1.47	0.96	0.14	ND	7
8R-2, 34-35	228.35	0.55	4.6	1.59	1.04	0.15	0.27	7
8R-3, 1-2	229.52	0.53	4.4	1.91	1.38	0.16	0.28	9
8R-5, 40-41	232.91	0.53	4.4	1.58	1.05	0.15	0.14	7
9R-2, 34-35	237.95	0.48	4.0	1.57	1.09	0.16	0.65	7
9R-4, 34-35	240.95	0.68	5.7	1.98	1.30	0.16	ND	8
9R-6, 34-35	243.95	0.52	4.3	1.66	1.14	0.15	0.57	8
10R-2, 30-31	247.61	0.16	1.3	ND	ND	ND	ND	ND
10R-4, 32-33	250.63	0.39	3.2	1.43	1.04	0.14	ND	7
11R-2, 29-30	257.2	0.27	2.2	1.17	0.90	0.14	0.61	6
11R-4, 33-34	260.24	0.24	2.0	ND	ND	ND	ND	ND
11R-5, 107-198	262.48	0.30	2.5	1.36	1.06	0.14	0.17	8
12R-2, 32-33	266.93	0.39	3.2	1.42	1.03	0.15	1.18	7
12R-3, 105-106	269.15	0.27	2.2	1.55	1.28	0.14	ND	9
13R-2, 34-35	276.55	0.40	3.3	1.13	0.73	0.12	1.38	6
13R-4, 34-35	279.55	0.21	1.7	1.25	1.04	0.13	0.11	8
13R-6, 34-35	282.55	0.33	2.7	1.18	0.85	0.14	1.22	6
14R-3, 53-54	286.94	0.20	1.7	1.02	0.82	0.13	0.21	6
14R-4, 32-33	288.23	0.17	1.4	0.67	0.50	0.12	1.22	4
15R-2, 34-35	295.95	0.96	8.0	1.91	0.95	0.15	0.30	6
15R-4, 34-35	298.95	0.24	2.0	0.90	0.66	0.14	0.32	5
15R-6, 34-35	301.95	0.33	2.7	1.15	0.82	0.15	0.60	5
16R-2, 34-35	305.55	0.35	2.9	1.22	1.33	0.14	1.12	10
16R-2, 111-112	306.32	0.29	2.4	ND	ND	ND	ND	ND
17R-1, 75-76	314.06	0.41	3.4	1.43	1.02	0.15	0.88	7
17R-2, 103-104	315.84	0.34	2.8	1.13	0.79	0.15	0.68	5
18R-2, 33-34	324.84	0.15	1.2	1.30	1.15	0.14	0.47	8
19R-2, 33-34	334.44	0.48	4.0	1.75	1.27	0.13	0.53	10
19R-4, 35-36	337.46	0.60	5.0	1.42	0.82	0.13	1.22	6
20R-2, 36-37	344.07	0.27	2.2	1.33	1.06	0.14	0.55	8
20R-4, 32-33	347.03	0.19	1.6	1.16	0.97	0.14	1.62	7
20R-6, 33-34	350.04	0.48	4.0	1.95	1.47	0.15	0.65	10
21R-2, 35-36	353.66	0.47	3.9	1.49	1.02	0.10	ND	10

Table 15 (continued).

Core, section, interval (cm)	Depth (mbsf)	IC (wt%)	$CaCO_3$ (wt%)	TC (wt%)	TOC (wt%)	TN (wt%)	TS (wt%)	TOC/TN
21R-4, 112-113	357.43	0.20	1.7	1.72	1.52	0.17	0.34	9
21R-6, 34-35	359.65	0.66	5.5	2.31	1.65	0.20	1.73	8
22R-2, 33-34	363.24	0.27	2.2	1.06	0.79	0.13	0.97	6
22R-4, 113-114	367.04	0.52	4.3	1.44	0.92	0.15	0.31	6
22R-6, 33-34	369.24	0.18	1.5	1.71	1.53	0.16	0.67	10
23R-1, 108-109	372.09	0.38	3.2	1.81	1.43	0.18	0.57	8
23R-2, 33-34	372.84	0.11	0.9	1.84	1.73	0.22	0.35	8
24R-1, 117-118	381.78	0.04	0.3	0.79	0.75	0.11	0.28	7
24R-2, 33-34	382.44	0.29	2.4	1.17	0.88	0.12	0.22	7
24R-4, 30-31	385.41	0.14	1.2	2.22	2.08	0.23	0.89	9
25R-1, 112-113	391.33	0.13	1.1	1.65	1.52	0.18	0.45	8
25R-2, 36-37	392.07	0.19	1.5	1.58	1.39	0.16	0.49	9
25R-4, 37-38	395.08	0.08	0.7	1.43	1.35	0.14	0.39	10
26R-1, 114-115	400.95	0.07	0.6	1.64	1.57	0.18	0.87	9
26R-4, 34-35	404.65	0.09	0.7	1.11	1.02	0.14	0.47	7
27R-2, 33-34	411.24	0.35	2.9	ND	ND	ND	ND	ND
27R-4, 34-35	414.25	0.27	2.2	2.27	2.01	0.18	0.78	11
27R-6, 32-33	417.23	0.28	2.3	1.35	1.07	0.11	0.30	10
28R-2, 34-35	420.95	0.15	1.3	ND	ND	ND	ND	ND
28R-2, 124-125	421.85	0.91	7.6	0.67	0.00	0.09	0.30	ND
28R-4, 34-35	423.95	0.91	7.6	ND	ND	ND	ND	ND
29R-2, 34-35	430.45	0.45	3.7	1.09	0.64	0.10	1.22	6
29R-2, 113-114	431.24	0.19	1.6	ND	ND	ND	ND	ND
30R-2, 31-32	440.02	0.12	1.0	0.76	0.64	0.10	0.50	6
30R-4, 33-34	443.04	0.19	1.6	ND	ND	ND	ND	ND
30R-6, 33-34	446.04	0.05	0.4	0.71	0.66	0.09	0.48	7
31R-2, 35-36	449.66	0.31	2.5	ND	ND	ND	ND	ND
31R-3, 113-114	451.94	0.22	1.8	0.82	0.60	0.09	0.60	7
31R-4, 34-35	452.65	0.46	3.8	ND	ND	ND	ND	ND
32R-2, 34-35	459.25	0.09	0.7	ND	ND	ND	ND	ND
32R-3, 122-123	461.63	0.20	1.7	0.98	0.78	0.10	0.19	8
32R-6, 32-33	465.23	0.50	4.2	ND	ND	ND	ND	ND
33R-2, 32-33	468.83	0.49	4.1	0.76	0.27	0.04	0.12	7
33R-4, 38-39	471.89	0.93	7.7	1.35	0.42	0.06	0.14	7
33R-5, 119-120	474.2	0.27	2.2	ND	ND	ND	ND	ND
34R-2, 33-34	478.54	1.91	15.9	2.46	0.55	0.06	0.26	9
34R-3, 125-126	480.96	5.80	48.3	5.70	0.00	0.05	0.09	0
34R-4, 34-35	481.55	1.21	10.1	ND	ND	ND	ND	ND
35R-3, 123-124	490.64	0.20	1.6	0.40	0.20	0.06	0.36	3
35R-4, 40-41	491.31	0.09	0.7	ND	ND	ND	ND	ND
36R-2, 34-35	497.85	5.22	43.5	5.46	0.24	0.05	0.16	5
36R-4, 35-36	500.86	9.86	82.1	ND	ND	ND	ND	ND
37R-2, 34-35	507.45	8.62	71.8	ND	ND	ND	ND	ND
37R-4, 34-35	510.45	9.01	75.1	9.40	0.39	0.00	0.12	ND
37R-4, 133-134	511.44	8.53	71.0	ND	ND	ND	ND	ND
38R-2, 36-37	517.17	10.25	85.4	10.18	0.00	0.00	0.00	ND
38R-4, 7-8	519.88	10.05	83.7	ND	ND	ND	ND	ND
38R-4, 34-35	520.15	10.07	83.9	ND	ND	ND	ND	ND
38R-6, 23-24	523.04	9.49	79.1	10.31	0.82	0.00	0.03	ND
39R-2, 34-35	526.75	8.40	70.0	ND	ND	ND	ND	ND
39R-4, 34-35	529.75	7.27	60.6	7.87	0.60	0.02	0.17	30
40R-2, 33-34	536.34	8.55	71.3	ND	ND	ND	ND	ND
40R-4, 37-38	539.38	9.76	81.3	ND	ND	ND	ND	ND
40R-4, 125-126	540.26	10.11	84.2	ND	ND	ND	ND	ND
40R-6, 33-34	542.34	9.06	75.5	9.13	0.07	0.00	0.33	ND
41R-2, 32-33	545.93	9.93	82.7	ND	ND	ND	ND	ND
41R-4, 24-25	548.85	9.63	80.2	ND	ND	ND	ND	ND
41R-5, 126-127	551.37	9.09	75.8	9.04	0.00	0.00	0.06	ND
42R-2, 35-36	555.56	9.16	76.3	ND	ND	ND	ND	ND
42R-4, 34-35	558.55	8.39	69.9	ND	ND	ND	ND	ND
42R-5, 127-128	560.98	6.26	52.2	ND	ND	ND	ND	ND
43R-1, 128-129	563.19	6.34	52.8	6.71	0.37	0.03	0.10	12
43R-3, 86-87	567.27	5.26	43.8	ND	ND	ND	ND	ND
43R-4, 33-34	568.24	8.54	71.1	ND	ND	ND	ND	ND
44R-2, 28-29	574.89	4.28	35.6	4.54	0.26	0.02	0.28	13
44R-3, 122-123	577.33	5.23	43.6	ND	ND	ND	ND	ND
45R-2, 119-120	585.4	8.17	68.1	ND	ND	ND	ND	ND
45R-4, 89-91	588.1	6.08	50.6	ND	ND	ND	ND	ND
45R-5, 78-79	589.49	7.88	65.6	8.41	0.53	0.00	0.04	ND
46R-2, 33-34	594.14	7.54	62.8	ND	ND	ND	ND	ND
46R-4, 34-35	597.15	9.27	77.2	ND	ND	ND	ND	ND
47R-2, 34-35	603.75	8.23	68.5	ND	ND	ND	ND	ND
47R-4, 34-35	606.75	8.95	74.6	ND	ND	ND	ND	ND
47R-4, 129-130	607.7	9.01	75.0	ND	ND	ND	ND	ND
47R-6, 34-35	609.75	8.66	72.2	8.59	0.00	0.02	0.10	0
48R-2, 34-35	613.45	9.33	77.7	ND	ND	ND	ND	ND
48R-4, 34-35	616.45	7.04	58.6	ND	ND	ND	ND	ND
48R-6, 34-35	619.45	8.36	69.7	ND	ND	ND	ND	ND
48R-6, 126-127	620.37	8.44	70.3	ND	ND	ND	ND	ND
49R-2, 34-36	623.05	7.10	59.1	7.34	0.24	0.00	0.05	ND
49R-4, 34-35	626.05	7.31	60.9	ND	ND	ND	ND	ND
49R-6, 34-36	629.05	6.10	50.8	ND	ND	ND	ND	ND
50R-2, 32-34	632.63	1.95	16.3	ND	ND	ND	ND	ND
50R-3, 104-105	634.85	7.84	65.3	7.83	0.00	0.00	0.00	ND
50R-4, 31-32	635.62	7.46	62.2	ND	ND	ND	ND	ND
51R-2, 44-45	642.35	5.64	46.9	ND	ND	ND	ND	ND
51-3, 116-117	644.57	5.88	49.0	ND	ND	ND	ND	ND
52R-2, 31-32	651.82	5.55	46.2	ND	ND	ND	ND	ND
52R-2, 120-121	652.71	7.70	64.1	8.09	0.39	0.00	0.00	ND

Notes: IC = inorganic carbon, $CaCO_3$ = calcium carbonate, TC = total carbon, TOC = total organic carbon, TN = total nitrogen, and TS = total sulfur. ND = not determined.

This table also appears on the volume CD-ROM.

tween 0 and 1.7 wt% (Fig. 28C; Table 15). High-TS concentrations probably reflect disseminated pyrite and pyrite nodules that are present in the core (see "Lithostratigraphy and Structures" section, this chapter). In pelagic Unit U3 of the subducted sediments, only small amounts of TS (0–0.1 wt%) were detected. Total nitrogen (TN) contents vary between 0.05 and 0.23 wt%, with an average value of 0.13 wt% (Table 15).

Percent Compaction of Underthrust Section

The depth distribution of weight percentage $CaCO_3$ in the underthrust section of Figure 28A and in the corresponding figure for Site 1039 has been used to calculate the percent compaction of the underthrust section. The carbonate content was chosen because in pelagic and hemipelagic sections it most clearly indicates the changes in the prevailing oceanographic conditions, and also because the carbonate content of sediments strongly influences their physical properties and diagenetic behaviors. The division of the sediment column into the same three subsections at Sites 1039 and 1040, based on their carbonate contents, is summarized in Table 16. For Site 1040, the corrected depths were used, and it was assumed that 100% of the sediment section is being subducted. The percent reductions are extremely variable, from 24% in the calcareous section to 62% in the transition section. This is supported by the Si concentration profiles. In Table 16, the total section reduction is given, and the behavior of the low- to moderate-carbonate sections vs. that of the calcareous section is compared, indicating the relative resistance to compaction of high-carbonate sediments. The very high percent of compaction calculated for the transition zone section of Table 16, which corresponds with an interval showing low sedimentation rate, is surprising and difficult to explain; it may represent a mixed signal of compaction plus loss of a portion of this subsection through dissolution.

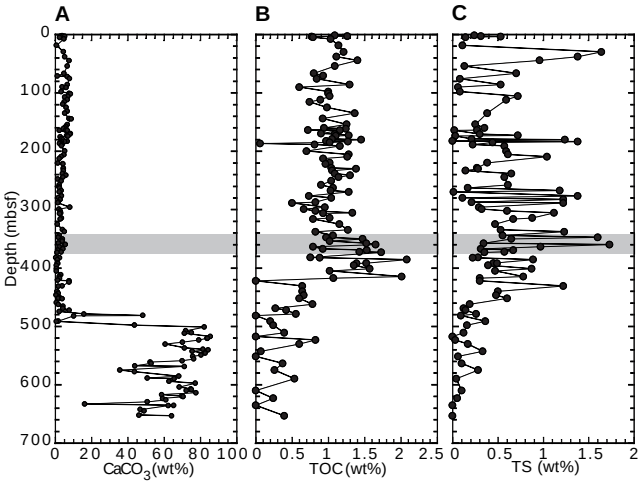

Figure 28. Concentrations of (**A**) carbonate, (**B**) total organic carbon (TOC), and (**C**) total sulfur (TS) vs. depth.

Composition of Organic Matter

To characterize the type of organic matter in the sediments, total organic carbon/total nitrogen (TOC/TN) values, hydrogen index (HI), and oxygen index (OI) values from Rock-Eval pyrolysis have been used. Most of the TOC/TN values range from 6 to 10 (Table 15), which indicate a predominantly marine origin of the organic material (Bordovskiy, 1965; Emerson and Hedges, 1988). TOC/TN values of >10 occur in the lowermost section of the subducted sediments (Unit U3), probably reflecting the presence of small amounts of terrigenous organic material. Data obtained by Rock-Eval pyrolysis do not support the TOC/TN results in general. The moderate- to high-HI values (100–689 mg HC/g TOC; Table 17) reflect the presence of marine-dominated organic matter, but the elevated OI values (up to 244 mg CO_2/g TOC; Table 17) suggest a significant input of terrigenous organic matter. These first estimates of the composition of the organic matter, however, have to be confirmed by more detailed shore-based organic geochemical and microscopical investigations.

X-ray Fluorescence Analyses of the Solid Phases

At Site 1040, the XRF geochemistry may be used to (1) distinguish the top of the underthrust section from the overlying deformed wedge sediments, (2) limit the allowable volumes of accreted sediment with trace element compositions similar to the incoming sediment, (3) demonstrate the chemical homogeneity of the deformed wedge sediments, and (4) evaluate the provenance of the detrital grains that contribute to the deformed wedge sediments. Major and minor element data for silicic sediments, ashes, and gabbros are reported in Table 18, and trace element data are reported in Table 19.

Figure 29 shows Ba, Cu, and Ni plotted against depth. Ba concentrations, which average 426 ppm in Subunits P1A and P1B at and above 367.1 mbsf, jump to an average value of 1575 ppm for samples measured at and below 372.2 mbsf. Concentrations of Cu jump by a factor of three across the décollement at 371 mbsf, and Ni also increases, albeit less dramatically. Cu, Ni, and Ba concentrations below 371 mbsf are sharply different from those of the deformed wedge sediments and are comparable to those of the incoming sediment section (see "Geochemistry" section, "Site 1039" chapter, this volume). A significant increase in Ba, but not Ni or Cu, is seen within the deformed wedge sediments at ~160–180 mbsf. This interval corresponds to an ash layer and a major Avid conduit (see "Pore-Water Results," this section).

The underthrust sediments in Figure 29 show the same sharp increase in Ba, Cu, and Ni that was seen in Site 1039 in the slow sedimentation interval at the base of Unit U2 and the top of Unit U3. At Site 1040, concentrations (Ba = 8862 ppm; Cu = 631 ppm) reach their maxima at 491.6 mbsf, or 120.6 m below the décollement. This stratigraphic marker is seen at 168 mbsf at Site 1039; assuming no accretion, these results suggest 28% compaction in Units U1 and U2.

Table 16. Percent compaction of underthrust section.

	Thickness at Site 1039 (m)	Thickness at Site 1040 (m)	Reduction (%)
Unit U1 & Subunit U2A; hemipelagic clayey section	133	85	36
Subunits U2B & U3A; hemipelagic clayey and transition sections	47	18	62
Subunits U3B & U3C; pelagic calcareous section	220	167	24
	Thickness (m)	**Thickness (m)**	**Reduction (%)**
Total section	400	270	33
Total hemipelagic plus transition sections	180	103	43
Total calcareous	220	167	24

Table 17. Rock-Eval data.

Core, section, interval (cm)	Depth (mbsf)	T_{max} (°C)	S_1 (mg HC/g rock)	S_2 (mg HC/g rock)	S_3 (mg CO_2/g rock)	PI ($S_1 + S_2$)	S_2/S_3	HI (mg HC/g TOC)	OI (mg CO_2/g TOC)	TOC (wt%)
170-1040B-										
1H-2, 12-13	1.63	547	0.3	4.21	1.42	0.07	2.96	386	130	1.09
2H-2, 133-134	2.84	543	1.1	4.47	0.18	0.2	24.83	354	14	1.26
4X-1, 92-93	18.33	399	0.31	7.86	1.17	0.04	6.72	689	102	1.14
5x-2, 132-133	29.83	409	0.16	3.13	1.37	0.05	2.28	258	113	1.21
7X-CC, 1-2	44.32	422	0.37	7.49	1.37	0.05	5.47	535	97	1.40
9X-4, 118-119	70.49	404	0.14	4.38	1.14	0.03	3.84	470	122	0.93
11X-4, 127-128	89.78	448	0.04	0.87	1.28	0.04	0.68	145	213	0.60
13X-2, 118-119	101.79	434	0.12	2.52	1.44	0.05	1.75	252	14	1.00
15X-2, 35-36	115.26	507	0.15	4.66	1.37	0.03	3.40	629	185	0.74
17X-2, 33-34	134.34	419	0.11	2.46	1.46	0.04	1.68	180	107	1.36
19X-2, 33-34	153.64	421	0.16	2.57	1.73	0.06	1.49	205	138	1.25
21X-2, 35-36	172.86	428	0.33	4.05	2.52	0.08	1.61	316	196	1.28
170-1040C-										
1R-2, 34-35	161.15	427	0.26	4.38	1.37	0.06	3.20	353	110	1.24
2R-4, 35-36	173.65	422	0.22	2.85	2.69	0.07	1.06	259	244	1.10
4R-2, 113-114	190.64	436	0.02	4.09	1.04	0	3.93	352	89	1.16
5R-6, 34-35	205.45	446	0.01	3.64	1.48	0	2.46	284	115	1.28
7R-2, 115-116	219.56	418	0.2	3.46	1.38	0.05	2.51	339	135	1.02
8R-3, 1-2	229.52	409	0.17	5.46	1.8	0.03	3.03	395	130	1.38
10R-4, 32-33	250.63	420	0.12	1.65	1.53	0.07	1.08	141	130	1.17
12R-3, 105-106	269.15	416	0.03	3.06	0.99	0.01	3.09	239	77	1.28
13R-4,33-34	279.55	425	0.1	2.24	1.04	0.04	2.15	215	100	1.04
14R-3, 53-54	286.94	427	0.15	2.61	0.82	0.05	3.18	318	100	0.82
15R-4, 34-35	298.95	431	0.03	2.34	0.8	0.01	2.93	354	121	0.66
18R-2, 33-34	324.84	417	0.06	1.5	0.96	0.04	1.56	130	83	1.15
19R-2, 33-34	334.44	445	0.05	1.31	2.27	0.04	0.57	103	178	1.27
20R-2, 36-37	344.07	499	0.05	1.81	1.78	0.03	1.01	170	167	1.06
21R-2, 35-36	353.66	438	0.01	1.03	1.41	0.01	0.73	100	138	1.02
21R-4, 112-113	357.43	433	0.02	2.18	1.7	0.01	1.28	180	140	1.21
23R-2, 33-34	372.84	397	0.38	8.1	3.26	0.04	2.48	468	188	1.73
26R-1, 114-115	400.95	369	1.14	5.96	2.25	0.16	2.64	379	143	1.57
32R-3, 122-123	461.63	378	0.16	2.8	1.72	0.05	1.62	358	220	0.78

Note: T_{max} = temperature (°C) of maximum hydrocarbon generation from kerogen; S_1 = volatile hydrocarbons; S_2 = kerogen-derived hydrocarbons; S_3 = organic CO_2 from kerogen; PI = productivity index; S_2/S_3 = kerogen-type index; HI = hydrogen index; OI = oxygen index; and TOC = total organic carbon obtained by CNS-elemental analyses.

Table 18. Major and minor elements (XRF) for silicic sediments, volcanic ashes, and gabbros.

Core, section, interval (cm)	Sample type	Lithology	Depth (mbsf)	SiO_2	TiO_2	Al_2O_3	Fe_2O_3*	MnO	MgO	CaO	Na_2O	K_2O	P_2O_5	Total	LOI
Prism sediments:															
170-1040B-															
1H-3, 135-150	IWSJ	Silty clay	4.35	60.07	1.02	17.19	8.52	0.090	3.28	3.12	2.34	2.407	0.151	98.18	7.26
4X-1, 110-120	IWSJ	Silty clay	19.10	59.91	1.10	17.52	9.10	0.050	3.63	2.09	2.12	2.305	0.144	97.95	7.55
8X-1, 74-84	IWSJ	Silty clay	55.94	58.95	1.17	18.90	10.05	0.078	3.59	1.72	1.79	2.114	0.149	98.50	9.75
11X-4, 130-150	IWSJ	Silty clay	89.80	58.75	1.16	17.88	10.00	0.090	3.65	2.12	1.84	2.389	0.205	98.07	8.65
15X-4, 125-150	IWSJ	Silty clay	119.05	59.29	1.14	18.01	9.37	0.083	3.65	2.50	1.79	2.104	0.141	98.06	9.00
19X-4, 120-150	IWSJ	Silty clay	157.35	59.20	1.15	18.16	9.55	0.084	3.62	2.46	1.71	2.108	0.174	98.21	8.85
21X-4, 120-150	IWSJ	Silty clay	176.07	55.93	1.07	16.72	12.28	0.159	3.89	3.82	1.68	2.003	0.299	97.83	11.52
170-1040C-															
1R-2, 120-150	IWSJ	Silty clay	162.00	59.06	1.19	17.93	9.90	0.084	3.40	2.65	1.69	2.299	0.181	98.37	9.14
1R-5, 114-120	XRF	Ash	166.44	69.36	0.51	15.05	3.70	0.090	1.13	2.79	2.96	3.013	0.146	98.73	6.98
3R-2, 115-150	IWSJ	Silty clay	181.05	59.30	0.99	17.13	9.55	0.077	3.24	3.69	1.73	2.439	0.214	98.35	7.68
5R-4, 115-150	IWSJ	Silty clay	203.25	61.25	1.10	19.05	8.59	0.061	2.57	1.82	1.71	2.209	0.148	98.49	8.63
8R-2, 115-150	IWSJ	Silty clay	229.15	59.30	1.17	17.52	9.94	0.062	3.63	2.42	1.69	1.929	0.123	97.76	9.68
12R-3, 115-150	IWSJ	Silty clay	269.25	60.07	1.17	18.14	9.46	0.050	3.88	2.19	1.79	2.337	0.117	99.18	8.14
16R-2, 120-150	IWSJ	Silty clay	306.40	58.87	1.12	17.47	9.32	0.067	4.06	3.06	1.79	2.347	0.122	98.21	7.96
17R-2, 115-150	IWSJ	Silty clay	315.95	57.51	1.10	16.93	9.34	0.071	4.01	3.02	1.78	2.372	0.115	96.23	7.57
18R-2, 115-150	IWSJ	Silty clay	325.65	59.39	1.18	17.91	9.89	0.053	4.06	2.27	1.93	2.309	0.115	99.09	7.14
19R-2, 115-150	IWSJ	Silty clay	335.25	59.90	1.24	18.02	9.69	0.062	3.46	1.90	2.01	2.122	0.117	98.50	6.99
20R-5, 115-150	IWSJ	Silty clay	349.35	59.38	1.16	18.34	9.54	0.064	3.54	2.14	1.77	2.204	0.152	98.27	8.89
21R-4, 115-150	IWSJ	Silty clay	357.45	57.98	1.10	17.99	10.13	0.095	3.32	2.64	1.68	2.146	0.214	97.28	9.54
22R-4, 115-150	IWSJ	Silty clay	367.05	56.49	1.19	18.26	9.64	0.065	3.91	4.41	1.78	1.966	0.146	97.84	9.90
Underthrust section:															
170-1040C-															
23R-1, 115-150	IWSJ	Diatom silt-clay	372.15	60.08	1.09	17.00	9.14	0.504	3.65	2.99	2.17	1.958	0.204	98.77	8.30
26R-1, 125-150	IWSJ	Diatom silt-clay	401.05	60.39	1.05	17.82	9.51	0.098	3.64	2.07	2.10	2.103	0.129	98.88	9.15
29R-2, 118-150	IWSJ	Silty clay	431.28	60.80	0.96	16.45	8.53	0.145	3.60	2.78	2.01	2.395	0.098	97.75	9.09
32R-3, 12-13	XRF	Ash	460.52	59.29	1.03	17.09	9.64	0.292	4.65	2.06	2.03	2.133	0.175	98.36	8.12
32R-6, 14-17	XRF	Ash	465.04	51.14	0.64	12.16	10.04	1.508	3.63	14.19	1.72	2.057	0.163	97.24	15.54
33R-5, 120-150	IWSJ	Silty clay	474.20	61.19	0.97	17.77	8.03	0.164	3.93	1.92	2.02	2.186	0.149	98.31	7.96
35R-4, 67-68	XRF	Ash	491.56	69.47	0.52	7.79	4.56	0.247	1.91	8.67	1.94	1.319	0.129	96.53	12.16
46R-1, 39-43	XRF	Ash	592.69	34.41	0.29	3.24	2.14	0.082	-1.17	55.20	0.28	0.457	0.339	95.25	31.38
49R-5, 133-135	XRF	Ash	628.53	63.06	0.46	10.78	4.02	0.155	0.46	12.59	2.83	3.871	0.079	98.29	12.60
52R-3, 56-58	XRF	Glass	653.56	101.63	0.10	0.36	0.61	0.012	0.93	0.22	-0.12	0.059	0.013	103.79	0.45
52R-4, 5-12 (Piece 2)	XRF	Gabbro	653.64	48.79	1.32	15.60	11.92	0.186	6.65	12.41	2.10	0.160	0.126	99.25	-0.46
52R-4, 62-67 (Piece 8)	XRF	Gabbro	654.21	48.65	1.34	15.64	11.94	0.175	6.92	12.36	2.07	0.116	0.126	99.31	0.14
53R-1, 5-11 (Piece 2)	XRF	Gabbro	659.65	48.72	1.33	15.62	11.93	0.181	6.78	12.38	2.08	0.138	0.126	99.28	-0.39
53R-1, 41-44 (Piece 1A)	XRF	Gabbro	660.01	48.80	1.56	15.03	12.59	0.180	7.22	11.60	2.62	0.142	0.147	99.88	0.05
53R-2, 31-36 (Piece 4)	XRF	Gabbro	661.41	48.18	1.26	15.60	11.30	0.167	8.59	12.70	2.14	0.079	0.080	100.08	0.71

Notes: Fe_2O_3* = total iron as Fe_2O_3. All concentrations are in weight percent. IWSJ = interstitial water squeezecakes, XRF = picks from sampling table, and LOI = loss on ignition.

Table 19. Trace element (XRF) analyses for silicic and calcareous sediments, volcanic ashes, and gabbros.

Core, section, interval (cm)	Sample type	Lithology	Depth (mbsf)	Nb	Zr	Y	Sr	Rb	Zn	Cu	Ni	Cr	V	Ce	Ba
170-1040B-															
1H-3, 135-150	IWSJ	Silty clay	4.35	5.9	119.4	19.1	288.1	43.8	11	71	46	88	177	26	735
4X-1, 110-120	IWSJ	Silty clay	19.10	5.4	114.3	19.9	244.8	41.4	129	88	56	106	206	13	438
8X-1, 74-84	IWSJ	Silty clay	55.94	4.8	116.1	19.6	201.5	39.3	110	63	36	76	194	30	392
11X-4, 130-150	IWSJ	Silty clay	89.80	5.0	118.4	24.2	222.8	37.0	103	68	43	89	193	28	37
15X-4, 125-150	IWSJ	Silty clay	119.05	5.1	113.4	19.7	242.8	38.4	112	60	40	80	176	24	414
19X-4, 120-150	IWSJ	Silty clay	157.35	5.4	113.5	19.0	230.4	38.3	115	60	44	82	188	25	354
21X-4, 120-150	IWSJ	Silty clay	176.07	6.2	110.4	28.0	254.5	37.0	112	61	39	70	170	28	331
170-1040C-															
1R-2, 120-15	IWSJ	Silty clay	162.00	6.3	113.5	19.6	240.9	41.9	109	63	37	85	190	24	389
1R-5, 114-120	XRF	Ash	166.44	6.6	145.8	13.9	319.3	54.9	55	24	8	15	55	31	1172
3R-2, 115-150	WSJ	Silty clay	181.05	5.7	102.2	22.2	282.9	40.4	93	44	34	81	173	19	397
5R-4, 115-150	IWSJ	Silty clay	203.25	7.4	125.8	20.7	256.1	34.1	104	57	22	36	166	29	327
8R-2, 115-150	IWSJ	Silty clay	229.15	6.4	109.3	18.4	221.6	38.9	119	71	51	101	189	19	338
12R-3, 115-150	IWSJ	Silty clay	269.25	7.0	110.4	20.8	234.7	46.3	114	69	56	109	188	19	372
16R-2, 120-150	IWSJ	Silty clay	306.40	6.7	109.0	19.5	248.8	46.1	109	70	57	102	191	23	392
17R-2, 115-150	IWSJ	Silty clay	315.95	6.9	108.9	18.2	244.5	47.0	110	69	60	98	194	27	397
18R-2, 115-150	IWSJ	Silty clay	325.65	7.7	112.7	19.7	278.2	42.5	116	75	65	108	204	25	393
19R-2, 115-150	IWSJ	Silty clay	335.25	6.9	120.4	21.5	243.4	35.9	107	62	47	130	197	22	338
20R-5, 115-150	IWSJ	Silty clay	349.35	6.7	115.0	18.9	234.1	41.8	110	65	39	87	196	28	313
21R-4, 115-150	IWSJ	Silty clay	357.45	6.9	125.3	23.1	238.9	40.7	103	69	39	77	190	28	343
22R-4, 115-150	IWSJ	Silty clay	367.05	7.2	112.9	17.9	279.6	39.7	106	57	43	99	191	27	301
23R-1, 115-150	IWSJ	Diatom. silty clay	372.15	5.8	108.8	20.9	270.9	37.6	173	154	78	89	220	18	1701
26R-1, 125-150	IWSJ	Diatom. silty clay	401.05	5.7	114.4	20.5	217.1	42.7	189	146	104	90	195	14	1548
29R-2, 118-150	IWSJ	Silty clay	431.28	6.9	111.8	20.7	270.0	45.2	205	125	107	70	202	20	1785
32R-3, 12-13	XRF	Ash	460.52	5.6	118.7	35.1	325.3	45.2	328	352	348	109	226	4	4170
32R-6, 14-17	XRF	Ash	465.04	4.3	92.4	28.5	521.2	38.1	156	171	311	63	108	16	2480
33R-5, 120-150	IWSJ	Silty clay	474.20	6.4	133.2	37.6	323.8	43.1	218	152	207	83	182	13	5040
35R-4, 67-68	XRF	Ash	491.56	3.9	93.9	35.8	617.7	23.6	488	631	294	32	141	BDL	8862
37R-4, 135-150	IWSJ	Carbonate	511.32	BDL	15.5	12.2	1418.6	2.2	20	45	9	BDL	10	BDL	2756
41R-5, 130-150	IWSJ	Carbonate	551.40	BDL	13.5	9.7	1363.9	1.0	25	37	5	BDL	12	BDL	1850
45R-2, 130-150	IWSJ	Carbonate	585.50	0.8	24.7	9.8	1176.9	4.5	31	44	12	1	23	BDL	2342
46R-1, 39-43	XRF	Ash	592.69	11.0	68.6	17.9	1172.5	11.3	50	31	20	10	35	5	1542
47R-4, 130-150	IWSJ	Carbonate	607.70	BDL	18.7	8.1	1180.6	4.4	21	31	11	1	9	BDL	1932
48R-6, 130-150	IWSJ	Carbonate	620.40	2.4	28.8	16.2	1202.5	7.2	35	88	30	5	15	1	3098
49R-4, 115-150	IWSJ	Carbonate	626.85	4.8	39.7	15.8	1062.6	8.3	43	65	27	6	29	BDL	3089
49R-5, 133-135	XRF	Ash	628.53	105.5	534.0	38.2	453.5	97.4	109	40	27	7	34	124	1301
50R-3, 130-150	IWSJ	Carbonate	635.10	7.6	61.6	18.2	1047.2	9.8	40	61	20	5	26	2	2992
51R-3, 120-140	IWSJ	Carbonate	644.60	14.4	101.7	18.8	992.7	6.8	65	61	33	20	57	12	3681
52R-2, 125-150	IWSJ	Carbonate	652.75	12.0	90.1	21.3	515.5	1.0	106	145	48	48	95	25	578
52R-3, 56-58	XRF	Glass	653.56	0.1	BDL	1.0	0.3	0.8	2	5	3	BDL	2	13	59
52R-4, 5-12 (Piece 2)	XRF	Glass	653.64	8.6	79.3	23.2	161.9	4.4	80	168	84	166	349	24	15
52R-4, 62-67 (Piece 8)	XRF	Gabbro	654.21	8.7	80.2	22.4	160.2	2.8	76	158	84	149	340	27	26
53R-1, 5-11 (Piece 2)	XRF	Gabbro	659.65	9.9	88.2	24.3	172.0	2.3	66	102	82	138	380	29	28
53R-1, 41-44 (Piece 1A)	XRF	Gabbro	660.01	8.9	98.2	24.3	177.2	2.7	70	147	84	163	337	21	23
53R-2, 31-36 (Piece 4)	XRF	Gabbro	661.41	7.8	87.2	21.9	199.3	1.8	51	179	79	194	299	22	27

Notes: All concentrations are in parts per million. IWSJ = interstitial water squeezecakes, XRF = picks from sampling table. BDL = below detection limit.

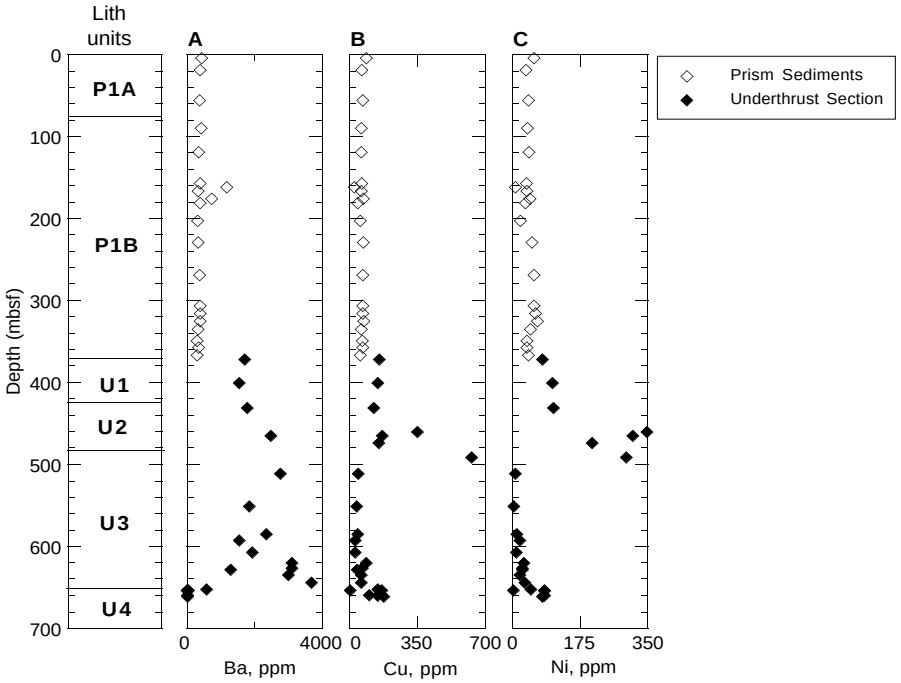

Figure 29. Concentrations of (**A**) Ba, (**B**) Cu, and (**C**) Ni vs. depth for prism and underthrust sediments.

The bottom half of the underthrust section at Site 1040 shows some distinctive characteristics. Concentrations of Cu, Ni, Zn, and V increase in the basal 30–40 m of carbonate. The ash at 628.5 mbsf shows enrichment in Zr, Nb, and Ce, in contrast to the ash at 166 mbsf and similar to that seen in the deeper ash layers at Site 1039, for which a Galapagos origin was proposed. The gabbro suite at Site 1040 has slightly higher average MgO contents and lower TiO_2, K_2O, and incompatible trace element abundances than those at Site 1039, suggesting that the Site 1040 gabbros are slightly less fractionated overall. Trace element ratios suggest a Galapagos origin for these gabbros. A 5-cm-thick glassy interval at the top of the Site 1040 gabbroic section, petrographically identified as quartz and clear glass with stringers of carbonate (see "Lithostratigraphy and Structures" section, this chapter), is almost entirely SiO_2, with very minor amounts of CaO, Fe_2O_3*, MgO, and Al_2O_3.

Figure 30 shows selected major and minor element compositions for the deformed wedge and underthrust sediments. The trace element homogeneity of the deformed wedge sediments (Subunits P1A and P1B) seen in Figure 29 is also seen in the major and minor element data. For many elements, the sediments have compositions indistinguishable from average arc andesite (Wilson, 1989) and Costa Rican andesites, suggesting a volcanic provenance for the deformed wedge sediments. Relative to upper continental crust and post-Archean shales (McLennan and Taylor, 1984), the sediment column has lower SiO_2 and higher Al_2O_3, Ba/Ce, Ba/Rb, and Zr/Nb, which is consistent with the addition of detrital grains with basaltic-andesite or andesite composition (Carr and Rose, 1987). The homogeneity of the deformed wedge sediments is remarkable and contrasts with the larger variability seen at Site 1041 (see "Geochemistry" section, "Site 1041" chapter, this volume). It may suggest mechanical homogeniza-

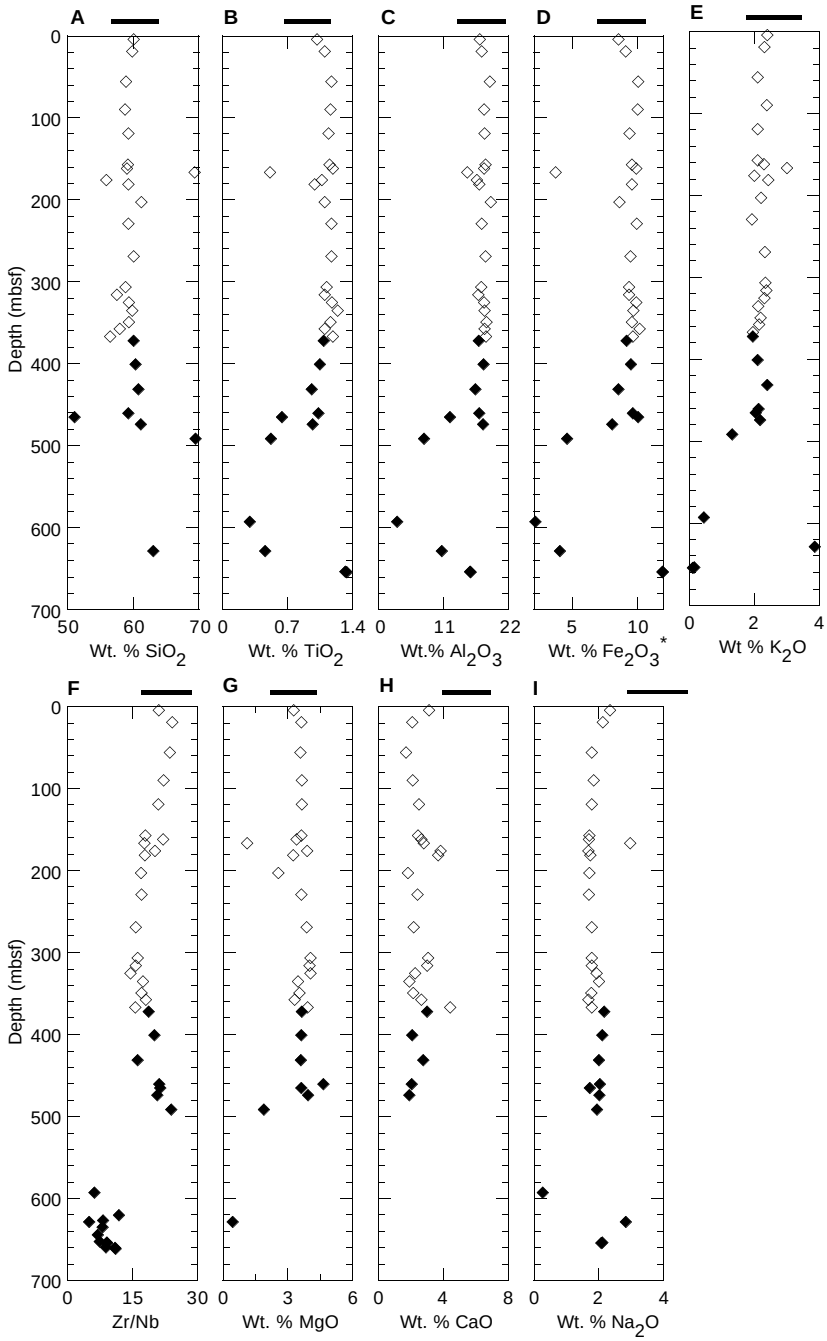

Figure 30. Concentrations of (**A**) SiO_2, (**B**) TiO_2, (**C**) Al_2O_3, (**D**) Fe_2O_3*, (**E**) K_2O, (**F**) Zr/Nb, (**G**) MgO, (**H**) CaO, and (**I**) Na_2O vs. depth. Heavy bar at the top of each panel indicates the values observed for arc andesites (Wilson, 1989).

tion of the sediment column, perhaps during downslope transport and reworking. One departure from this homogeneity is seen at about 166 mbsf, where SiO_2, Na_2O, and K_2O concentrations increase, and Fe_2O_3*, TiO_2, and MgO concentrations decrease. A silicic ash is present at this interval, which also corresponds to a fluid conduit noted previously. There is no change in the chemistry that corresponds to the lower porosity interval at ~200–370 mbsf (see "Physical Properties" section, this chapter). If the detrital particles are indeed derived from the volcanic arc, then it is also striking that concentrations of CaO and Na_2O in the deformed wedge sediments are dramatically lower than expected. Lower CaO concentration in volcanic sands relative to volcanic lavas was also observed in the Izu-Bonin arc (Gill et al., 1994), although to a much lesser extent than observed here. The chemistry may require mixing between detrital grains of volcanic provenance with grains from some other, unidentified source, such as glauconitic or continental clays.

The bulk composition of the underthrust section for K, Rb, Ba, and Sr is shown in Table 20. The lithologically weighted bulk composition has been converted to subducted element fluxes following the method of Plank and Langmuir (1993), and they are reported in Table 21. The convergence rate was taken from Figure 1B of the "Introduction" chapter (this volume). Although the bulk concentration of Ba in the underthrust section at Site 1040 is less than that at Deep Sea Drilling Project Site 495 off Guatemala, the flux is actually slightly higher, reflecting faster convergence beneath Costa Rica.

PHYSICAL PROPERTIES

Density and Porosity

Laboratory Measurements

Site 1040 was cored using APC, XCB, and RCB methods, and the accuracy of physical properties indices varies both with degree of drilling disturbance and the type of sediment being drilled. Gamma-ray attenuation (GRA) bulk density measurements are not considered reliable below ~25 mbsf and are only useful to show relative changes in wet bulk density (Table 22). In intervals with drilling deformation caused by RCB coring (see "Biostratigraphy and Magnetostratigraphy" section, this chapter), a small-scale increase in water-content and porosity measurements occurs (Table 23; Fig. 1). In the overlap zone between APC and XCB cores (the base of Hole 1040A and top of Hole 1040B), the water content is 8%–10% higher in XCB-recovered sediment, presumably because of ingress of drilling slurry. Where overlap occurs between the XCB cores of Hole 1040B and the RCB cores of Hole 1040C, the latter show a distinctly lower porosity and higher bulk density. This suggests that porosity and bulk density measurements on RCB cores are closer to the in situ values measured by wireline and LWD logs (see"Downhole Measurements," this section).

The sediments recovered from Hole 1040A and the upper part of Hole 1040B are relatively undisturbed, and physical properties measurements define an initial steep trend of decreasing porosity from greater than 75% at the seafloor to a value of around 50% at 8 mbsf (Fig 1; Table 23). Bulk density readings reflect this change, increasing to around 1.8 g/cm^3 over the first 10 mbsf. Measurements from 25 to 100 mbsf show a broad decrease in porosity and an increase in bulk density. At greater depth, porosity decreases to an average of 42% at 265 mbsf.

Little change in the consolidation state of the sediment is recorded from a depth of 200 mbsf down to the base of the décollement zone at 371 mbsf. Porosity values are between 35% and 45%, and bulk density measurements increase marginally, probably caused by a slight increase in the density of constituent grains. The exception to this trend is an interval between 272 and 300 mbsf where porosity decreases to an average of only 33%.

The base of the décollement zone, defined by a structural and lithologic boundary (see "Lithostratigraphy and Structures" section, this chapter) is marked by an abrupt change in physical properties between measurements down to and including Core 170-1040C-22R and those from deeper in the hole. Porosity increases by about 15 percentage points to values close to 60%, and wet bulk density decreases from an average of about 1.9 to ~1.7 g/cm^3. Porosity below the décollement horizon remains in a band between 56% and 62%, except for two excursions between 478 and 500 mbsf, and 556 and 580 mbsf, where the average porosity is between 65% and 67%. These devia-

Table 20. Composition of the bulk sediment in the underthrust section at Site 1040.

Unit	Thickness (m)	K_2O (wt%)	Ba (ppm)	Sr (ppm)	Rb (ppm)
U1	49.7	2.03	1625	244	40.2
U2	53.4	2.4	5138	360	42.9
U3	166.5	0.18*	2718	1181	5.9
Total	269.6	0.96	2996	846	19.6

Notes: * = from Plank and Langmuir (1993). Sediment thickness uses corrected depths for Site 1040.

Table 21. Subducted element fluxes in the underthrust sediment at Site 1040, Costa Rica, and Site 495, Guatemala.

Flux (g yr^{-1}cm^{-1})	Guatemala* 495	Costa Rica† 1040
K	1176	1947
Ba	682	773
Sr	262	226
Rb	4.6	4.9

Notes: * = from Plank and Langmuir, 1993. † = using corrected depths.

Table 22. Gamma-ray attenuation (GRA) bulk density data for Site 1040.

Leg	Site	Hole	Core	Type	Section	Top (cm)	Bottom (cm)	Depth (mbsf)	GRA density (g/cm^3)	Measured counts	Actual daq period (s)	Core diameter (cm)
170	1040	A	1	H	1	7.7	7.7	0.08	1.397	1.07E+05	5	6.7
170	1040	A	1	H	1	9.7	9.7	0.1	1.409	1.06E+05	5	6.7
170	1040	A	1	H	1	11.7	11.7	0.12	1.441	1.04E+05	5	6.7
170	1040	A	1	H	1	13.7	13.7	0.14	1.434	1.04E+05	5	6.7
170	1040	A	1	H	1	15.7	15.7	0.16	1.44	1.04E+05	5	6.7
170	1040	A	1	H	1	17.7	17.7	0.18	1.45	1.03E+05	5	6.7
170	1040	A	1	H	1	19.7	19.7	0.2	1.405	1.06E+05	5	6.7
170	1040	A	1	H	1	21.7	21.7	0.22	1.392	1.07E+05	5	6.7
170	1040	A	1	H	1	23.7	23.7	0.24	1.363	1.09E+05	5	6.7
170	1040	A	1	H	1	25.7	25.7	0.26	1.4	1.06E+05	5	6.7

Note: Daq = data acquisition.

This is a sample of the table that appears on the volume CD-ROM.

Table 23. Moisture and density data, and calculated phase relationships from discrete core specimens, Site 1040.

Leg	Site	Hole	Core	Type	Section	Top (cm)	Bottom (cm)	Depth (mbsf)	Wet volume (g/cm^3)	Dry volume (g/cm^3)	Wet mass (g)	Dry mass (g)	Beaker ID	Beaker mass (g)	Beaker volume (g/cm^3)
170	1040	A	1	H	1	25	27	0.25	0	5.95	20.16	13.95	5	8.03	3.62
170	1040	A	1	H	1	72	74	0.72	0	6.19	20.6	14.61	7	8.03	3.62
170	1040	A	1	H	1	130	132	1.3	0	6.93	22.12	16.35	2	8.11	3.65
170	1040	A	1	H	2	50	52	2	0	7.11	22.69	16.88	8	8.02	3.61
170	1040	A	1	H	2	110	112	2.6	0	7.23	23.26	17.15	9	8.09	3.64
170	1040	A	1	H	3	49	51	3.49	0	7.08	21.39	17.11	6	7.95	3.58
170	1040	A	1	H	3	119	121	4.19	0	7.65	23.63	18.56	16	8.08	3.64
170	1040	A	1	H	3	119	121	4.19	0	7.23	22.38	17.63	17	8.02	3.61
170	1040	A	1	H	4	17	19	4.67	0	7.56	23.46	18.36	10	7.89	3.55
170	1040	A	1	H	4	17	19	4.67	0	7.99	25.18	19.52	12	8.07	3.63

Table 23 (continued).

Leg	Site	Hole	Core	Type	Section	Top (cm)	Bottom (cm)	Depth (mbsf)	Water content (wet)	Water content (dry)	Wet bulk density (g/cm^3)	Grain density (g/cm^3)	Porosity (%)	Void ratio	Dry bulk density (g/cm^3)
170	1040	A	1	H	1	25	27	0.25	0.53	1.13	1.43	2.56	73.8	2.82	0.68
170	1040	A	1	H	1	72	74	0.72	0.49	0.98	1.47	2.57	71.03	2.45	0.75
170	1040	A	1	H	1	130	132	1.3	0.43	0.74	1.55	2.53	64.74	1.84	0.9
170	1040	A	1	H	2	50	52	2	0.41	0.7	1.58	2.54	63.36	1.73	0.94
170	1040	A	1	H	2	110	112	2.6	0.42	0.72	1.57	2.54	63.95	1.77	0.92
170	1040	A	1	H	3	49	51	3.49	0.33	0.49	1.73	2.63	55.8	1.26	1.17
170	1040	A	1	H	3	119	121	4.19	0.34	0.51	1.72	2.62	56.64	1.31	1.14
170	1040	A	1	H	3	119	121	4.19	0.34	0.52	1.72	2.67	57.58	1.36	1.14
170	1040	A	1	H	4	17	19	4.67	0.34	0.51	1.71	2.62	56.81	1.32	1.14
170	1040	A	1	H	4	17	19	4.67	0.34	0.52	1.71	2.64	57.33	1.34	1.13

This is a sample of the table that appears on the volume CD-ROM.

tions are equally apparent in the wet bulk density, which indicates that the less dense zones have relatively sharp bases and gradational tops. Grain density is markedly lower in these two intervals, decreasing to values as low as 2.4 g/cm^3 from a background level of around 2.6 g/cm^3. Both wet bulk density and grain density increase sharply in the bottom two cores of Hole 1040C (Cores 170-1040C-51R and 52R). This may result from admixing of ash-derived material or, perhaps, chemical alteration of the calcareous oozes that are related to the gabbroic intrusion. The two samples from the last recovered sediment section may have been contaminated by drilling slurry derived from the underlying gabbro.

Downhole Measurements

In situ density and porosity measurements were collected by the CDN as part of the LWD downhole assembly. The total logged intervals at Holes 1040D and 1040E are from the seafloor to 325 and 307 mbsf, respectively. The results are shown in Figures 1 and 31, and listed in Tables 24 and 25. The differential caliper logs show a very small standoff of ~1 in between the borehole and LWD collars, indicating good hole conditions. Downhole density and porosity measurements roughly correlate with the core specimen measurements (Fig. 1). Correspondence of the values is maintained to about 160 mbsf, where the core-based porosities decrease sharply because of the change from XCB to RCB coring. Although the two profiles from Holes 1040D and 1040E generally show the same trends in density and porosity, they show different log responses in several intervals.

Bulk density profiles show a gradual increasing trend composed of a number of segments with rapid downward decreases between more gradual downward increases. Most of the density values range between 1.7 and 2.0 g/cm^3. Between 0 and 205 mbsf in Holes 1040D and 1040E, the bulk density gradually increases with depth from about 1.7 to 1.9 g/cm^3 with frequent fluctuation. The most distinct change in bulk density values occurs in the interval 204–210 mbsf in both holes, where the values increase from 1.85 to 2.05 g/cm^3 in Hole 1040D and from 1.78 to 2.0 g/cm^3 in Hole 1040E. Most of the values over the interval 210–310 mbsf range between 1.9 and 2.1 g/cm^3 in both holes. Bulk density fluctuates widely between 1.6 and 2.0 g/cm^3 in the interval below 310 mbsf in Hole 1040D. Large negative excursions occur at 84 mbsf (1.55 g/cm^3), 237 mbsf (1.68 g/cm^3), and 310 mbsf (1.60 g/cm^3) in Hole 1040D, and 168 mbsf (1.70 g/cm^3) and 269 mbsf (1.72 g/cm^3) in Hole 1040E.

Porosities calculated directly from the neutron log fluctuate widely throughout the logged interval. Porosity values greater than 100% were removed, and the data set was smoothed by calculating a 9-pt running average. These filtered neutron porosity profiles (Fig. 31; Tables 24, 25) show values ranging from 65% to 50% and a gradual decrease with depth. The porosity profiles generally show a reverse trend to the density profile. However, several low-density intervals have low neutron porosities, for example at 172, 237, and 311 mbsf in Hole 1040D, and at 168 and 271 mbsf in Hole 1040E. These results may be explained by a change in grain density, or may partly be the result of changes in hole conditions.

The wireline High Temperature Lithodensity Tool (HLDT) was deployed at Hole 1040C in an interval between 88 and 222 mbsf (Fig. 32; Table 26). Density values ranged from 1.2 to 1.8 g/cm^3, which are significantly different from the values derived from the CDN tool (1.7–2.0 g/cm^3). Washed-out borehole conditions, which are shown by the caliper log, may be the cause of the low density values.

P-wave Velocity

Laboratory Measurements

P-wave velocities were measured in the upper section of Hole 1040A with the *P*-wave logger (PWL; Table 27) and nominally in two intervals per split section using the PWS3 transducers (Table 28). No measurements could be obtained over the depth interval from 30 to 280 mbsf, even on extracted core specimens (Fig. 33). Several factors might explain this difficulty.

1. The sediment was commonly intensely sheared, at least partially because of disturbance by both the XCB and RCB coring; thus, either no samples could be taken, or microfractures in the samples prevented the propagation of acoustic energy.

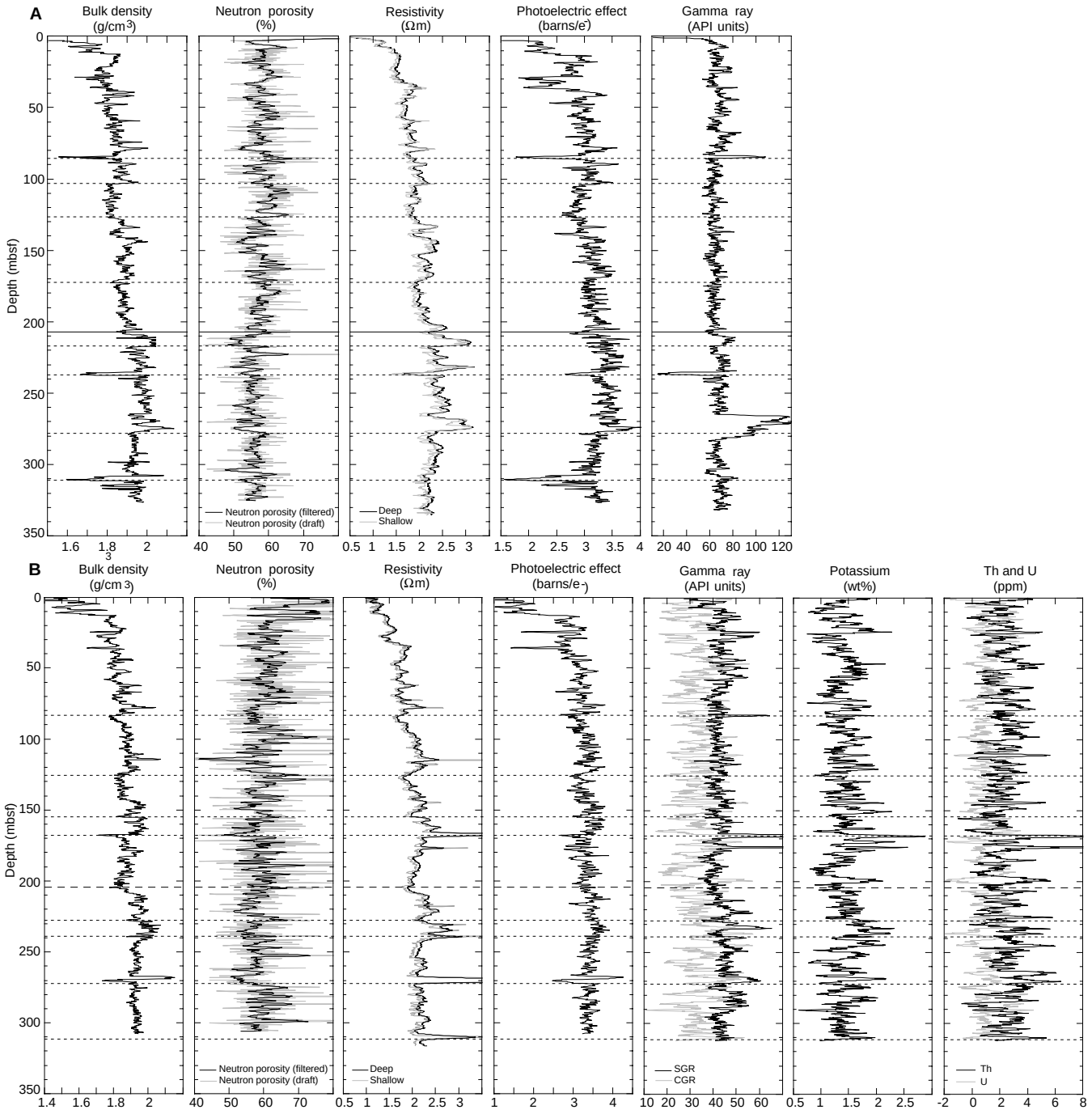

Figure 31. **A.** Summary of LWD data at Hole 1040D. **B.** Summary of LWD data at Hole 1040E. SGR = total spectral gamma ray, and CGR = computed gamma ray.

2. Large parts of the sediment cores may become gas charged and/or damaged by gas escape during the dissociation of gas hydrates (see "Geochemistry" section, this volume). Gas pockets or microcracks then produced significant attenuation of the acoustic energy.

Velocities at the seafloor are ~1600 m/s and increase rapidly with depth to 1700 m/s at 30 mbsf (Fig. 33A). Below this depth velocities increase uniformly, reaching values of 2000–2100 m/s at 335 mbsf, just above the décollement zone. No velocities could be measured within the décollement zone, reflecting the intense structural shearing and fragmentation as well as the significant sediment disturbance by the RCB coring process.

Beneath the décollement, better core quality permitted the collection of velocity data, both on sediment within the split-core liners and on extracted specimens. Velocities at the top of the underthrust section (Subunit U1A) are 1675–1775 m/s, representing a significant velocity decrease relative to velocities in the overlying deposits. Velocities continue to decrease with depth throughout Subunit U1B, and Units U2 and U3. At a depth of 560 mbsf, values drop to an average between 1625 and 1700 m/s. This unusual characteristic reflects differential compaction of the underthrust section, with the lower car-

Table 24. Shipboard composite logging-while-drilling data from Hole 1040D.

Depth (mbrf)	Depth (mbsf)	ROP5 (m/hr)	RTIM (s)	ATR (Ωm)	PSR (Ωm)	GTIM (s)	GR (GAPI)	DTAB (s)	PEF (barns/e⁻)	DRHO (g/cm³)	DC_A (in)	ROMT (g/cm³)	NTAB (s)	TNPH (v/v)
4189.02	0.02	86.4	1650	0.34	0.33	2850	5.26	5390	0.08	–0.02	0	1.09	7280	1.06
4189.17	0.17	48.43	1670	0.34	0.33	2850	5.92	5460	0.08	–0.02	0	1.09	7290	0.94
4189.32	0.32	56.16	1760	0.33	0.31	2890	5.98	5510	0.08	–0.02	0	1.08	7280	0.96
4189.48	0.48	34.07	1760	0.44	0.44	2860	8.02	5550	0.08	–0.02	0	1.08	7250	1.02
4189.63	0.63	31.35	1720	0.66	0.75	2810	20.77	5540	0.08	–0.02	0	1.1	7180	1.07
4189.78	0.78	27.32	1690	0.61	0.69	2810	33.53	5670	0.08	–0.01	0.09	1.13	7250	0.93
4189.93	0.93	20.26	1670	0.71	0.84	2770	41.41	5730	0.08	0.01	0.29	1.17	7190	0.8
4190.09	1.09	21.05	1600	0.74	0.86	2730	46.15	5760	0.14	0.01	0.58	1.22	7230	0.8
4190.24	1.24	11.72	1620	0.87	0.9	2740	51.67	5700	0.21	0.02	0.82	1.25	7130	0.75
4190.39	1.39	12.15	1550	0.92	0.95	2690	54.04	5770	0.2	0.03	0.9	1.27	7120	0.85

Note: ROP5 = 5-ft averaged rate of penetration, RTIM = resistivity time after bit, ATR = attenuation resistivity, PSR = phase shift resistivity, GTIM = gamma-ray time after bit, GR = gamma ray, DTAB = density time after bit, PEF = photoelectric factor, DRHO = bulk density correction, DC_A = differential caliper, ROMT = rotationally processed density, NTAB = neutron time after bit, and TNPH = thermal neutron porosity.

This is a sample of the table that appears on the volume CD-ROM.

Table 25. Shipboard composite logging-while-drilling data from Hole 1040E.

Depth (mbrf)	Depth (mbsf)	ROP5 (m/hr)	ATR (Ωm)	PSR (Ωm)	RTIM (s)	GTIM (s)	GR (GAPI)	THOR (ppm)	URAN (ppm)	POTA (wt%)	CGR (cps)	SGR (cps)	DTAB (s)	PEF (barns/e⁻)	DRHO (g/cm³)	DC_A (in)	ROMT (g/cm³)	NTAB (s)	TNPH (v/v)
4189.02	0.02	36.86	0.96	1.02	750	1950	45.65	3.24	–1.55	1.66	40.67	26.93	3740	1.31	0.01	0.95	1.45	4890	0.73
4189.17	0.17	19.24	1.17	1.06	770	2000	51.28	4.2	–2.02	1.88	47.88	29.95	3760	1.31	0.03	0.97	1.49	4890	0.56
4189.32	0.32	18.56	1.16	1.15	780	2030	53.37	3.86	–1.29	1.73	44.19	32.77	3770	1.29	0.04	0.96	1.51	4880	0.56
4189.48	0.48	17.26	1	0.98	800	2060	51.28	3.82	–1.17	1.64	42.39	32.04	3830	1.3	0.05	0.99	1.52	4910	0.62
4189.63	0.63	15.62	1.16	1.07	850	2110	54.28	4.34	–1.62	1.83	47.57	33.16	3860	1.33	0.05	1.06	1.53	4920	0.71
4189.78	0.78	15.21	1.24	1.14	870	2120	52.97	4.02	–1.33	1.74	44.82	32.99	3900	1.23	0.04	1.17	1.52	4930	0.73
4189.93	0.93	14.02	1.19	1.25	850	2130	50.36	3.77	–1.26	1.68	42.84	31.64	3880	1.07	0.04	1.26	1.49	4920	0.65
4190.09	1.09	14.21	1.17	1.15	850	2110	46.57	3.6	–1.24	1.58	40.45	29.42	3920	0.97	0.04	1.3	1.48	4920	0.72
4190.24	1.24	17.01	1.18	1.06	840	2120	45.79	3.16	–0.53	1.35	35	30.31	3930	0.87	0.05	1.4	1.5	4900	0.73
4190.39	1.39	12.72	1.22	1.02	860	2150	46.57	2.53	–0.16	1.34	32.63	31.2	3990	0.84	0.01	1.45	1.39	4890	0.89

Note: ROP5 = 5-ft averaged rate of penetration, ATR = attenuation resistivity, PSR = phase shift resistivity, RTIM = resistivity time after bit, GTIM = gamma ray time after bit, GR = gamma ray, THOR = thorium, URAN = uranium, POTA = potassium, CGR = computed gamma ray (thorium + potassium), SGR = total gamma ray, DTAB = density time after bit, PEF = photoelectric factor, DRHO = bulk density correction, DC_A = differential caliper, ROMT = rotationally processed density, NTAB = neutron time after bit, and TNPH = thermal neutron porosity.

This is a sample of the table that appears on the volume CD-ROM.

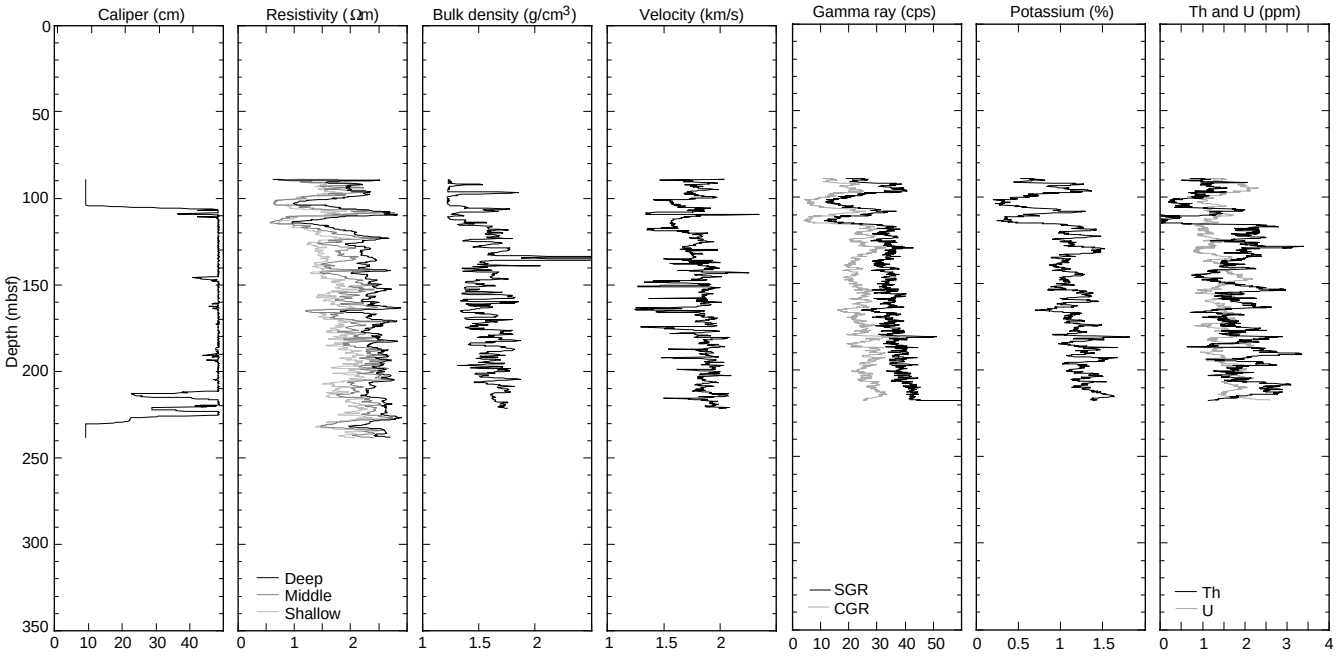

Figure 32. Summary of wireline logging data from Hole 1040C.

Table 26. Composite wireline logging data from Hole 1040C.

Depth (mbsf)	IDPH (Ωm)	IMPH (Ωm)	SFLU (Ωm)	DTLN (µs/ft)	DTLF (µs/ft)	LTT1 (ms)	LTT2 (ms)	LTT3 (ms)	LTT4 (ms)	Uncomp. DT (ms/ft)	DT (ms/ft)
88.467	0.6	1.78	1.03	196.81	17.81	1763.6	1407.87	2140.8	1880.4	236.265	154.0325
88.62	0.72	0.97	1.14	207.3	–0.7	1838.8	1466.4	2140.8	1911.6	222.6	150.4
88.772	0.84	0.74	1.13	192.8	–9.7	1882	1527.8	2412.4	1927.2	199.7	209.85
88.924	1.78	0.7	1.35	190.7	–11.71	1903.6	1573.6	2376.13	1943.73	185.065	190.6
89.077	2.51	0.78	1.79	186.04	–29.8	1936.93	1581.93	2303.6	1948.93	183.5	177.4175
89.229	2.34	0.94	1.95	228.9	–34.97	1934.07	1580.4	2303.6	1955.33	187.465	175.485
89.382	2.29	1.16	1.41	228.7	–8.89	1932	1570.4	2303	1964.4	197	175.05
89.534	1.8	1.3	1.25	216.11	–8.7	1934.07	1563.8	2290.73	1965.13	200.665	173.9675
89.687	1.76	1.26	1.24	217.6	210.12	1928.47	1561.47	2285.27	1948.8	193.665	175.8675
89.839	1.64	1.15	1.18	199.71	212.05	1929.33	1561.73	2285.27	1918.67	178.47	183.55

Notes: IDPH = deep induction phasor-processed resistivity, IMPH = medium induction phasor-processed resistivity, SFLU = spherically focused resistivity unaveraged, DTLN = delta-T long spacing near, DTLF = delta-T long spacing far, LTT1 = long spacing transit time 1 (UT-R1, 10 ft), LTT2 = long spacing transit time 2 (UT-R2, 8 ft), LTT3 = long spacing transit time 3 (LT-R1, 12 ft), LTT4 = long spacing transit time 4 (LT-R2, 10 ft), Uncomp. DT = uncompaeted delta-T, DT = delta-T, Uncomp. V = uncompsated velocity, CALI = caliper, RHOB = bulk density, DRHO = bulk density correction, PEF = photoelectric factor, SGR = spectroscopy gamma ray, CGR = computed gamma ray, THOR = thorium, POTA = potassium, and URAN = uranium.

Table 26 (continued).

Depth (mbsf)	Uncomp. V (km/s)	V (km/s)	CALI (in)	RHOB (g/cm^3)	DRHO (g/cm^3)	PEF (barns/e^-)	SGR (cps)	CGR (cps)	THOR (ppm)	POTA (wt%)	URAN (ppm)
88.467	1.29007682	1.97880317	3.5	1.22	0.01	1.47	18.62	10.19	0.68	0.0051	1.13
88.62	1.36927224	2.02659574	3.5	1.22	0.01	1.45	21.82	12.47	0.75	0.0064	1.25
88.772	1.52628943	1.45246605	3.5	1.23	0.02	1.47	25.16	13.98	1.02	0.0068	1.49
88.924	1.6469889	1.59916055	3.5	1.24	0.02	1.48	24.24	13.14	1.03	0.0062	1.48
89.077	1.66103542	1.7179816	3.5	1.24	0.02	1.49	26.52	14.93	1.18	0.0071	1.55
89.229	1.6259035	1.73690059	3.5	1.24	0.03	1.48	24.58	13.94	0.94	0.007	1.42
89.382	1.54720812	1.7412168	3.5	1.23	0.02	1.44	26.2	15.41	0.97	0.0079	1.44
89.534	1.51894949	1.75205139	3.5	1.22	0.01	1.42	24.15	14.42	0.61	0.0081	1.3
89.687	1.57385175	1.73312295	3.5	1.23	0.01	1.39	20.65	11.51	0.47	0.0065	1.22
89.839	1.70785006	1.66058295	3.5	1.24	0.03	1.39	22.36	12.44	0.73	0.0065	1.33

This is a sample of the table that appears on the volume CD-ROM.

Table 27. *P*-wave velocities obtained from the PWL using the MST on unsplit cores from Site 1040.

Leg	Site	Hole	Core	Type	Section	Top (cm)	Bottom (cm)	Depth (mbsf)	Velocity (m/s)	Meas. separation mean (mV)	Meas. separation SD (mV)	Mean time mean (µs)	Meas. time SD (µs)	Acoustic level mean	Attempted daq	Valid daq	Thickness (mm)
170	1040	A	1	H	1	5.3	5.3	0.05	1505	190	0	51.17	0.023	86	25	25	2.54
170	1040	A	1	H	1	7.3	7.3	0.07	1509.2	190	0	51.05	0.024	179	25	5	2.54
170	1040	A	1	H	1	9.3	9.3	0.09	1500.6	190	0	51.3	0.01	178	25	5	2.54
170	1040	A	1	H	1	13.3	13.3	0.13	1502.3	190	0	51.25	0.014	172	0	25	2.54
170	1040	A	1	H	1	15.3	15.3	0.15	1502.1	189	0	51.19	0.02	85	25	25	2.54
170	1040	A	1	H	1	19.3	19.3	0.19	1489.9	189	0	51.55	0.017	159	25	25	2.54
170	1040	A	1	H	1	21.3	21.3	0.21	1481.2	189	0	51.81	0.018	186	25	25	2.54
170	1040	A	1	H	1	23.3	23.3	0.23	1475.6	189	0	51.98	0.023	189	25	25	2.54
170	1040	A	1	H	1	25.3	25.3	0.25	1482.2	189	0	51.78	0.024	192	25	25	2.54
170	1040	A	1	H	1	27.3	27.3	0.27	1556.8	189	0	49.65	0.01	0	0	25	2.54

Note: SD = standard deviation, Meas. = measured, and daq = data acquisition.

This is a sample of the table that appears on the volume CD-ROM.

Table 28. *P*-wave velocities obtained from the PWS3 on split cores from Site 1040.

Leg	Site	Hole	Core	Type	Section	Top (cm)	Bottom (cm)	Depth (mbsf)	Velocity (m/s)
170	1040	A	1	H	1	0.73	72.6	0.73	1620.1
170	1040	A	1	H	1	1.4	140	1.4	1607.2
170	1040	A	1	H	2	2	49.6	2	1580.3
170	1040	A	1	H	2	2.6	110	2.6	1571.8
170	1040	A	1	H	3	3.59	58.6	3.59	1654.2
170	1040	A	1	H	3	4.19	119.1	4.19	1632.8
170	1040	A	1	H	4	4.68	18.4	4.68	1700.4
170	1040	A	1	H	4	4.86	35.9	4.86	1640.4
170	1040	A	1	H	4	5.67	117.1	5.67	1684.7
170	1040	A	1	H	4	5.68	118.3	5.68	1687.2

This is a sample of the table that appears on the volume CD-ROM.

bonate sequence experiencing less compaction than the upper diatomaceous and clayey beds. Below 560 mbsf, velocity measurements return to a trend of increasing velocity with depth, reaching values of 1700–1800 m/s near the base of Unit U3 at about 650 mbsf. At 660 mbsf, just above the gabbro, a thin sediment layer with velocities of 2000 m/s or more was recorded, perhaps reflecting baked sediment associated with the gabbro intrusion.

Downhole Measurements

In situ sonic velocity measurements were acquired by the long-spaced sonic logging tool (LSS) as a part of the wireline logging toolstring. The interval from 88 to 222 mbsf was logged in Hole 1040C (Fig. 32). Borehole-compensated sonic velocity shows a gradual increase from 1700 to 2000 m/s with depth. These values agree well with the few available *P*-wave velocity measurements from discrete core specimens, although the log data fluctuate much more widely.

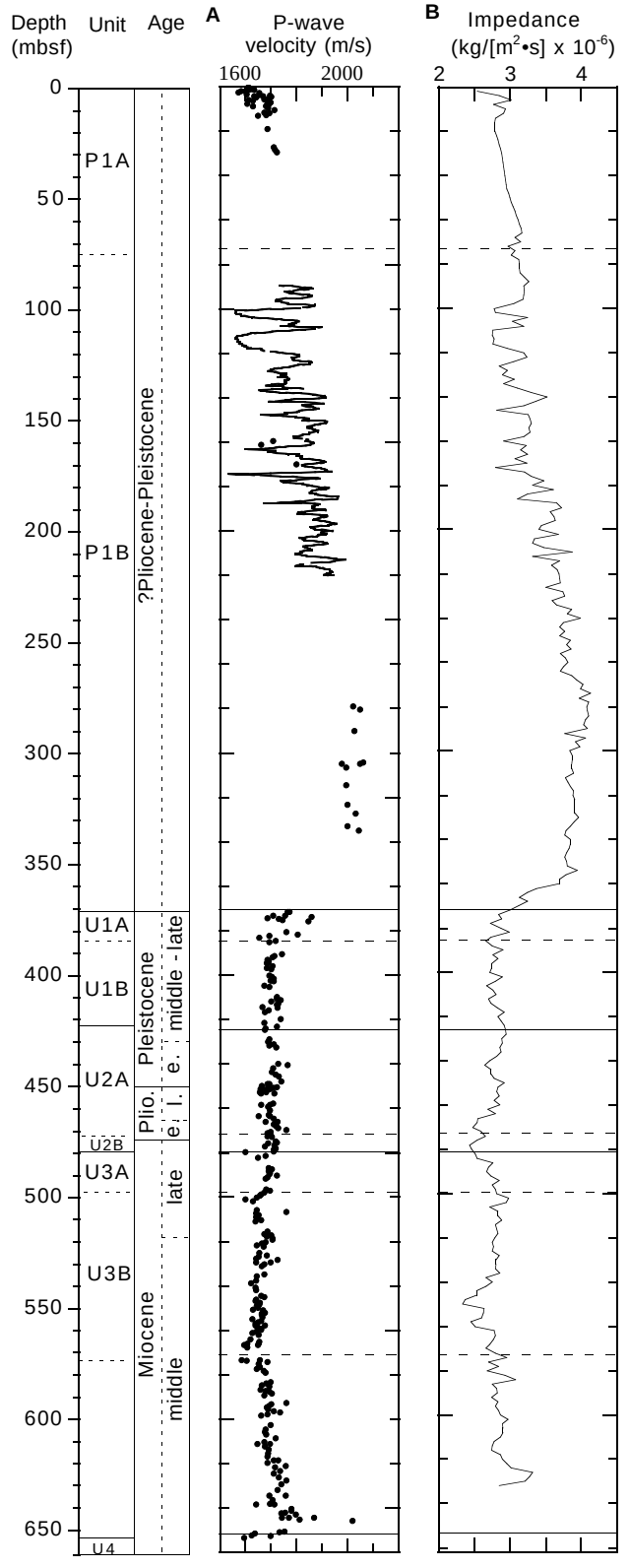

Figure 33. **A.** Acoustic compressional wave velocity, measured by wireline sonic logging (smooth line) and by the PWS3 transducers on specimens from split cores (solid circles). **B.** Acoustic impedance, or the product of *P*-wave velocity and bulk density. Velocity (Fig. 33A) and density (Fig. 1) were resampled at an interval of 2 m.

Synthetic Seismogram

A synthetic seismogram was created from the velocity and density data sets collected at Site 1040 to tie core-derived structure and stratigraphy data to the seismic-reflection data of Line CR-20 (Fig. 2). Velocity data were assembled from samples measured by the PWS3 (0–30 mbsf, 285–337 mbsf, and 373–656 mbsf) and from the wireline sonic log (88–220 m). To complete the profile, velocities were linearly interpolated across data gaps above and below the sonic log. At 347 and 363 mbsf, two estimated velocity points were included in a data gap. These additional points are consistent with the trend of the density profile in this interval and were necessary to extend the velocity profile to the décollement level or base of the upper plate as defined by the large drop in density and recovery of underthrust material in the cores. Density data were compiled from LWD bulk density (Hole 1040E) in the interval 0–310 mbsf and from laboratory-based moisture and density measurements from 310 to 665 mbsf. Consistent with results at Site 1039, synthetic data created using the LWD bulk density data appeared to be superior to that created with core-derived bulk density. Most of the laboratory-based velocity and density measurements came from cores of Hole 1040C, which deviated substantially from vertical. Depth corrections, to approximate true vertical depth, were made before creating the synthetic data. The composite velocity and density profiles, sampled at 2-m depth intervals, were combined to form an acoustic impedance series, and a reflectivity series was computed at a 1-ms sample interval. A wavelet derived from the seafloor reflection was convolved with the reflectivity series to produce the synthetic traces shown in Figure 34.

The synthetic data produced in this process match the real seismic data at this site well and therefore allow detailed correlation between the stratigraphic and structural data from cores and arrivals on Line CR-20. Above the décollement at Site 1040 (from 5575 to 5960 ms two-way traveltime), Line CR-20 shows sparse reflections, most of which are associated with faulting rather than stratigraphic layering (Shipley et al., 1992). Several arrivals with poor to fair continuity when crossing the drill path of Site 1040 are reasonably well matched by events in the synthetic data. In particular, events marked by dominant negative deflections at ~5800 and 5850 ms are similar to events in the reflection data. Both of these arrivals may mark fault zones, as suggested by the seismic data, and the event at ~5800 ms corresponds to a zone of anomalous pore-water chemistry and elevated hydrocarbon gas content. The high-amplitude event at ~5700 ms in the synthetic data, however, may be the result of poor hole conditions during wireline logging. Anomalous measurements were present in all wireline logs in this interval, including caliper, but not identified in the subsequent LWD logs through this interval.

The top of the underthrust section is clearly marked by the large negative deflection at 5960 ms. Within the underthrust section, the best synthetic–real data match is with Unit U3 and its subunits. A good correlation exists from 5960 to 6230 ms, but the top of Unit U4, at 6280 ms in the synthetic data, is 12–15 ms late compared to its arrival time on Line CR-20. In this interval above the gabbro intrusion, laboratory-measured velocity averages 1720 m/s, whereas the velocity required to match the observed reflection time is 2260–2460 m/s. A velocity discrepancy was also observed at Site 1039, although it was cumulative across all of Unit U3 rather than restricted to Subunit U3C, and the error was a modest 6%. The velocity discrepancy at Site 1040, however, is greater than 20%. The error here could be caused by more lithified samples at the base of the section, which may suffer more dramatic rebound effects. Errors of similar magnitude have been observed in other carbonate-rich sections with in situ velocities in the range of 1600–2500 m/s (Urmos et al., 1993; Jarrard et al., 1993).

Magnetic Susceptibility

Magnetic susceptibility (Fig. 1; Table 29) is characterized by large variability in the upper 25 mbsf, corresponding to debris flows

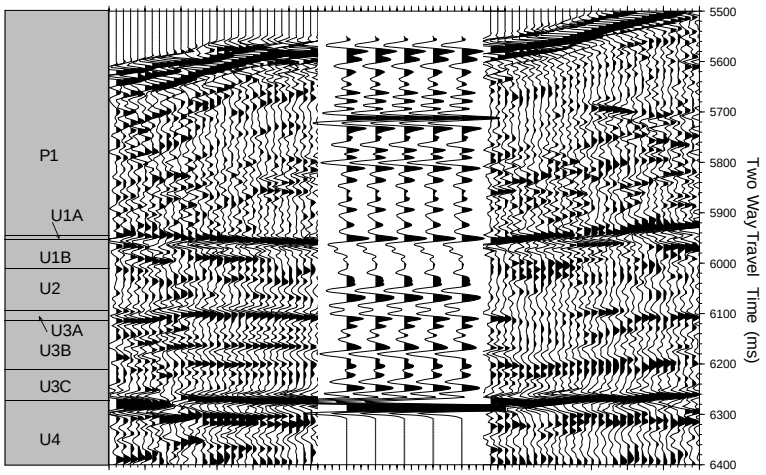

Figure 34. Line CR-20 seismic-reflection data in the vicinity of Site 1040 with synthetic seismic traces inserted at the Site 1040 location. Lithostratigraphic units are indicated at the left, with Unit P1 from the upper plate and the remainder being underthrust units.

Table 29. Magnetic susceptibility values obtained on unsplit cores using the MST, Site 1040.

Leg	Site	Hole	Core	Type	Section	Top (cm)	Bottom (cm)	Depth (mbsf)	Relative, drift corr. sus.	Relative, sus. mean	Actual daq period (s)	Core diameter (cm)	Sample elapsed zero time (s)	Background correction
170	1040	A	1	H	1	3	3	0.03	176.3	176.2	5	6.7	8005	–0.1
170	1040	A	1	H	1	5	5	0.05	186.7	186.6	5	6.7	11405	–0.1
170	1040	A	1	H	1	7	7	0.07	205.3	205.2	5	6.7	14801	–0.1
170	1040	A	1	H	1	9	9	0.09	225.9	225.8	5	6.7	18203	–0.1
170	1040	A	1	H	1	11	11	0.11	242.9	242.8	5	6.7	21603	–0.1
170	1040	A	1	H	1	13	13	0.13	256	255.8	5	6.7	25006	–0.2
170	1040	A	1	H	1	15	15	0.15	253.8	253.6	5	6.7	28408	–0.2
170	1040	A	1	H	1	17	17	0.17	235.6	235.4	5	6.7	31795	–0.2
170	1040	A	1	H	1	19	19	0.19	216.2	216	5	6.7	35186	–0.2
170	1040	A	1	H	1	21	21	0.21	202.3	202	5	6.7	38573	–0.3

Note: Corr. = corrected, sus. = susceptibility, and daq = data acquistion.

This is a sample of the table that appears on the volume CD-ROM.

Table 30. Vane shear strength data for Holes 1040A and 1040B.

Leg	Site	Hole	Core	Type	Section	Top (cm)	Bottom (cm)	Depth (mbsf)	Undrained shear strength (kPA)	Undrained residual strength (kPa)	Time (s)
170	1040	A	1	H	1	129.7	129.7	1.3	24.7	13.7	34.74
170	1040	A	1	H	1	72	72	0.72	11.4	9.1	16.02
170	1040	A	1	H	1	72	72	0.72	11.4	9.1	16.02
170	1040	A	1	H	1	25.4	25.4	0.25	9.5	4.4	13.32
170	1040	A	1	H	2	109.6	109.6	2.6	24.1	17.3	34.02
170	1040	A	1	H	2	135.9	135.9	2.86	29.6	17.2	41.76
170	1040	A	1	H	2	135.9	135.9	2.86	29.6	17.2	41.76
170	1040	A	1	H	4	117.9	117.9	5.68	75.5	42.8	106.38
170	1040	A	1	H	4	27.2	27.2	4.77	41.6	29.4	58.68
170	1040	A	1	H	4	27.2	27.2	4.77	41.6	27.8	58.68

This is a sample of the table that appears on the volume CD-ROM.

or silty sand layers within the silty clay of Subunit P1A (0–75 mbsf). From 25 to 270 mbsf, the variability is greatly reduced, with values decreasing to nearly zero at the bottom of the interval. At 270 mbsf, a sharp increase in magnetic susceptibility values is observed. This corresponds with a porosity decrease in the narrow interval from ~270 to 290 mbsf. However, no obvious change in lithology occurs at this depth. Subunit P1B (75–357 mbsf) is characterized by uniform silty clay with intervals of silt to very fine sand.

Magnetic susceptibility in the underthrust sedimentary section closely mimics the variations at Hole 1039B. A narrow region of uncommonly high magnetic susceptibility is found at or just below the base of the décollement zone from ~371 to 376 mbsf. The high values may be associated with ash layers or turbiditic sand. Alternatively, the high values may result from a magnetic carrier produced during diagenesis. Positive excursions in susceptibility values are observed throughout Unit U1. Smaller peaks are present throughout Unit U2 (423–480 mbsf), which also has a lower background value. The boundary between Units U2 and U3 is marked by a small, but sharp, increase in susceptibility. Values decrease with depth throughout Subunit U3A (480–500 mbsf). A feature characteristic of the magnetic susceptibility data set is the sudden decrease to near zero at the top of the chalk of Subunit U3B (500–653 mbsf). Susceptibility values increase by a small amount in the lower 30 m of Unit U3, and values become very high in the deepest few meters of the layer. In the gabbro intrusion of Unit U4, susceptibility is at least an order of magnitude greater than in the sedimentary section above.

Vane Shear Strength

Undrained shear strength measurements were made using the motorized miniature vane shear device on cores from Holes 1040A and 1040B (Table 30). Only data from lithostratigraphic Subunit P1A (0–

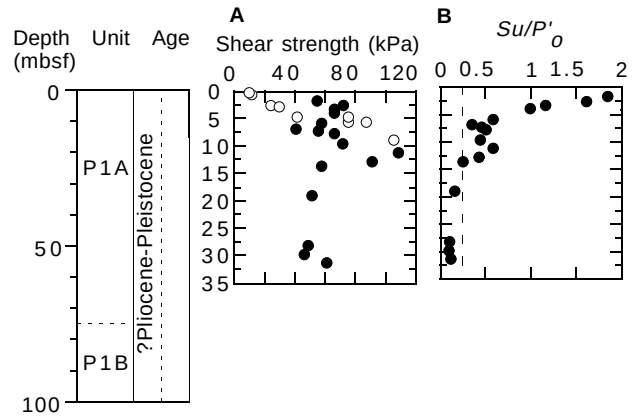

Figure 35. **A.** Undrained shear strength, measured with the automated vane shear device vs. depth at Site 1040 (open circles = Hole 1040A; solid circles = Hole 1040B). **B.** Shear strength to effective overburden stress ratio (S_u/P'_0) plotted as a function of shear strength vs. depth. Typical normally consolidated sediment has a ratio of about 0.25 (dashed line), suggesting that sediment at Site 1040 is overconsolidated in the upper 14 m.

35 mbsf) were collected reliably. Below this depth, the sediment was either stronger than the instrument's spring, or sediment failure was accomplished largely by cracking. Data are thus presented only for the upper section (Fig. 35A).

Between 0 and 10 mbsf, shear strength values increase rapidly with depth from 10 kPa at the mudline to 112 kPa at 12 mbsf. The latter value is in excess of the maximum reading taken at Hole 1039B (98 kPa at 97 mbsf). Below 12 mbsf, shear strength values become more scattered and decrease significantly between 10 and 32 mbsf. This decrease is probably attributable to small-scale cracking of the sediment before true failure, yielding lower values of peak strength.

An estimate of the consolidation state can be made by comparing the shear strength to the overburden stress, assuming lithostatic loading (Figure 35B). The sediment is significantly overconsolidated between 0 and 14 mbsf, and below 14 mbsf the material is normally consolidated or lightly underconsolidated. Such behavior is reflected in the porosity and bulk density data.

Electrical Resistivity

Laboratory Measurements

It was only possible to measure electrical resistivity on certain cores. Much of the recovered sediment was too brittle, incohesive, or disturbed by drilling for reliable measurements. Pore-water chemistry measured onboard (see "Geochemistry" section, this chapter) shows marked deviations from seawater salinity; hence the results are presented as measured resistivity rather than as derived formation factor (Fig. 36A; Table 31). The resistivities measured on the split cores are repeatable, but significantly lower than those derived from downhole measurements. For these reasons it is suggested that these split-core results be used only to show relative changes rather than to determine absolute values.

In the upper section of Holes 1040A and 1040B where cohesive sediment was recovered intact, measurements were taken at a 50-cm spacing. Resistivity values increase sharply with depth, which correlates with a decrease in porosity and an increase in undrained shear strength measured over the same interval. These values are high for such a shallow depth range, and therefore the resistivity data support the inference that the upper part (0–14 mbsf) of the sedimentary section is strongly overconsolidated.

In XCB- and RCB-recovered sediment below 20 mbsf, resistivity values display less obvious trends, but range from 0.7 to 1.1 Ωm in the more intact parts of the core. Clayey silt from the deformation

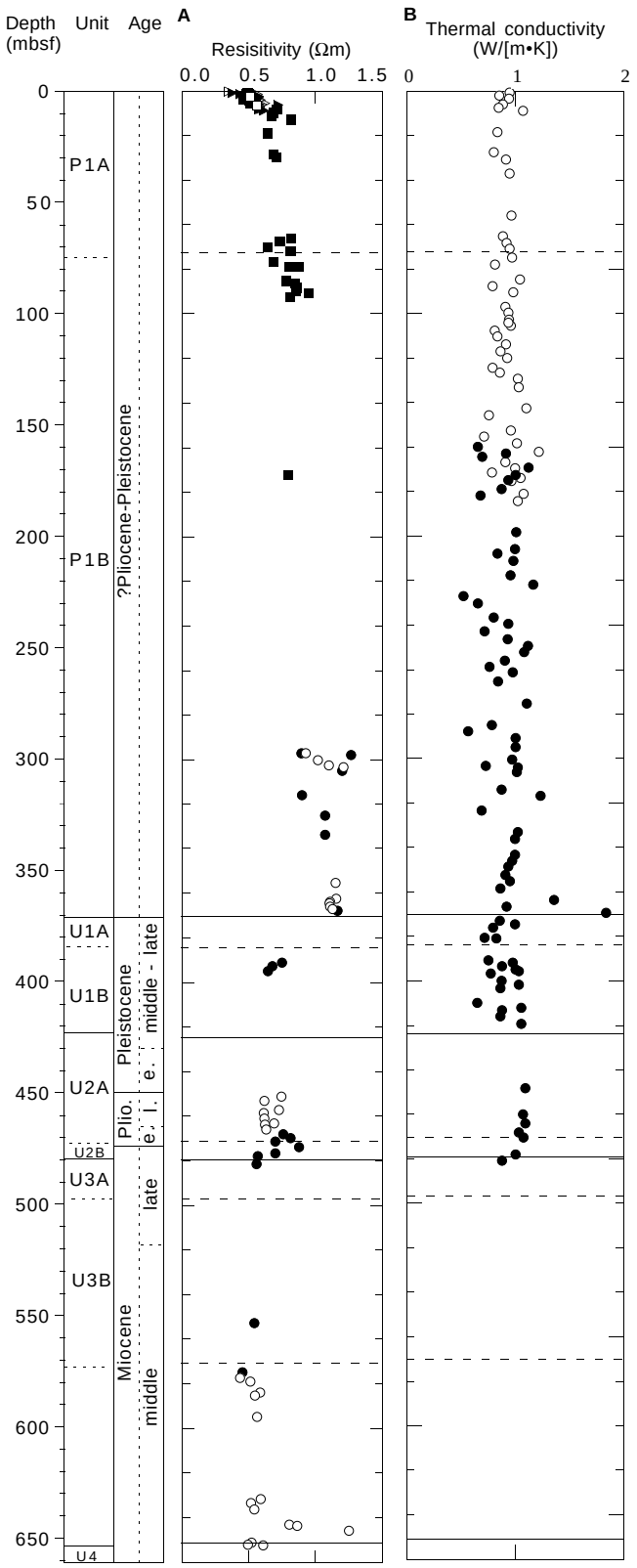

Figure 36. **A.** Split-core electrical resistivity measurements plotted with depth for Site 1040. Solid triangles = Hole 1040A transverse, open triangles = Hole 1040A longitudinal, open squares = Hole 1040B transverse, solid squares = Hole 1040B longitudinal, open circles = Hole 1040C transverse, and solid circles = Hole 1040C longitudinal. **B.** Thermal conductivity vs. depth for Site 1040. Open circles = Hole 1040B; solid circles = Hole 1040C.

Table 31. Electrical resistivity measurement data collected from Site 1040.

Site	Hole	Core	Section	Top (cm)	Depth (mbsf)	Transverse resistivity (Ωm)	Longitudinal resistivity (Ωm)	Formation factor, transverse	Formation factor, along core
1040	A	1	1	147	1.47	0.44		2.17	
1040	A	1	1	95	0.95	0.378		1.86	
1040	A	1	1	14	0.14		0.351		1.73
1040	A	1	2	132	2.82	0.474		2.38	
1040	A	1	2	145	2.95		0.574		2.91
1040	A	1	2	147	2.97	0.562		2.85	
1040	A	1	2	100	2.5	0.576		2.92	
1040	A	1	3	100	4		0.587		2.98
1040	A	1	3	48	3.48		0.562		2.85
1040	A	1	3	50	3.5	0.555		2.82	

This is a sample of the table that appears on the volume CD-ROM.

zone at about 300 mbsf and disturbed plastic clay in the zone immediately above the décollement horizon display resistivity values up to 1.3 Ωm, which decrease to ~0.7 Ωm in the upper part of the underthrust interval. Below this depth (~371 mbsf), resistivity decreases somewhat with depth to ~0.5 Ωm in the lower part of the underthrust Unit U3. Positive and negative excursions occur in measured resistivity within the underthrust interval. The most marked deviation from the trend occurs in Core 170-1040C-51R at 10 m above the gabbro intrusion. At this interval, the resistivity exceeds 1.2 Ωm. This observation could be related to low-grade metamorphism of the carbonate caused by intrusion of the gabbro body.

Downhole Measurements

In situ resistivity measurements were collected using the CDR in Holes 1040D and 1040E. The deep and shallow resistivity logs in Figure 31 show very similar trends and amplitudes, indicating good hole conditions. Excellent quality of the resistivity logs allows bed thickness to be resolved.

The resistivity profiles basically show trends similar to the density profiles in both holes. In the interval 0–200 mbsf, the resistivity values gradually increase from 1 to 2.5 Ωm in Hole 1040D, whereas in Hole 1040E the values show greater fluctuation. In Hole 1040D, the interval 200–277 mbsf is characterized by relatively high resistivity values up to 3.2 Ωm. In Hole 1040E, the high-resistivity interval is identified between 210 and 242 mbsf. Large peaks in resistivity values greater than 3.5 Ωm are identified at 114, 168, 238, and 270 mbsf in Hole 1040E. The resistivity peak at 114 mbsf corresponds with a peak in bulk density. However, the peaks at 168, 238, and 270 mbsf correlate with negative peaks in density. The low-density and high-resistivity intervals suggest the possible occurrence of gas hydrates (see "Geochemistry" section, this chapter).

The wireline phasor dual induction tool (DIT) was deployed at Hole 1040C in the interval from 88 to 238 mbsf (Fig. 32). Resistivity values fluctuate from 0.5 to 2.9 Ωm, and are lower than the values measured by the CDR tool on the LWD string. Washed-out borehole conditions, shown by the caliper log, may be the cause of these low and fluctuating resistivity values.

Thermal Conductivity

Thermal conductivity data were collected on unsplit cores at three or four positions along each core, using the full-space needle probe method (Table 32). Measurements made on cored intervals heavily disturbed by drilling were subsequently discarded. Harder sediments were measured using the half-space method on split cores (see "Explanatory Notes" chapter, this volume).

Average thermal conductivity values show little variation with increasing depth (Fig. 36B). From 0 to 420 mbsf, the values stay at ~1 W/(m·K). Some of the scatter observed is likely to be caused by variations in the degree of drilling disturbance. The underthrust section (371 mbsf and below) has thermal conductivity values ~0.3 W/(m·K) higher than the equivalent reference section at Site 1039. This increase reflects the decrease in porosity caused by compaction and possible dissolution of diatom frustules. However, no significant change in thermal conductivity was measured across the décollement zone even though marked changes in porosity and density are recorded.

Table 32. Thermal conductivity data for Site 1040.

Site	Hole	Core	Type	Section	Top (cm)	Bottom (cm)	Depth (mbsf)	Thermal conductivity (W/[m·K])
1040	B	1	H	1	70	70	0.7	0.9485
1040	B	1	H	2	50	50	2	0.8585
1040	B	1	H	3	50	50	3.5	0.945
1040	B	2	H	1	50	50	6	0.893
1040	B	2	H	2	50	50	7.5	0.848
1040	B	2	H	3	50	50	9	1.075
1040	B	4	X	1	50	50	18.5	0.841
1040	B	5	X	1	50	50	27.5	0.801
1040	B	5	X	3	50	50	30.5	0.915
1040	B	6	X	1	50	50	36.9	0.947

This is a sample of the table that appears on the volume CD-ROM

Table 33. Summary of in situ temperature measurements at Site 1040.

Depth (mbsf)	Hole, core	Tool	Equilibrium temp. (°C)	Comments
10 m above mudline	1040C	WSTP	2.09 ± 0.1	
55.2	1040B-7X	DVTP	—	Bad data
84.00	1040B-10X	DVTP	2.53 ± 0.1	
113.40	1040B-15X	DVTP	2.77 ± 0.1	
161.40	1040B-20X	DVTP	3.17 ± 0.1	
226.50	1040C-8R	DVTP	3.63 ± 0.1	
274.70	1040C-13R	DVTP	3.89 ± 0.1	
323.00	1040C-18R	DVTP	4.20 ± 0.1	
380.60	1040C-23R	DVTP	4.58 ± 0.1	
428.60	1040C-28R	DVTP	5.00 ± 0.1	
476.70	1040C-33R	DVTP	5.39 ± 0.1	

Note: WSTP = water-sampling temperature probe, DVTP = Davis-Villinger Temperature Probe.

Heat Flow

Equilibrium temperatures obtained from the WSTP and the DVTP are shown in Table 33 and Figure 37 and are also shown as a function of depth in Figure 38. The errors were determined subjectively, based on the stability of the equilibration record and tool performance. The geothermal gradient at Site 1040 is 8.3°C/km, 5.9°C/km, and 8.4°C/km in the intervals from about 0 to 161.4 mbsf, 227 to 323 mbsf, and 380 to 477 mbsf, respectively. The average geothermal gradient in the whole interval was 7.2°C/km.

Heat flow is estimated from the in situ equilibrium temperature measurements and the thermal conductivity values measured on board (Figure 36B). The inverse of the slope of the temperature vs.

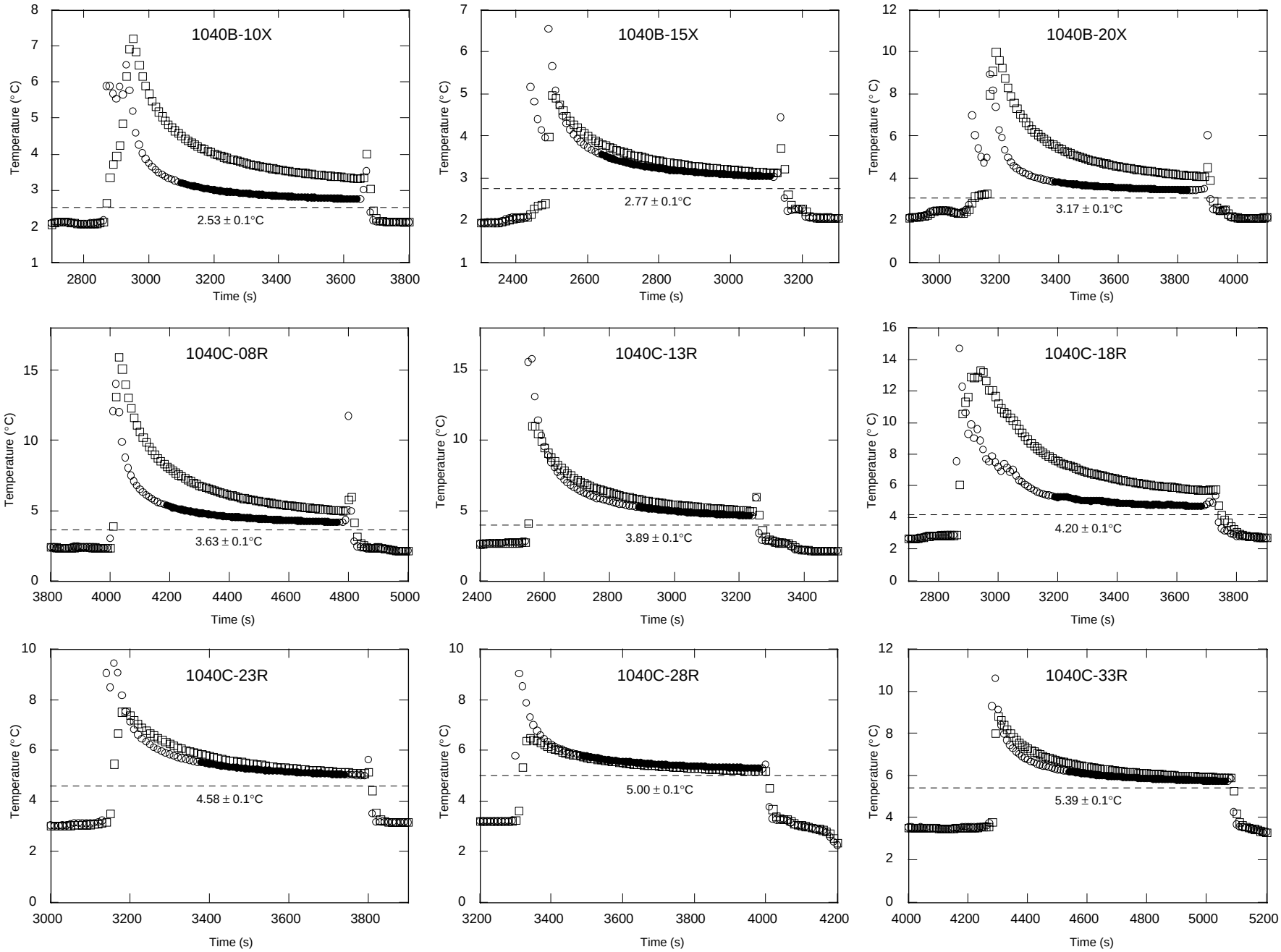

Figure 37. Temperature vs. time data from the DVTP at Holes 1040B and 1040C. The dashed line in each panel indicates the estimated equilibrium temperature determined by fitting a synthetic curve to the equilibration record. Circles and squares for the DVTP indicate temperature data from the upper and lower thermistor, respectively. The portion of the equilibrium curve used for the curve fitting is indicated with solid circles.

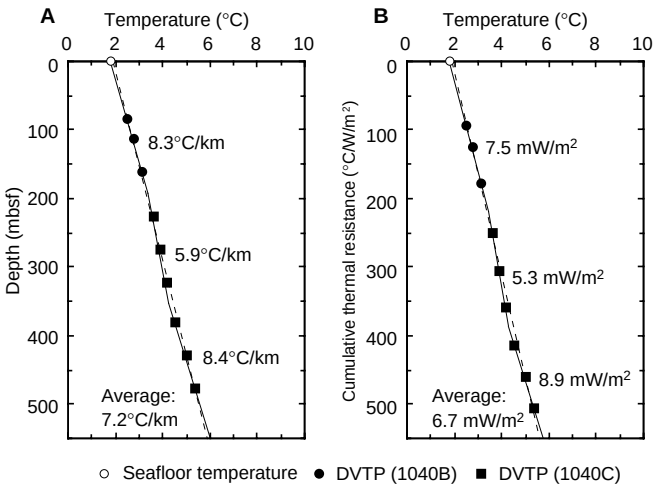

Figure 38. **A.** Temperature vs. depth at Site 1040. Thermal gradients in the three segments and over an interval are shown. **B.** Temperatures vs. cumulative thermal resistance. Mean heat-flow values in the three segments and over an interval are shown.

the cumulative thermal resistance curve (Figure 38B) yields a direct measure of heat flow. The heat-flow values are 7.5 mW/m^2, 5.3 mW/m^2, and 8.9 mW/m^2 in the intervals from about 0 to 161.4 mbsf, 227 to 323 mbsf, and 380 to 477 mbsf, respectively. The averaged heat-flow value in the whole interval is 6.7 mW/m^2, which is slightly lower than the value at Site 1039 (8.3 mW/m^2; see "Site 1039" chapter, this volume). The relatively low heat flow in the interval between ~200 and 370 mbsf may imply fluid flow above the décollement, which is also suggested by the interstitial water chemistry (see "Geochemistry" section, this chapter).

Colorimetry

Sediments cored at Site 1040 show lightness component (L*) values that oscillate between 30% and 40% from the seafloor to about 450 mbsf and then increase rapidly, reaching 75% at 500 mbsf. L* values are ~70% for over 100 m and then drop to 48% at the base of Hole 1040C (Fig. 1). The interval of relatively constant and low lightness encompasses Units P1, U1, and half of Subunit U2A; the region of rapid increase includes the basal half of Subunit U2A and all of Subunits U2B and U3A. A 10% drop at 490 mbsf (within Subunit U3A) marks the 35% ramp over 10 m that leads to Subunit U3B. The lightness curve for values above 40% (all of Unit U3) correlates well with the carbonate concentrations obtained from core catchers at this site (Fig. 1).

Subunits P1A through U2B are almost indistinguishable on the lightness curve. The red/blue (a*/–b*) ratio, however, allows us to differentiate Unit U2 from the overlying units, given their relatively high ratios (~0.8) when compared with ratios of Units P1 and U1 (0.48 ± 0.5). Unit U3 has red/blue ratios below 0.3, whereas the intrusive Unit U4 has the highest mean value of 1.6. A comparison of L* and a*/–b* values for each unit is given in Fig. 39A.

Plots of mean reflectance vs. wavelength for each lithostratigraphic unit cored at Site 1040 show no significant difference for Subunits P1A through U2A, both in the magnitude and shape of the curves (Fig. 39B). Subunits U2B and U3A, and Unit U4 have similar overall reflectance, but their spectra are slightly different. As with lightness, Subunit U3B shows the highest values; Subunits U3B and U3C have the largest dependency of reflectance with wavelength.

Natural Gamma Ray and Photoelectric Effect

In situ natural gamma-ray measurements were collected by the CDR tool, and the photoelectric effect (PEF) was measured by the CDN tool in Holes 1040D and 1040E (Fig. 31). Values of total spectral gamma ray roughly show a constant trend with frequent fluctuation between 35 and 60 counts per seconds (cps) throughout Hole 1040E. Yields of the potassium, thorium, and uranium spectrometry range between 1% and 2%, 0 and 4 ppm, and 0 and 6 ppm, respectively. A relatively large increase in the total spectral gamma ray occurs between 200 and 220 mbsf, coincident with increases in the values of bulk density and resistivity. Large peaks of the total spectral gamma ray occur at 82, 168, 176, 232, and 270 mbsf. These peaks are all correlated with the resistivity peaks, except for that at 82 mbsf. Values of PEF approximately range from 2.0 to 4.0 barns/e$^-$ in Hole 1040D and from 2.5 to 3.5 barns/e$^-$ in Hole 1040E, which indicates the variation in typical rock-forming minerals and biogenic components. The values show no remarkable change, which is an indication of the general homogeneity of lithologic Unit P1.

REFERENCES

Berggren, W.A., Hilgen, F.J., Langereis, C.G., Kent, D.V., Obradovich, J.D., Raffi, I., Raymo, M.E., and Shackleton, N.J., 1995a. Late Neogene chronology: new perspectives in high-resolution stratigraphy. Geol. Soc. Am. Bull., 107:1272–1287.

Berggren, W.A., Kent, D.V., Swisher, C.C., III, and Aubry, M.-P., 1995b. A revised Cenozoic geochronology and chronostratigraphy. *In* Berggren, W.A., Kent, D.V., Aubry, M.-P., and Hardenbol, J. (Eds.), *Geochronology, Time Scales and Global Stratigraphic Correlation.* Spec. Publ.—Soc. Econ. Paleontol. Mineral., 54:129–212.

Bordovskiy, O.K., 1965. Accumulation and transformation of organic substances in marine sediment, 2. Sources of organic matter in marine basins. *Mar. Geol.*, 3:5–31.

Carr, M.J., and Rose, W.I., 1987. CENTAM: a data base of Central American volcanic rocks. *J. Volcanol. Geotherm. Res.*, 33:2239–2240.

Emerson, S., and Hedges, J.I., 1988. Processes controlling the organic carbon content of open ocean sediments. *Paleoceanography,* 3:621–634.

Gill, J.B., Hiscott, R.N., and Vidal, P., 1994. Turbidite geochemistry and evolution of the Izu-Bonin arc and continents. *Lithos,* 33:135–168.

Jarrard, R.D., Jackson, P.D., Kasschau, M., and Ladd, J.W., 1993. Velocity and density of carbonate-rich sediments from northeastern Australian margin: integration of core and log data. *In* McKenzie, J.A., Davies, P.J., Palmer-Julson, A., et al., *Proc. ODP, Sci. Results*, 133: College Station, TX (Ocean Drilling Program), 633–647.

Langseth, M.G., and Silver, E.A., 1996. The Nicoya convergent margin: a region of exceptionally low heat flow. *Geophys. Res. Lett.*, 23:891–894.

McLennan, S.M., and Taylor, S.R., 1984. Archean sedimentary rocks and their relationship to the composition of the Archean continental crust. *In* Kroner, A., Hanson, G.N., and Goodwin, A.M. (Eds.), *Archaean Geochemistry: The Origin and Evolution of the Archaean Continental Crust:* Berlin (Springer-Verlag), 47–72.

Plank, T., and Langmuir, C.H., 1993. Tracing trace elements from sediment input to volcanic output at subduction zones. *Nature*, 362:739–743.

Shipley, T.H., McIntosh, K.D., Silver, E.A., and Stoffa, P.L., 1992. Three dimensional seismic imaging of the Costa Rica accretionary prism: structural diversity in a small volume of the lower slope. *J. Geophys. Res.*, 97:4439–4459.

Shipley, T.H., and Moore, G.F., 1986. Sediment accretion, subduction, and dewatering at the base of the trench slope off Costa Rica: a seismic reflection view of the decollement. *J. Geophys. Res.*, 91:2019–2028.

Shipley, T.H., Stoffa, P.L., and Dean, D.F., 1990. Underthrust sediments, fluid migration paths, and mud volcanoes associated with the accretionary wedge off Costa Rica: Middle America trench. *J. Geophys. Res.*, 95:8743–8752.

Stein, R., Brass, G., Graham, D., Pimmel, A., and the Shipboard Scientific Party, 1995. Hydrocarbon measurements at Arctic Gateways sites (ODP Leg 151). *In* Myhre, A.M., Thiede, J., Firth, J.V., et al., *Proc. ODP, Init. Repts.*, 151: College Station, TX (Ocean Drilling Program), 385–395.

Urmos, J., Wilkens, R.H., Bassinot, F., Lyle, M., Marsters, J.C., Mayer, L.A., and Mosher, D.C., 1993. Laboratory and well-log velocity and density measurements from the Ontong Java Plateau: new in-situ corrections to laboratory data for pelagic carbonates. *In* Berger, W.H., Kroenke, L.W., Mayer, L.A., et al., *Proc. ODP, Sci. Results*, 130: College Station, TX (Ocean Drilling Program), 607–622.

Wilson, M., 1989. *Igneous Petrogenesis: A Global Tectonic Approach:* London (Unwin Hyman).

Ms 170IR-104

NOTE: Core-description forms ("barrel sheets") and core photographs can be found in Section 3, beginning on page 251. Smear-slide data, thin-section descriptions, and shore-based processed log data and descriptions can be found on CD-ROM. See Table of Contents for material contained on CD-ROM.

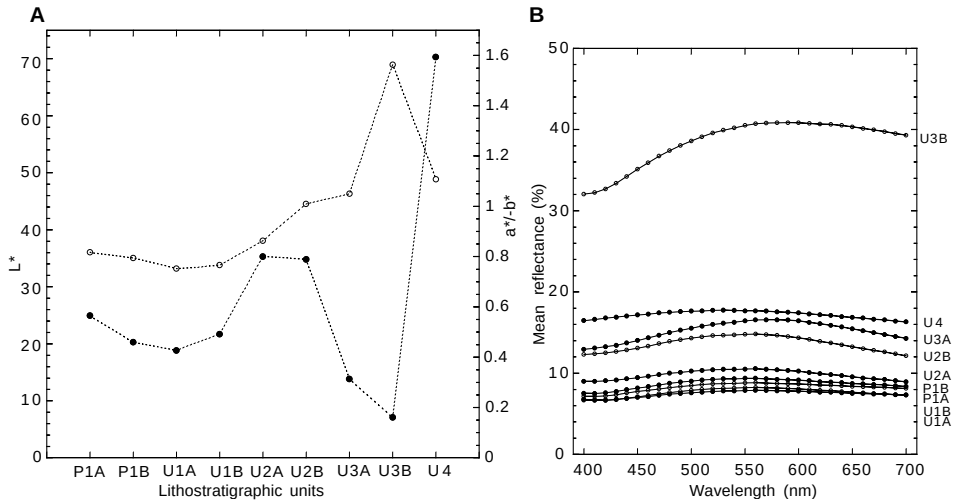

Figure 39. **A.** Mean lightness component (L*; open circles) and chromaticity ratio (a*/–b*; solid circles) for each lithostratigraphic unit drilled at Site 1040. **B.** Mean percentage of reflectance vs. wavelength for each unit cored at Site 1040.

Previous Chapter Table of Contents Next Chapter